SPIN DEPENDENT CURRENT INJECTION INTO EPITAXIAL GRAPHENE NANORIBBONS

A Thesis
Presented to
The Academic Faculty

by

John H. Hankinson V

In Partial Fulfillment
of the Requirements for the Degree
Doctor of Philosophy in the
School of Physics

Georgia Institute of Technology
August 2015

SPIN DEPENDENT CURRENT INJECTION INTO EPITAXIAL GRAPHENE NANORIBBONS

Approved by:

Dr. Walt A. de Heer, Advisor
School of Physics
Georgia Institute of Technology

Dr. Zhigang Jiang
School of Physics
Georgia Institute of Technology

Dr. Edward H. Conrad
School of Physics
Georgia Institute of Technology

Dr. Robert Haddon
Department of Chemistry
University of California, Riverside

Dr. Phillip N. First
School of School of Physics
Georgia Institute of Technology

Date Approved: May 14th, 2015

To my parents, John and Gail Hankinson

ACKNOWLEDGEMENTS

I wish to sincerely thank my advisor, Dr. Walt de Heer, for giving me the opportunity to work on such an exciting research topic and for all of the advice and guidance he has given me over the years. I would also like to thank Dr. Claire Berger for mentoring, training, and teaching me. I also want to thank everyone on my committee: Dr. Edward Conrad, Dr. Philip First, Dr. Zhigang Jiang, and Dr. Robert Haddon. I am grateful to my colleagues for all of the experimental help and useful discussions they provided since I came to Georgia Tech: Dr. Lei Ma, Dr. Mike Sprinkle, Dr. Xiaosong Wu, Dr. Ming Ruan, Dr. Farhana Zaman, Dr. Zelei Guo, Dr. James Palmer, Baiqian Zhang, Dr. Rui Dong, Dr. Jan Kunc, Dr. Yike Hu, Dogukan Deniz, Dr. Huan Chao, Dr. Wenlong Yu, Andrei Savu, Meredith Nevius, Jean-Phillipe Turmaud, Owen Vail, Dr. Jeremy Hicks, Dr. Chris Malec, Dr. Britt Torrance. I would also specifically like to thank Owen Vail for all of his help preparing and measuring samples and I would like to thank Wenlong Yu and Huan Chao for their help making transport measurements. I also want to thank my brother, Sam Hankinson, and my parents John and Gail Hankinson, for all of their support.

TABLE OF CONTENTS

LIST OF FIGURES

LIST OF SYMBOLS AND ABBREVIATIONS

τ_{sf}	Spin lifetime
l_{sf}	Spin diffusion length
σ	Conductivity
P	Spin Polarization
AFM	Atomic Force Microscopy
LFM	Lateral Force Microscopy
C-AFM	Current Atomic Force Microscopy
EFM	Electrostatic Force Microscopy
EG	Epitaxial Graphene
SLG	Single-layer Graphene
MLG	Multi-layer Graphene
TMR	Tunnel Magnetoresistance
JMR	Junction Magnetoresistance
MTJ	Magnetic Tunnel Junction
EG	Epitaxial Graphene
CVD	Chemical Vapor Deposition
GNR	Graphene Nanoribbon
CCS	Confinement Controlled Sublimation

SUMMARY

Over the past decade there has been a great deal of interest in graphene, a 2-dimensional allotrope of carbon with exceptional mechanical and electrical properties. Its outstanding mobility, minimal size, and mechanical stability make it an appealing material for use in next generation electronic devices. Epitaxial graphene growth on silicon carbide is a reliable, scalable method for the production of high quality graphene films. Recent work has shown that the SiC can be patterned prior to graphitization, in order to selectively grow graphene nanostructures. Graphene nanoribbons grown using this technique do not suffer from the rough edges caused by lithographic patterning, and recent measurements have revealed extraordinary transport properties. In this thesis the magnetic properties of these nanoribbons are investigated through spin polarized current injection. The sensitivity of these nanoribbons to spin polarized current is interesting from a fundamental physics standpoint, and may find applications in future spintronic devices.

CHAPTER 1

INTRODUCTION

1.1 Graphene Properties and Bandstructure

Graphene is a two dimensional allotrope of carbon composed of a single atomic layer of carbon atoms bonded together in a honeycomb lattice. Its unit cell is made up of two carbon atoms differentiated as A and B sublattice atoms as depicted in figure 1.1. The in-plane bonding between carbon atoms is an extremely strong sp^2 covalent bond giving graphene exceptional mechanical strength. The 4th valence electron of each carbon atom is in a delocalized π-orbital, free to move about the graphene sheet, and is responsible for its exceptional electronic properties.

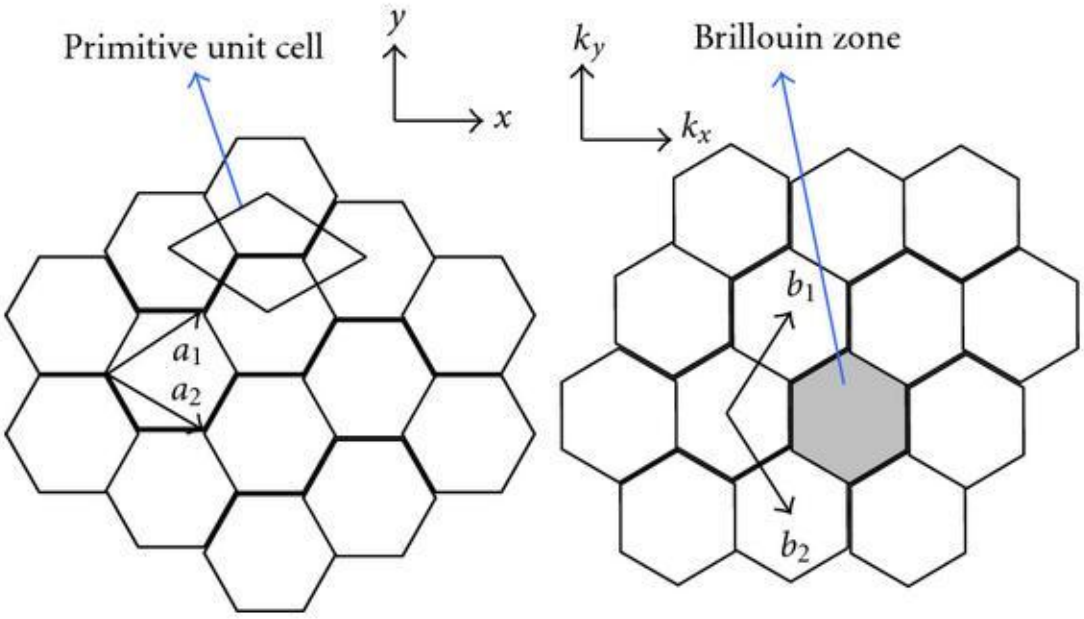

Figure 1.1: The primitive unit cell and lattice vectors in real space and the Brillouin zone of graphene in k-space, from ref [1]

The band-structure of graphene was first described with a tight binding model by Wallace in 1947 [2]. The dispersion relation resulting from the nearest neighbor tight binding approximation is:

$$E(\boldsymbol{k}) = \pm t\sqrt{1 + 4\cos^2\left(\frac{k_y a}{2}\right) + 4\cos\left(\frac{k_y a}{2}\right)\cos\left(\frac{\sqrt{3}k_x a}{2}\right)} \qquad (1.1)$$

In this equation t is nearest neighbor hopping energy, approximately 2.8eV in graphene, a is the in plane lattice constant, 2.46Å, and the ± accounts for the π and π* bands [3]. The valence and conduction bands meet at the six corners of the hexagonal Brillouin zone, labeled **K** or **K'** points, as illustrated in figure 1.2.

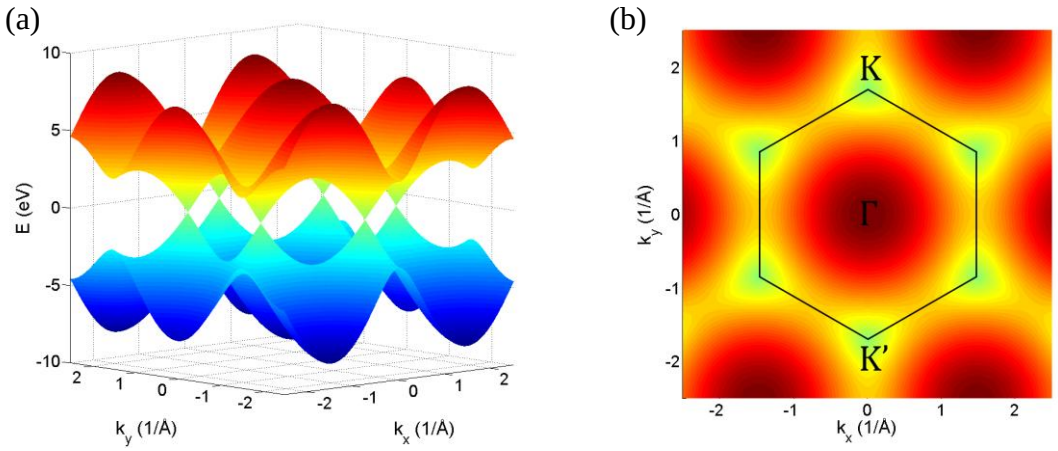

Figure 1.2: (a) Nearest neighbor tight binding approximation of the graphene band structure according to equation 1.1 with t=2.8eV. (b) 2D view of the band structure depicting the Brillouin zone and the **K**, **K'**, and **Γ** points.

At the **K** and **K'** points, near charge neutrality, the energy bands take on a nearly conical structure with a linear dispersion relation that can be approximated as

$$E(\boldsymbol{q}) \approx \pm v_F|\boldsymbol{q}| + O((q/K)^2) \qquad (1.2)$$

where $v_F \simeq 1 \times 10^6 m/s$ is the Fermi velocity and $\boldsymbol{q}$ is the momentum measured relative to **K** (or **K'**), i.e. $\boldsymbol{k} = \boldsymbol{K} + \boldsymbol{q}$ and $|\boldsymbol{q}| \ll \boldsymbol{K}$ [3]. Because of this unique linear dispersion relation, the charge carriers in graphene are often referred to as massless Dirac fermions [4] and compared to photons and neutrinos, which travel at a constant speed, *c* (the speed of light), and have no mass.

The 2-component electron wave function, $\psi(\boldsymbol{r})$, obeys the 2D Dirac equation near the **K** and **K'** points [3]:

$$-iv_F\boldsymbol{\sigma}\cdot\nabla\psi(\boldsymbol{r}) = E\psi(\boldsymbol{r}) \tag{1.3}$$

In momentum space, the wave function around the **K** point has the form:

$$\psi_{\pm,\boldsymbol{K}}(\boldsymbol{k}) = \frac{1}{\sqrt{2}}\begin{pmatrix} e^{-i\theta_k/2} \\ \pm e^{i\theta_k/2}\end{pmatrix} \tag{1.4}$$

for $H_k = v_F\boldsymbol{\sigma}\cdot\boldsymbol{k}$, and around the **K'** point has the form:

$$\psi_{\pm,\boldsymbol{K'}}(\boldsymbol{k}) = \frac{1}{\sqrt{2}}\begin{pmatrix} e^{i\theta_k/2} \\ \pm e^{-i\theta_k/2}\end{pmatrix} \tag{1.5}$$

for $H_k = v_F\boldsymbol{\sigma}^*\cdot\boldsymbol{k}$. Here $\boldsymbol{\sigma}$ and $\boldsymbol{\sigma}^*$ are Pauli matrices: $\boldsymbol{\sigma} = (\sigma_x, \sigma_y)$, $\boldsymbol{\sigma}^* = (\sigma_x, -\sigma_y)$. θ_k is the angle in momentum space defined as $\theta_k = \arctan(q_x/q_y)$. The ± signs correspond to the eigenenergies $E = \pm v_F k$ and to the π and π* (bonding and anti-bonding) bands. Because of the mathematical similarity to spin, the band designation is often referred to as pseudospin. The direction of this pseudospin can be related to momentum using the helicity operator:

$$\hat{h} = \frac{1}{2}\boldsymbol{\sigma}\cdot\frac{\boldsymbol{p}}{|\boldsymbol{p}|} \tag{1.6}$$

Based on this definition of $\hat{h}$ it is apparent that the states $\psi_{\boldsymbol{K}}(\boldsymbol{r})$ and $\psi_{\boldsymbol{K'}}(\boldsymbol{r})$ are eigenstates of $\hat{h}$:

$$\hat{h}\psi_{\boldsymbol{K}}(\boldsymbol{r}) = \pm\tfrac{1}{2}\psi_{\boldsymbol{K}}(\boldsymbol{r}), \quad \hat{h}\psi_{\boldsymbol{K'}}(\boldsymbol{r}) = \mp\tfrac{1}{2}\psi_{\boldsymbol{K'}}(\boldsymbol{r}) \tag{1.7}$$

This implies that $\boldsymbol{\sigma}$ has two eigenstate values with one parallel to momentum $\boldsymbol{p}$ and one anti-parallel to $\boldsymbol{p}$. Thus, the pseudospin gives the states chirality near the Dirac point as shown in figure 1.3.

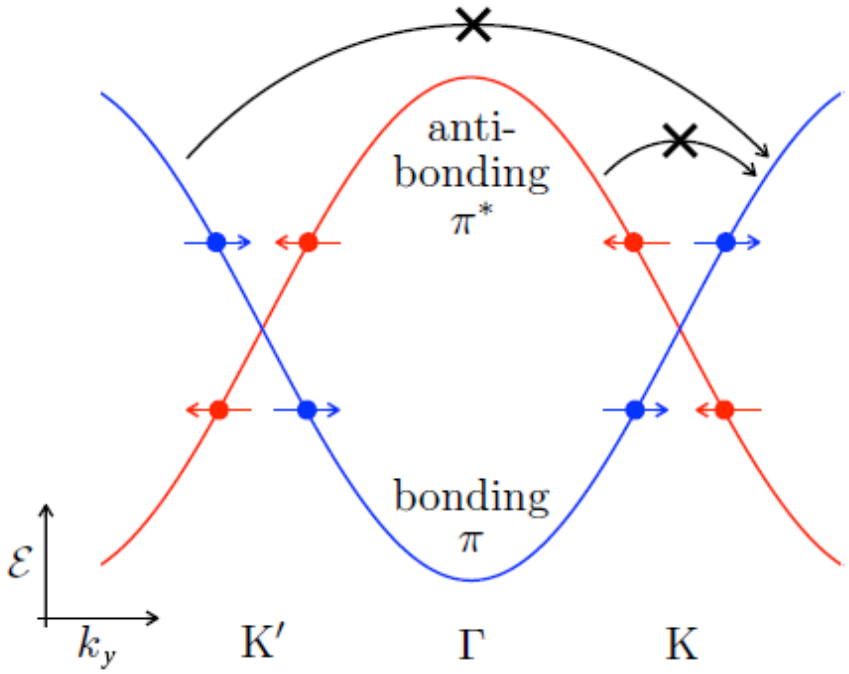

Figure 1.3: A 2D slice of the graphene band structure between the K' and K points through the Γ point. The pseudospin of the particles is denoted by the red and blue coloring and corresponding arrows. Pseudospin conservation inhibits intra-valley scattering (the small arrow at the top right) and the large change in momentum limits inter-valley scattering (the large arrow across the top). [5]

Pseudospin is not just an abstract mathematical construct, it has significant implications for transport. For a particle to reverse its own momentum through intra-valley scattering it would also have to reverse its pseudospin, but this is generally disallowed due to pseudospin conservation [6]. While this prevents scattering due to long-range disorder, short range potentials can flip the psuedospin and lead to intra-valley scattering [6,7]. The other option for a charge carrier to reverse its momentum would be to scatter from one valley to another, which would allow the carrier to conserve its pseudospin. Although pseudospin is conserved in inter-valley scattering, the large change in momentum required generally prevents such scattering. However, atomically sharp potentials/defects and ribbon edges can result in inter-valley scattering [8].

The high mobility of graphene can be diminished by dephasing of carriers caused by electron-phonon interactions or electron-electron interactions. Electron-phonon scattering in graphene has been found to be weak [9]. However, the electron-electron interaction can become significant as the carrier concentration increases [10,11].

Graphene's relativistic dispersion relation and the suppression of scattering due to pseudospin conservation[6] results in very high mobility [12,13]. Its high mobility combined with its exceptional mechanical properties makes it a very appealing material for future electronic devices. In addition, the relativistic nature of the particles makes it a very interesting platform from a pure physics perspective.

1.2 Graphene Production Methods

Although theoretical calculations of the graphene bandstructure were published in 1947 [2], it was not until 2002 that its exceptional electronic properties were demonstrated experimentally, with seminal papers in 2004 at the Georgia Institute of Technology [14] and independently in 2005 by groups at the University of Manchester [4] and University of Columbia[15] following work on ultra thin graphite [16,17]. These initial experiments sparked great interest in graphene as a potential material for next generation electronics. Interestingly, the three groups fabricated their graphene samples through completely different methods. The Manchester and Colombia groups peeled apart layers of graphite, in a method known as mechanical exfoliation; while the de Heer group formed graphene films on the surface of silicon carbide through a high temperature epitaxial growth technique demonstrated previously by van Bommel, Forbeaux, and others [18,19]. In addition to these two methods, graphene can also be formed through chemical vapor deposition (CVD)[20] and by reduction of graphene oxide [21,22].

Mechanical exfoliation is an appealing method for the production of graphene due to its simplicity. The method includes any number of techniques used to peel apart graphite into thin films. Graphite can be rubbed against a hard surface [23], or Scotch tape can be used to repeatedly peel apart graphite [16,24]. The resulting graphitic thin films can then be transferred to a substrate for identification and measurement [23]. Typically, a silicon wafer with a ~300nm thick silicon oxide layer is used as it allows for easy optical identification of single layer graphene flakes [23,25]. While this method can be used to provide samples for research, it is not scalable, which limits its usefulness for applications in industry [26]. Moreover, the method is inherently "dirty" from a surface science perspective and the deposited films are typically randomly strained and contaminated with charge puddles [27].

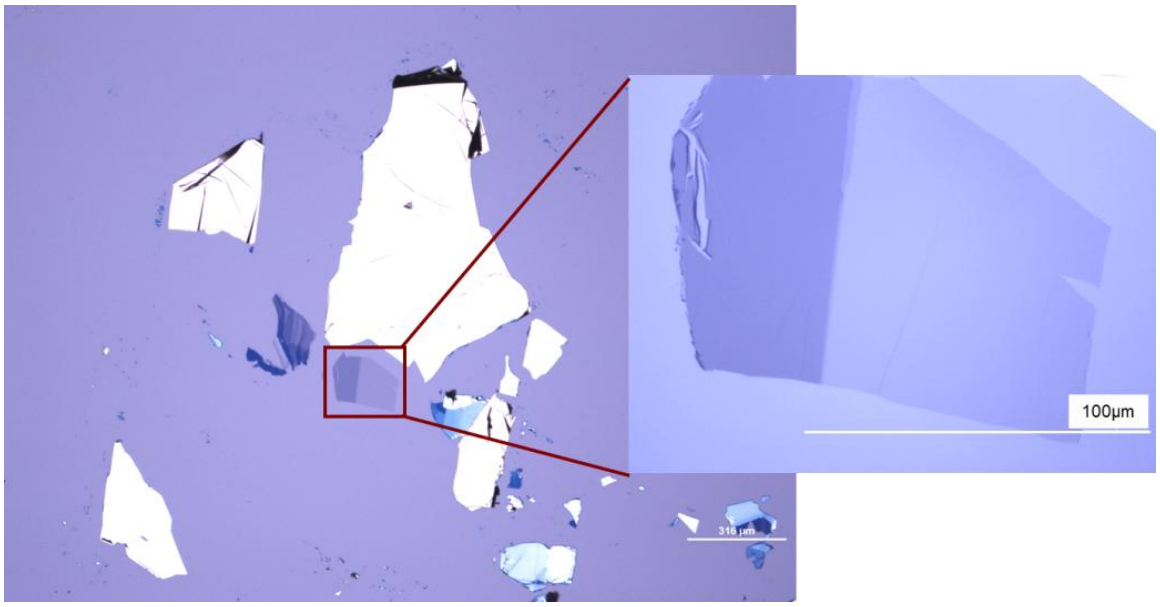

Figure 1.4: Optical image of exfoliated graphene on a silicon wafer with a 290nm thick oxide layer. The inset shows an enlarged view of the monoloayer graphene. From ref [28].

CVD is another method commonly used for the production of graphene films [20]. CVD growth of graphene is typically accomplished through thermal decomposition

of hydrocarbons on transition metal substrates. CVD graphene growth has been demonstrated on Cu [29], Ni [30], Ru [31], and Ir [32]. One advantage of CVD growth is that very large graphene sheets can be formed. Films up to 30 inches wide have been fabricated using CVD [33]. Unfortunately, because CVD growth is performed on metallic substrates, the graphene must be transferred to another substrate for transport measurements or use in electronic devices. In addition, CVD graphene has typically suffered from small domain sizes that reduce mobility [34]. However, there has been considerable research into increasing the size of CVD graphene domains, and significant improvements have been made [35,36].

Another method for graphene production is the reduction of graphene oxide. In this technique graphite is oxidized, which results in reduced coupling between layers and allows the oxidized graphene layers to separate and break up into thin flakes [21]. Sonication of the graphite oxide is often used to further separate the graphite oxide layers [21]. After separation the resulting graphene oxide layers can be transformed into graphene through chemical reduction [21] or thermal annealing [37]. This method can be used to form large quantities of graphene, but the process introduces defects that lower the mobility of the resulting graphene films [21].

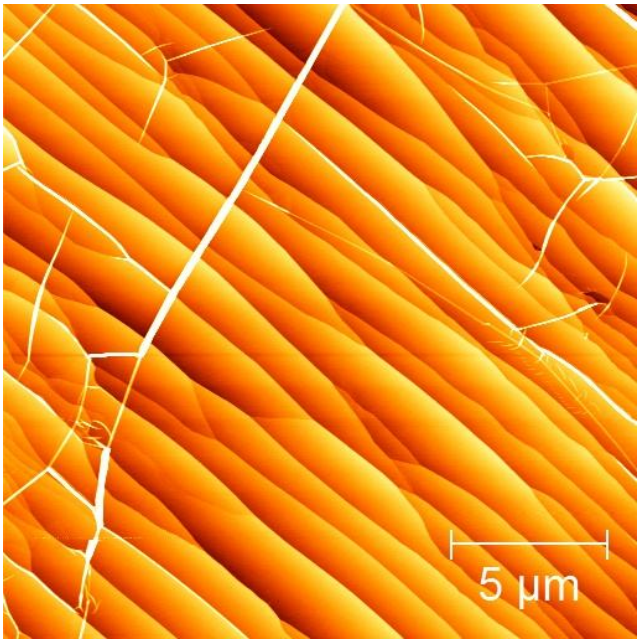

Figure 1.5: Epitaxial graphene on the SiC C-face. The diagonal steps are SiC surface steps, and the white lines are pleats in the graphene sheets that form during cool down due to the different thermal expansion coefficients of graphene and SiC.

The method used to produce graphene in this work is epitaxial growth on silicon carbide. In this growth technique, SiC crystals are heated until thermal decomposition begins on the surface. Si sublimation leaves behind excess carbon that forms graphene sheets. The formation of graphitic thin films through thermal decomposition of SiC was reported by van Bommel et al. in 1975 [18]. In 2004 the de Heer group demonstrated that this technique could be used to form high mobility graphene sheets [14]. Epitaxial growth is a very appealing production method, as it forms very high quality graphene on a crystalline substrate. It is also scalable on commercially available substrates, providing a path toward wafer scale production of graphene for use in electronics. In addition, SiC pre-patterning allows for growth of graphene nano-structures. The epitaxial growth technique is discussed in depth in chapter 3.

1.3 Thesis Outline

Chapter 2 gives an overview of the tools and techniques used to characterize epitaxial graphene as well as the methods used to create the graphene devices used for transport measurements. In chapter 3, the details of epitaxial growth are explored. The confinement controlled sublimation (CCS) technique is explained in detail and the use of SiC pre-patterning for the creation of graphene nanostructures is discussed. Chapter 4 provides relevant background information on spin dependent transport and discusses some of mechanisms that can lead to magnetism in graphene. Chapter 5 presents the results of transport measurements on epitaxial graphene nanoribbons. It will focus specifically on measurements of spin dependent tunneling into epitaxial graphene nanoribbons. The results of these measurements were quite complicated and varied from sample to sample. Thus, chapter 5 presents each sample individually to give a clear picture of the graphene growth and resulting transport observed in each. Hopefully, the careful documentation of the transport measurements presented here will lead to eventual understanding of the underlying physics. The last chapter will highlight the key observations made and suggest future experiments that can be done to gain further insight into the nature of the transport in these graphene nanoribbons (GNR).

CHAPTER 2

EXPERIMENTAL METHODS

2.1 Scanning Probe Microscopy

2.1.1 Atomic Force Microscopy

Atomic force microscopy (AFM) is a powerful scanning probe microscopy (SPM) technique widely used for surface topography measurements [38]. AFM utilizes a cantilever with a sharpened tip that scans the sample surface line by line. The relative position of the sample and the scanning probe is controlled by a set of piezoelectric crystals as shown in figure 2.1. In the Park XE-70 used in this thesis, the Z scanner is completely separated from the X-Y scanner allowing for more precise vertical control of the probe [39]. As the cantilever scans across the sample surface, forces acting on the tip cause a deflection of the cantilever. This deflection is measured by reflecting a laser beam off of the cantilever's top surface to a position-sensitive photodiode (PSPD). The PSPD sensitively detects changes in the laser's position allowing the system to measure the forces acting on the tip and thus gain information about surface topography and roughness as shown in figure 2.1. This technique allows for extremely precise vertical resolution on the order of 1Å. The lateral resolution is dependent on the tip sharpness. A nanoscopically sharp tip (such as the SSS-NCHR) can yield horizontal resolution on the order of a few nanometers; however, many tips, especially those coated with a conducting metal layer, will be unable to resolve such fine details. This is especially important to consider when measuring steep sidewalls as a worn tip will make step edges appear less steep.

A wide variety of tips were used in this work depending on the application. The most commonly used tip for this work is the Point Probe Plus PPP-NCHR tip with a typical radius of curvature below 7nm. However, when finer horizontal resolution is required, the supersharp SSS-NCHR tip with a radius of curvature below 2nm can be used. For electrical measurements, tips coated with a 25nm thick double layer chromium and platinum iridium5 (PPP-EFM or PPP-ContSCPt tips) are used. The coating results in a radius of curvature of approximately 30nm. It is important to note that over time these tips can wear down, further reducing lateral resolution. Three different AFMs were used in this work: the Park Systems Autoprobe CP, the Veeco diCP-II, and the Park Systems XE-70. The XE-70 is the newest and most advanced of the three and most of the images presented in this thesis were taken with it.

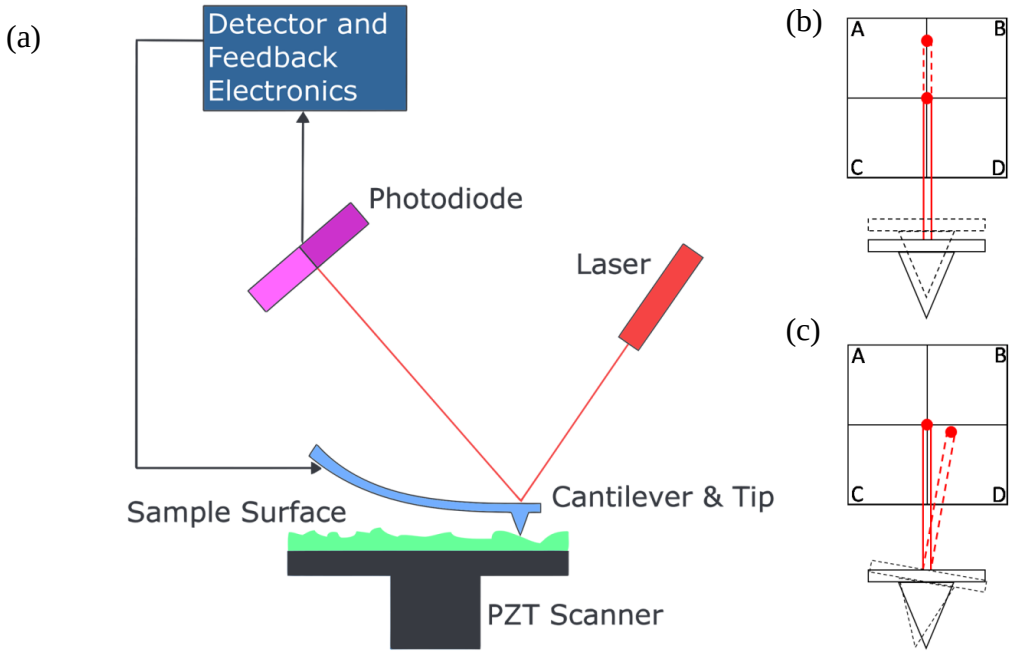

Figure 2.1: (a) Schematic showing the basic components used in atomic force microscopy. The 4-segment photodiode can detect both vertical displacement (b) and lateral displacement (c). Public domain image obtained from the Wikimedia Commons

Atomic force microscopy can be divided into two major categories: contact or non-contact mode. In contact mode, the tip sample interaction is governed by short-range interatomic repulsive forces. The force between the tip and sample is typically very small, on the order of 1-10nN; however, the spring constant of the cantilever is usually less than 1N/m letting it sensitively respond to these minute forces [39]. As the tip approaches the sample, the repulsive electrostatic force causes the cantilever to bend. The vertical deflection of the cantilever, detected using the laser and PSPD (figure 2.1b), is proportional to the force between the tip and the sample. Thus, along with knowledge of the cantilever's spring constant, this deflection can be used to measure the force between the tip and the sample. As the tip scans across the sample surface, a feedback loop maintains a constant force between the tip and sample by moving the sample vertically and the surface topography is tracked [40].

In non-contact mode, the cantilever is vibrated perpendicular to the sample plane, at a frequency just above the cantilever's resonant frequency. As the tip approaches the sample surface, it will experience small attractive van der Waals forces due to the dipole-dipole interaction between the tip and the sample. This attractive force will cause a decrease in the effective spring constant and a corresponding decrease in the resonant frequency. This shift in resonant frequency will result in the fixed oscillation frequency being further from resonance causing a decrease in the oscillation amplitude as shown in figure 2.2 [39]. A feedback loop moves the sample up and down using the Z piezo in order to maintain a constant oscillation amplitude and hence a constant tip-sample separation distance. In this way, the surface topography can be measured with minimal

force applied to the sample surface, which has the advantages of reducing tip wear and preventing any damage to the sample surface.

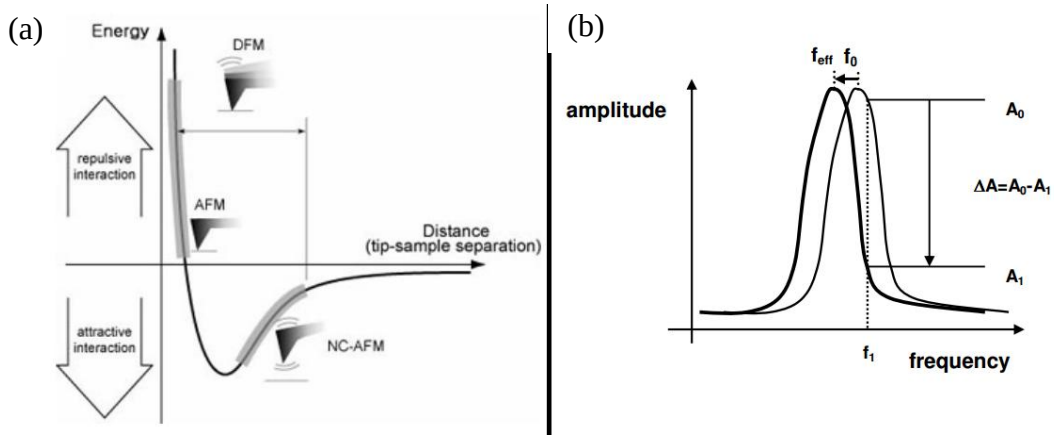

Figure 2.2: (a) Relationship between force and separation distance as it pertains to different AFM operating modes [39]. (b) Shift in resonant frequency due to van der Waals forces and the corresponding change in oscillation amplitude [39].

2.1.2 Current AFM

Current AFM (C-AFM) is an advanced contact mode technique used to measure the electrical properties of the sample surface. For a C-AFM measurement, a conductive tip is used to scan the surface while a constant voltage is applied between the tip and the sample. The current flowing from the tip to the sample is measured during the scan allowing one to map the conductivity on the surface at the same time as the topography. When working with graphene grown on insulating silicon carbide, it is necessary to ground the graphene in order to complete the circuit. Hence, this technique is typically only applied to samples that have had electrical contacts patterned on them that can be used to ground the sample.

2.1.3 Electrostatic Force Microscopy

Electrostatic Force Microscopy (EFM) is a technique used to map the electric properties of the sample surface in addition to measuring surface topography. During an

EFM measurement, the electrostatic force between the tip and the sample surface is measured using a biased conductive AFM tip. EFM can reveal information about the surface potential and charge distribution. During an EFM measurement, the tip response is influenced by electrostatic forces as well as the normal van der Waal forces used for topography measurements. The influence of these two forces must be distinguished from one another in order to properly interpret the data. One method to accomplish this is to take advantage of the differing length dependence of the van der Waals forces, which are proportional to $1/r^6$, and the electrostatic forces, which are proportional to $1/r^2$. In this basic method, known as standard EFM, each line of the sample is scanned twice. The first scan (to measure the topography) is taken close to the sample surface where the van der Waals forces dominate. The second scan is done at a larger separation distance where the electrostatic forces dominate. A constant distance is maintained between the sample and the tip using the topography data during this scan to minimize the effects of sample topography on the electrostatic data. This method has the obvious disadvantage of doubling the scan time.

One alternative EFM method, known as enhanced EFM, uses a lock-in amplifier to apply an AC bias to the tip during a non-contact mode scan. The electrostatic force between the sample and the tip during such a measurement is given by equation 2.1 [41].

$$\begin{aligned} F(t) = (C/d) \times \left[(V_{DC} - V_s)^2 + \frac{1}{2}{V_{AC}}^2\right] \\ + 2 \times (C/d) \times (V_{DC} - V_s) \times V_{AC} \sin(\omega t) \\ - \frac{1}{2}(C/d) \times {V_{AC}}^2 \cos(2\omega t) \end{aligned} \tag{2.1}$$

C is the capacitance between the tip and sample, d is the separation distance, V_{DC} is the DC bias applied to the tip, V_{AC} is the AC bias, V_S is the surface potential of the sample, ω

is the lock-in frequency, and *t* is time. The force can be divided into three parts: a DC component that arises from the van der Waals interaction between the tip and the sample, an AC component with frequency ω that reflects the sample's electrostatic properties, and an AC component with frequency 2ω that reflects the capacitive properties of the sample [39]. The separation distance is kept constant by the normal non-contact mode feedback loop and the lock-in amplifier is used to isolate and measure the ω signal. This allows simultaneous measurement of the sample's topography and electrostatic properties. However, one must be careful when performing these measurements and interpreting the results. If the tip does not respond quickly enough to a change in topography, the change in separation distance will be picked up in the EFM signal showing a false change in surface potential. When done correctly, this technique is useful for distinguishing graphene from silicon carbide due to the different work functions of the materials. This is the primary EFM mode used in this work.

2.1.4 Lateral Force Microscopy

Lateral force microscopy (LFM) is a contact mode SPM technique that measures the frictional force of the tip against the sample as it scans across the surface. It does so by tracking the lateral displacement of the cantilever in addition to the vertical displacement used for topography as shown in figure 2.1 (c). The direction of the displacement due to frictional forces depends on the scan direction so the scan direction must be known for proper interpretation of the results. Typically, the sample is scanned in both directions and the difference in displacement between the two scans is analyzed to reveal information about the frictional force across the surface. Surface steps can also cause lateral deflection of the cantilever, so knowledge of the topography is necessary to

distinguish topological effects from the frictional effects. Graphene has been observed to have a lower coefficient of friction than that of SiC, making LFM a useful tool for determining graphene coverage on flat SiC surfaces.

2.2 Ellipsometry

Ellipsometry is a versatile, non-destructive thin-film characterization technique that can be used to measure the thickness or optical properties of a variety of materials. Ellipsometry works by analyzing the change in polarization of light reflected off of the sample surface. The incident light is typically linearly polarized and can be divided into the s-component, which oscillates parallel to the plane of the sample, and the p-component, which oscillates parallel to the plane of incidence (see figure 2.3). The reflected light is measured and the change in polarization, ρ, is expressed in terms of Ψ and Δ, which relate to the change in amplitude and phase shift as shown in equation 2.2 [42]. R_s and R_p represent the intensities of the reflected s and p components. This change is dependent upon both the film thickness and the optical constants of the material and substrate being measured. In order to obtain accurate thickness measurements a suitable optical model of the material being measured is required. The optical constants used for graphene were obtained from Jellison's measurements on highly ordered pyrolytic graphite [43]. The silicon carbide was measured directly and fit using a Cauchy model to determine the refractive index.

$$\rho = \frac{R_p}{R_s} = tan(\Psi)e^{i\Delta} \tag{2.2}$$

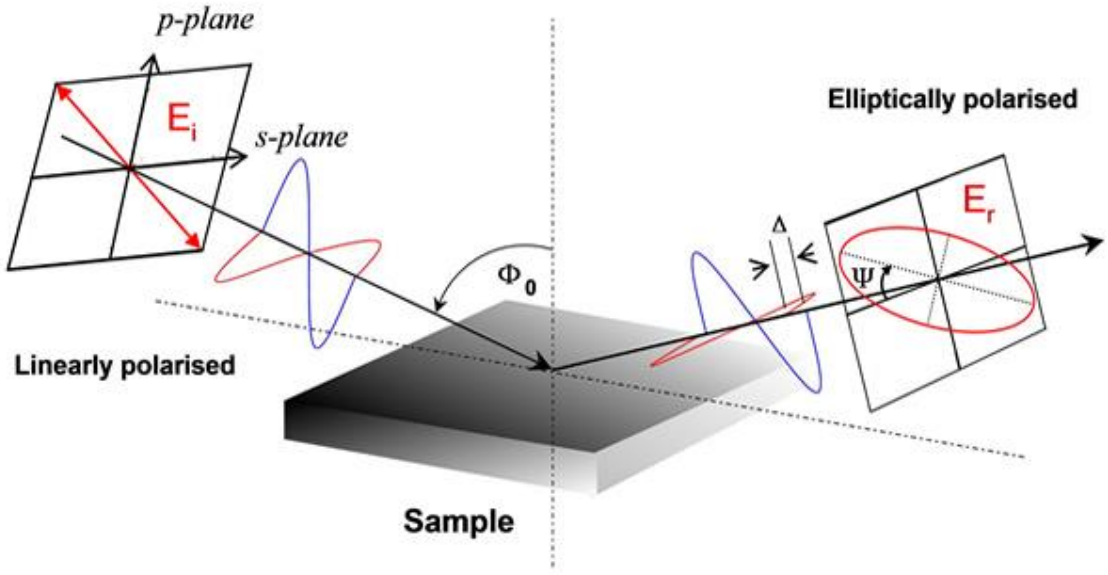

Figure 2.3: Linearly polarized light is reflected off of the sample surface resulting in elliptically polarized light measured by the ellipsometer and characterized in terms of the azimuth angle, Ψ, and relative phase difference, Δ. Image reproduced from ref [44]

In this work, a Horiba Jobin Yvon Auto SE was used to measure the thickness and uniformity of graphene grown on the silicon carbide surface. The Auto SE has a spectral range of 440 to 1000nm and works with a fixed angle of incidence. The minimum spot size for this system is 25µm x 60µm, allowing for large-scale mappings but preventing its use for nanometer scale uniformity measurements.

2.3 Raman Spectroscopy

Any molecular system will have characteristic vibrational and rotational modes that are dependent on the bond strength, atomic mass, and structure of the system. Raman spectroscopy is a spectroscopic technique used to gain vibrational information about the system [45]. Briefly, in this technique, a sample is exposed to monochromatic light that can undergo elastic Raleigh scattering or inelastic Raman scattering. The elastically scattered light at the incident wavelength is filtered out so that the remaining radiation that has undergone inelastic scattering can be analyzed. The change in energy

of the inelastically scattered light measured with Raman spectroscopy corresponds to the energy of one of the system's phonon modes. The light can either excite the molecule into a higher energy state, resulting in a lower energy photon exiting the system through a process known as Stokes scattering; or the molecule can relax into a lower energy state than it was in prior to the absorption, releasing a higher energy photon through a process known as anti-Stokes scattering. In this work, a Horiba Jobin Yvon Labram HR-800 Raman spectrometer with a 532nm excitation laser and ~1μm^2 beam size was used to characterize graphene films grown on silicon carbide.

In graphene, the Stokes phonon energy shift results in three major peaks in the Raman spectrum [46]: the G peak at 1580cm^{-1}, the D peak at 1350cm^{-1}, and the 2D peak at 2690cm^{-1} when measured with a 532nm excitation laser [47]. The G peak results from a high frequency in plane vibrational mode corresponding to the E_{2g} phonon and can be observed in pristine graphene [45]. The D peak results from the A_{1g} breathing mode of 6 atom rings and can only manifest near the edges or defects in the graphene lattice [45,48]. The 2D peak is an overtone of the D-peak resulting from two phonons with opposite wave vectors [45]. Because the opposite wave vectors of these two phonons satisfy conservation of momentum, the 2D-peak can be observed in pristine graphene even though the D-peak will not be present [45].

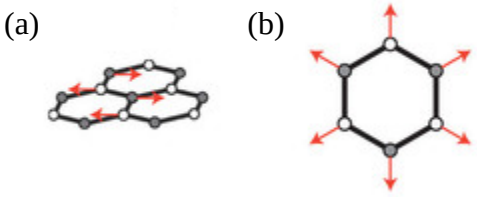

Figure 2.4: (a) The E_{2g} phonon mode responsible for the G peak. (b) The 6-atom A_{1g} breathing mode responsible for the D and 2D peaks. Reproduced from ref [45]

The size and shape of these three peaks can reveal a great deal of information about the graphene being measured, see for example Ferrari & Basko [45]. Since the A_{1g} breathing mode requires lattice defects or grain boundaries to manifest, the intensity of the D peak relative to that of the G peak, which is unaffected as long as the sp^2 carbon bonding is still intact, can serve as a good indicator of the graphene quality [48]. Measurements away from the edges should yield an intensity ratio (I_D/I_G) close to zero for high quality graphene.

The shape, position, and intensity of the G and 2D peak can also be used as indicators of the doping of a graphene sheet [49]. Both electron and hole doping shift the G-peak to higher energies. However, the 2D peak shifts toward higher energies for hole doping but remains relatively constant for electron doping up to a concentration of approximately $3.2 \times 10^{13} cm^{-2}$, at which point the peak position begins shifting down in energy [49] as shown in figure 2.5. In addition to a change in peak position, the peak shape can also be affected by doping. The G peak becomes more narrow and increases in intensity with increasing carrier concentration for electrons or holes, while the 2D peak becomes broader and less intense for increasing carrier concentration [49]. Hence, the relative intensity and width of the 2D peak compared to that of the G peak can be used as another indicator of the doping level. The intensity ratio, I(2D)/I(G), will be the largest for neutral graphene and decrease with an increase in doping [49].

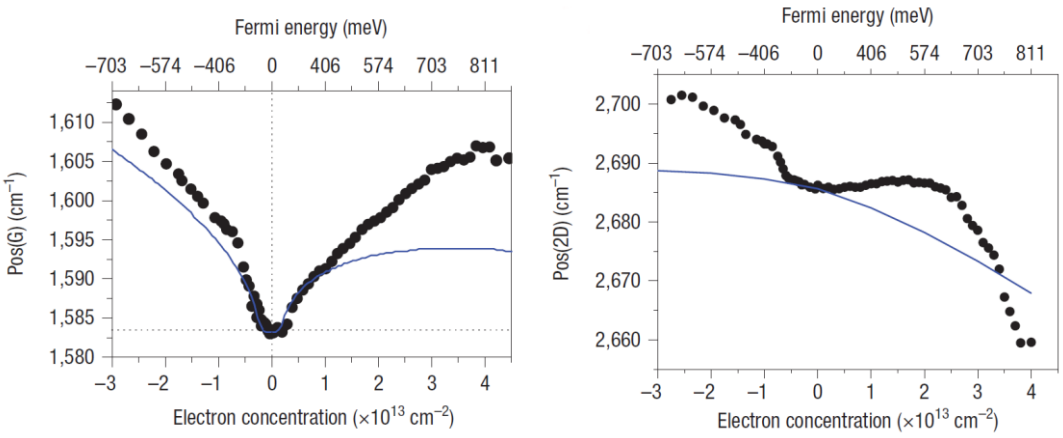

Figure 2.5: The position of the G peak (left) and 2D peak (right) as a function of carrier concentration. The data was taken on graphene produced by micromechanical cleavage using a 514.5nm excitation laser. Reproduced from ref [49]

When measuring graphene on silicon carbide it is important to differentiate the graphene spectrum from the silicon carbide spectrum. Silicon carbide has a number of Raman active peaks in the same energy range as graphene as shown in figure 2.6. To extract the pure graphene spectrum one must subtract the SiC background spectrum. To obtain a good SiC background spectrum one can adjust the focal depth of the Raman spectrometer to measure the silicon carbide directly underneath the graphene being measured. If this measurement is not possible, another SiC Raman spectrum can be used as a reference. The height of the pure SiC Raman spectrum is matched to that of the combined graphene-silicon carbide spectrum in a region where the graphene does not have a peak, such as the shoulder of the SiC peak near 1900cm^{-1}. After matching the height of the spectra, the background subtraction can be performed.

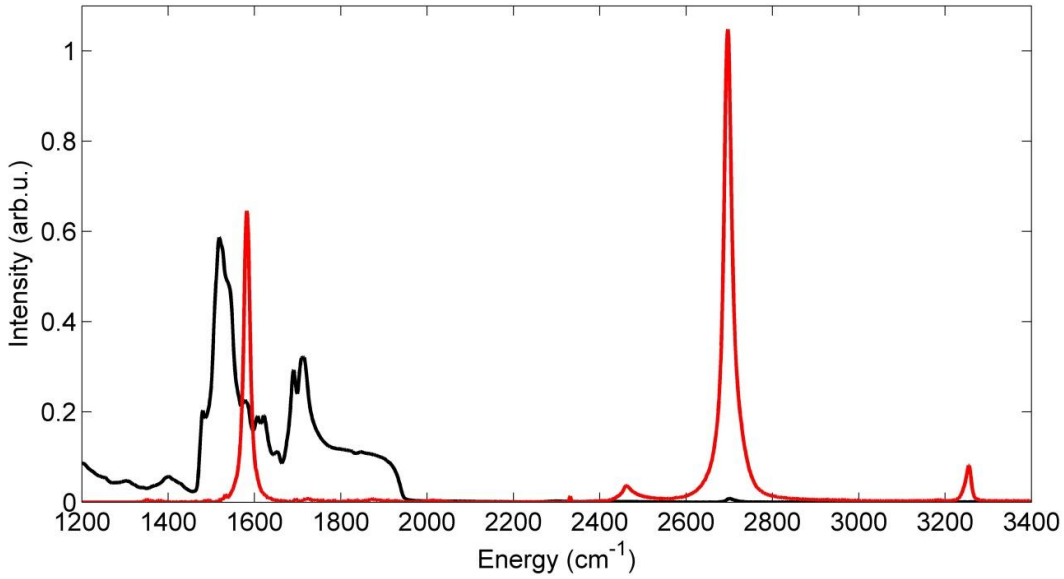

Figure 2.6: The graphene spectrum (red) and silicon carbide spectrum (black) overlap requiring decomposition of the combined spectrum into its constituent parts. Figure provided by Jan Kunc.

Basic subtraction has limitations and can lead to poorly defined spectra with spectral regions of negative intensity [50]. To better separate the two spectra one can use the non-negative matrix factorization technique, which provides well defined non-negative decomposed spectra [50]. In this technique, multiple Raman spectra are taken at different focal depths. The relative intensity of the graphene and SiC signals vary as a function of focal depth allowing one to decompose the combined spectra into basis functions representing the individual graphene and SiC spectra [50]. This provides a much cleaner graphene spectrum, but requires multiple measurements, which increases data collection time.

2.4 Device Fabrication

2.4.1 Electron Beam Lithography

Electron beam (e-beam) lithography is a fabrication technique used to create nanoscale patterns. The process utilizes an electron-sensitive material (resist) that

changes its solubility properties based on the energy deposited by an electron beam [51]. First, the entire surface of the substrate is covered with an e-beam resist through spin coating. A pattern is then defined by selectively exposing the resist to a concentrated electron beam. After exposure, a developer is used to dissolve the exposed or unexposed portions of the resist (depending on the type of e-beam resist used) creating a custom nanoscale mask. Another material can then be selectively deposited onto the sample through the mask or the substrate can be etched in the exposed areas (figure 2.7). Afterward, the remaining resist is removed with a suitable solvent.

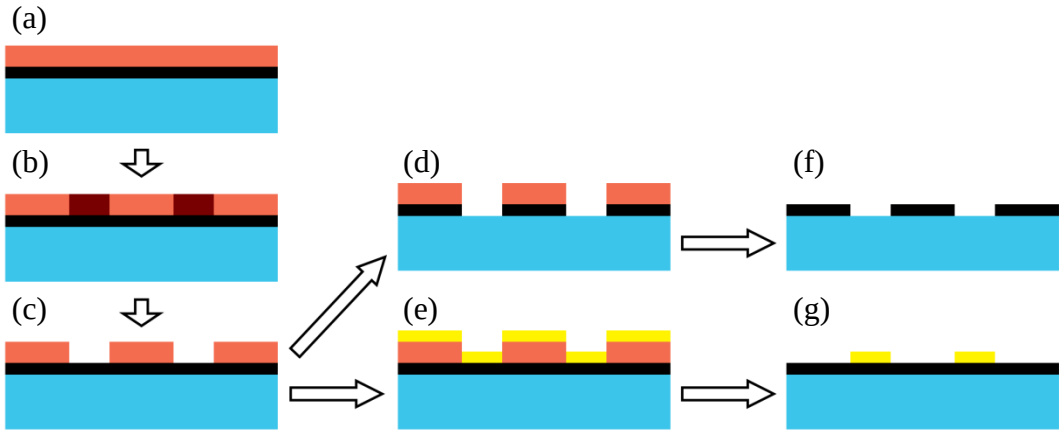

Figure 2.7: Electron beam lithography process. First e-beam resist (PMMA) is spin coated onto the surface of the sample (a). The resist is selectively exposed to the electron beam (b) and then developed to remove the exposed resist (c). Afterwards exposed surfaces can be etched (d) or a thin film can be deposited through the mask (e). Finally a solvent (acetone) is used to remove any remaining resist (f) and (g).

The choice of resist is an important consideration when doing e-beam lithography. Resists can be divided into two main categories: positive tone resists, which dissolve in the region exposed to the electron beam, and negative tone resists, which dissolve in the unexposed region. In this work, patterning was done primarily using a 6% solution of 950,000 molecular weight polymethyl methacrylate dissolved in anisole (PMMA 950 A6), a commonly used positive tone resist. The patterns were written with a JEOL JSM-

5910. This system has a maximum resolution of 3nm for imaging. However, for lithography the minimum feature size obtainable with the system used is approximately 50nm and for good metal liftoff the minimum feature size of the contacts was kept above 200nm.

2.4.2 Reactive Ion Etching

Reactive ion etching (RIE) is a type of dry etching commonly used for nanofabrication. In this process, a chemically reactive plasma is generated by using an electromagnetic field to ionize one or more input gases. The choice of gas is dependent on the material being etched. For graphene, an oxygen plasma is used; while for etching of silicon carbide, gases such as sulfur hexafluoride (SF_6) or carbon tetrafluoride (CF_4) are typically used.

The plasma will attack any exposed surface so a mask is used to protect the sample surface where etching is not desired. The choice of mask material is important as it can also be etched during plasma etching. The relative rate of etching of the mask compared to the target material is known as the selectivity of the mask. For deep etches a high selectivity mask is needed, so a metal such as nickel is deposited before etching. However, for most shallow etches the mask can be composed of an e-beam resist or photoresist like PMMA.

2.4.3 Thin Film Deposition

Thin film deposition is used to provide metal contacts and tunnel barriers for measurement of patterned graphene structures. In this process, a source material is heated until it undergoes vaporization. The vaporized atoms will settle on exposed surfaces within the chamber. A mask is used to protect the parts of the sample surface where deposition is not desired. In this work, the most common mask material is PMMA

patterned using electron beam lithography. After deposition, a solvent (acetone) is used to remove the resist and the portion of the film lying on top of it.

For non-magnetic contacts used in this work Pd/Au contacts are deposited using an e-beam evaporator. A 20nm thick layer of Pd is deposited at 0.7 Å/s followed by 30nm of Au deposited at 1Å/s. For magnetic contacts a 20nm thick film of Co is deposited at 0.4 Å/s using an e-beam evaporator. Prior to the Co deposition a thin aluminum oxide layer is deposited to allow for efficient spin injection.

In order to prevent contamination and oxidation the deposition takes place in a high vacuum chamber. However, since the chamber is not a perfect vacuum there are still some water molecules present that can cause oxidation of metals as they are deposited. For most metals this oxidation rate is negligible. However, certain metals, such as aluminum, are more readily oxidized and can form oxides if deposition is done at a slow enough rate. In this work, slow deposition of aluminum, at 0.1Å/s, is used in order to create aluminum oxide tunnel barriers. The total thickness of aluminum deposited is 3-4 Å, resulting in a AlO_x layer approximately 1nm thick after oxidation [52].

CHAPTER 3

EPITAXIAL GRAPHENE GROWTH ON SILICON CARBIDE

It has long been known that thin graphitic films can be grown on the surface of hexagonal silicon carbide[18]. However, it was not until 2002 that the de Heer group first measured the electronic properties of these epitaxial graphene films and found that they showed remarkable 2D electron gas properties. These first results were reported in 2004 [14]. While the ease of creating small graphene flakes through mechanical exfoliation helped spur scientific study of the material, it does not provide a means of scalable commercial production of graphene. Growth of graphene films on silicon carbide however, does offer a possible path toward large-scale production of high-quality electronics grade material. In addition, silicon carbide is a useful semiconductor creating a system with the potential for integrated electronics using both the graphene and the silicon carbide itself.

3.1 Silicon Carbide

Silicon carbide is a wide band gap semiconductor commonly used in high temperature and high power electronic applications [53]. However, in this work it is used primarily as a high-quality crystalline substrate for epitaxial graphene. The SiC crystal can form a number of polytypes resulting in a variety of structural and electronic properties [54]. Some of the more common polytypes include the 4H and 6H polytypes, which have hexagonal crystal structures, and the 3C polytype, which has a cubic crystal lattice. The 4H and 6H hexagonal polytypes have been observed to allow for good epitaxial growth of graphene films and are the only polytypes used in this work.

Hexagonal SiC crystals are composed of stacks of atomically thin bi-layers consisting of equal numbers of silicon and carbon atoms bonded together as seen in figure 3.1. The layers have an interlayer bonding length of 2.5Å and an in plane lattice constant of 3.07Å [55]. The 4H and 6H polytypes have slightly different rotational stacking sequences resulting in 4 and 6 bi-layers respectively in a single unit cell. The polar [0001] axis results in a carbon terminated $(000\bar{1})$ face and a silicon terminated (0001) face. The majority of epitaxial graphene growth is done on one of these two crystal facets.

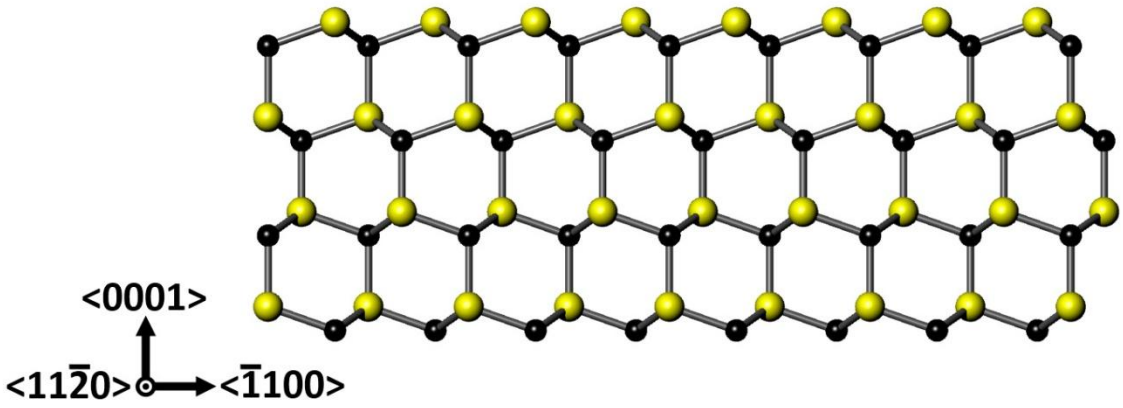

Figure 3.1: Side view showing 4 bi-layers of the 4H SiC crystal structure.

Silicon carbide can be doped with a number of different elements to modify its conductivity. For electronic transport measurements of epitaxial graphene, semi-insulating wafers are typically used so that transport through the substrate is not significant at room temperature. In this work, 4H semi-insulating SiC from Cree with average resistivity between $1x10^{8}\Omega$-cm and $1x10^{10}\Omega$-cm was used. The wafers used in this work were diced nominally on axis with miscut angles of approximately 0.1º to 0.3º. The face used for graphene growth undergoes chemical mechanical polishing (CMP) in order to remove large scratches and surface defects left behind during the wafer dicing.

The sample surface can be further improved by hydrogen etching, which is a high temperature annealing process under a flow of hydrogen gas [56]. During this process the surface restructures, creating atomically flat terraces arranged in a staircase structure as seen in figure 3.2. The orientation, terrace width, and step height depend on the miscut angle as well as the time, temperature and gas flow rate used during the hydrogen etching process.

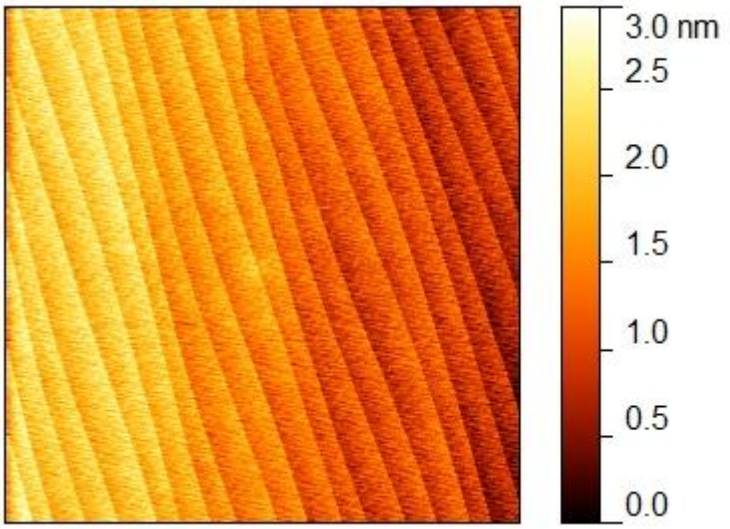

Figure 3.2: 20x20μm^2 image of the silicon carbide $(000\bar{1})$ face after hydrogen etching showing surface steps resulting from the slight miscut angle.

3.2 Graphene Formation Due to SiC Surface Sublimation

Early characterization of few layer graphene on the surface of silicon carbide was performed by van Bommel in 1975 [18]. Van Bommel noted that under high temperature annealing (800˚C) in UHV, graphitic thin films formed on both the (0001) and $(000\bar{1})$ faces of silicon carbide due to silicon sublimation. Using low energy electron diffraction measurements (LEED), he made the first observation of the $(6\sqrt{3} \times 6\sqrt{3})R30$ diffraction pattern that characterizes the commensurate graphene/SiC structure formed on the (0001) face [18]. $6\sqrt{3}$ denotes the length of the supercell edge in number of SiC unit vectors, and R30 refers to the 30˚ rotation between the supercell edge and the SiC lattice

vector. This consistent rotation between the graphene and the underlying SiC is important as it allows for control over the chirality of ribbons grown or patterned on the Si-face. Multiple layers grown on this face all share the same rotational orientation and follow Bernal stacking as in graphite. Because the electronic properties of few layer graphite differ from those of graphene, careful control of graphene thickness is required when working on the Si-face.

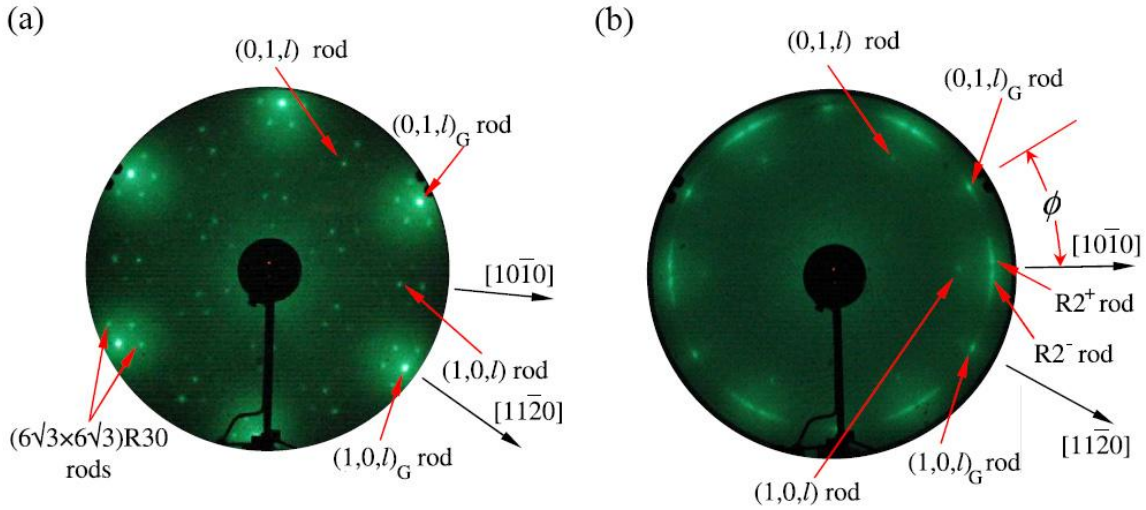

Figure 3.3: LEED patterns of epitaxial graphene on the (a) Si-face and (b) C-face of silicon carbide. Reproduced from [57]

Graphene grown on the carbon face follows a different stacking sequence with multiple allowed rotation directions relative to the underlying SiC. The LEED pattern (fig 3.3) shows graphene diffraction spots at $\phi = \pm 30°$ as well as a diffuse ring segment peaked at $\phi = \pm 2.2°$, indicating the preferred orientations of the graphene sheets relative to the underlying silicon carbide. These angles are interesting because -2.204˚, 2.204˚, and 30˚ all provide a nearly commensurate $(6\sqrt{3} \times 6\sqrt{3})R30$ cell with the underlying silicon carbide. In addition, a 32.204˚ rotation between graphene layers forms a commensurate $\left(\sqrt{13} \times \sqrt{13}\right)_G R46.1$ unit cell (in this case the cell edge lengths and

rotation are given in terms of the graphene lattice vector as denoted by the G subscript) [57]. So while these rotation angles may seem random at first glance, they actually allow for commensurate superstructures between graphene and SiC as well as between the graphene layers themselves. Furthermore, because the layers formed on the C-face are rotated relative to their neighboring layers, they do not follow Bernal stacking and have been demonstrated to behave as independent graphene layers [57].

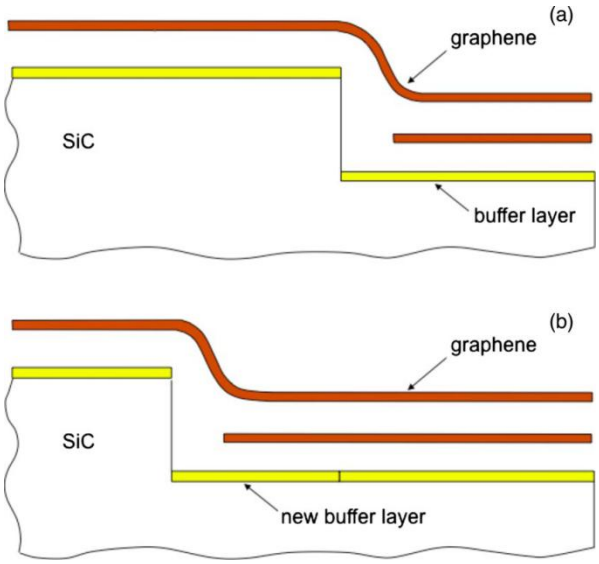

Figure 3.4: Graphene growth at a step on the (0001) face. New graphene forms as the SiC step edge recedes, reproduced from [58]

On both faces graphene forms from the C atoms left behind after the desorption of Si during thermal decomposition of the SiC crystal [55]. The formation of the epitaxial graphene films is believed to nucleate at SiC step edges on the Si-face [55,58,59]. During growth, the SiC surface recedes as the epitaxial graphene film forms as show in figure 3.4. During multi-layer growth new layers form underneath the fully formed graphene layers, resulting in continuous graphene sheets on the surface even if there is variation in the number of layers across the sample. Graphene sheets in multilayer films have different doping depending on their distance from the SiC substrate. The layers

closest to the SiC interface will be electron doped ($n \sim 10^{12}$-10^{13} cm^{-2}) due to the interface electric field, while layers further from the SiC interface are essentially undoped ($n < 10^{10} cm^{-2}$)[60].

While the growth mechanism on both faces is similar, the growth rates differ significantly. Under the same growth conditions graphene formation on the C-face occurs much more rapidly than on the Si-face. The difference in growth rate may be linked to the formation of a carbon rich buffer layer on the Si-face which is not seen on the C-face. The buffer layer, sometimes referred to as zero-layer graphene, appears to be composed of a graphene like carbon lattice; however, interaction between its carbon atoms and the substrate silicon atoms modifies the layer's electronic properties. This bonding results in a 300meV bandgap at E_F rather than the π bands with linear dispersion relations as seen in freestanding graphene [61,62]. After the growth of the buffer layer, the first true graphene layer forms, showing the linear dispersion relation characteristic of isolated graphene. However, hydrogen intercalation can be used to passivate the SiC surface, turning the buffer layer into a quasi-free-standing graphene layer [62].

3.3 Confinement Controlled Sublimation

Epitaxial graphene growth through thermal decomposition of SiC differs from typical thin film growth techniques because the atoms for the epitaxial layer are provided by the substrate rather than an external source. During thin film growth through chemical vapor deposition (CVD), the rate of surface diffusion and the deposition flux can be controlled independently by adjusting the substrate temperature and adjusting the flow rate of the source material. During epitaxial graphene growth, both are tied to the substrate temperature because it affects the Si desorption rate, and therefore affects the

amount of carbon available for graphene formation. Growth in UHV conditions leads to rapid Si desorption at relatively low temperatures. The high Si sublimation rate and low temperatures results in defective graphene [26]. Increasing temperature can increase surface mobility and anneal out defects, but results in extremely rapid Si sublimation rates. Lower growth temperatures reduce the Si sublimation rate but also reduces surface mobility and results in more defects. Increasing the Si partial pressure can limit Si desorption, allowing for graphene growth near equilibrium conditions at higher temperatures [26].

One method to increase the Si partial pressure is confinement controlled sublimation (CCS) [26]. During CCS growth, the SiC wafer is confined in a small graphite crucible in high vacuum. The crucible is supplied with a small opening to moderate the outgassing of Si vapor from the crucible. This technique increases the Si partial pressure and results in a more controlled growth closer to equilibrium conditions [26]. Careful design and maintenance of the crucible in which the sublimation takes place is crucial for obtaining high quality epitaxial graphene growth with the CCS method.

The crucibles for epitaxial graphene growth consist of an enclosed graphite chamber with a small leak hole (~1mm diameter) to allow Si to escape at a controlled rate. The crucible dimensions vary, but for a typical 0.3x3.5x4.5mm^3 sample the internal volume of the crucible is approximately 100mm^3. In order to stabilize the conditions within the crucible, a few primer samples are baked prior to the first controlled graphitization run. This process allows some silicon to buildup on the inner walls of the crucible. As the crucible heats up, this silicon is released from the chamber walls

creating a silicon vapor pressure before surface sublimation begins on the SiC crystal resulting in a more uniform repeatable growth.

The sample chamber is heated under high vacuum conditions using an inductive heater. Early furnace designs utilized a metal susceptor, such as molybdenum, to heat the graphite crucible. However, in later designs the graphite crucible itself is used as the inductive heating element. This new simplified design provides a number of advantages. By directly heating the graphite, rather than relying on heat transfer from another element, we can more precisely control the heating process. The removal of the susceptor and surrounding insulation that was used also keeps the system cleaner and exposes the graphite chamber, allowing direct measurement of the chamber temperature with an infrared pyrometer. A Land Amtek IQR E Y Infinity infrared pyrometer was used for monitoring the temperature during growth. This pyrometer has a range of 700˚C to 1750˚C, making it well suited for measuring the temperature during the most important stages of graphitization. Monitoring the temperature with the infrared pyrometer has proven to be more precise than using a thermocouple, enabling much more consistent growth temperatures. The voltage response of the thermocouples drifted over time and they were very sensitive to oxidation and easily broken.

In addition to constant temperature monitoring using a thermocouple or infrared pyrometer, a Leeds and Northrup Co. 8622-C-8 optical pyrometer is sometimes used for temperature calibration. This pyrometer uses a disappearing filament design. The incoming radiation goes through a red filter and is compared to a filament that has an adjustable current flow. Matching the color of the filament to that of the incoming radiation from the target allows determination of the target temperature based on

knowledge of the filament's temperature to current relation. The 8622-C has three overlapping temperature ranges with a total range of 800˚C to 2800˚C

The typical graphene growth recipe is a 3-stage process. During the first stage, the chamber is heated for 10 to 20 minutes to allow the chamber to degas. This can be done at temperatures as low as 200˚C; however, in later furnace designs degassing is done at 800˚C due to the low temperature cutoff of the infrared pyrometer used for temperature measurements. The second stage is a 1200˚C anneal to remove the native oxide on the SiC surface. The final stage is the graphitization stage. The time and temperature vary greatly depending on the desired thickness and the facet selected for growth. C-face thin film growth is typically done at temperatures between 1450 and 1550˚C. Mono-layer coverage is typically obtained after approximately 10 minutes under such conditions [26].

3.4 High pressure growth

Graphene growth can be further inhibited by the introduction of an inert gas such as Argon or Neon. These gases slow the rate at which silicon gas escapes the confinement chamber by a factor $R = ({}^{D}/_{\lambda} + 1)^{-1}$ where λ is the mean free path of a silicon atom in the gaseous environment and D is the length of the path through the leak hole [26]. The reduced Si leak rate results in a higher Si-partial pressure inside the crucible. In addition, Si atoms that desorb from the surface have a finite probability of being reflected back to the surface off of an Argon atom [63]. The combination of these two factors greatly inhibits graphene formation.

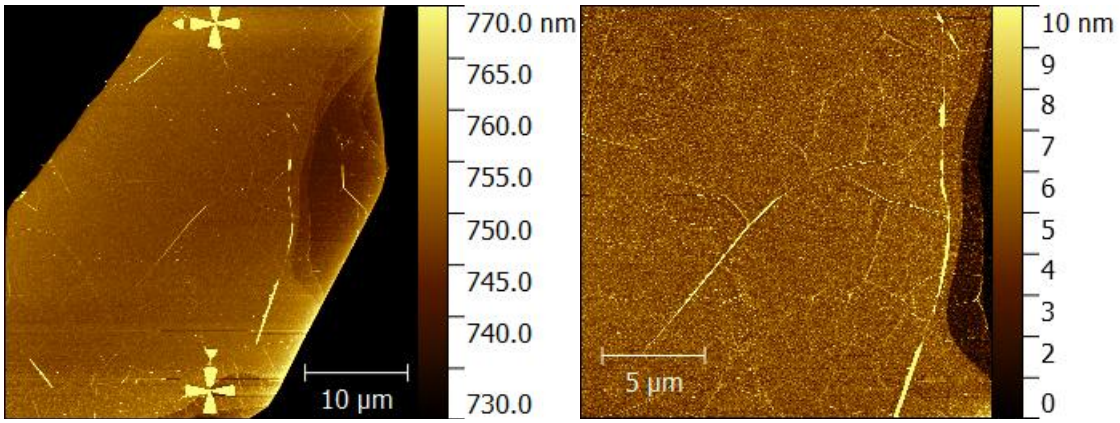

Figure 3.5: AFM images on top of a roughly 700nm tall mesa that formed on the C-face after CCS growth at 2090˚C in 1atm of Ar. The white lines are pleats that form in the graphene as a result of the different thermal expansion coefficients of graphene and SiC.

As expected, when CCS growth was performed in 1atm of argon graphene formation was strongly inhibited. In order to form graphene under these conditions samples were heated to over 2000˚C, which resulted in significant SiC surface restructuring. Figure 3.5 shows one such sample, 21H7, which was heated to 2090˚C for 40min in a CCS crucible with a 1mm diameter leak hole in 1atm of argon. This lead to the formation of mesas tens of microns wide and nearly one micron tall on the surface. Many of the mesas had large regions that were atomically flat as show in figure 3.5, while other mesas were shown to have spiraling hexagonal step structures on the surface. Surprisingly, Raman mapping of these samples showed that graphene grew preferentially on top of the mesas, with almost no graphene present on the lower surfaces (see figure 3.6). To confirm that there truly was no graphene on the lower surface the Raman laser was re-focused on the lower surface and additional measurements were taken.

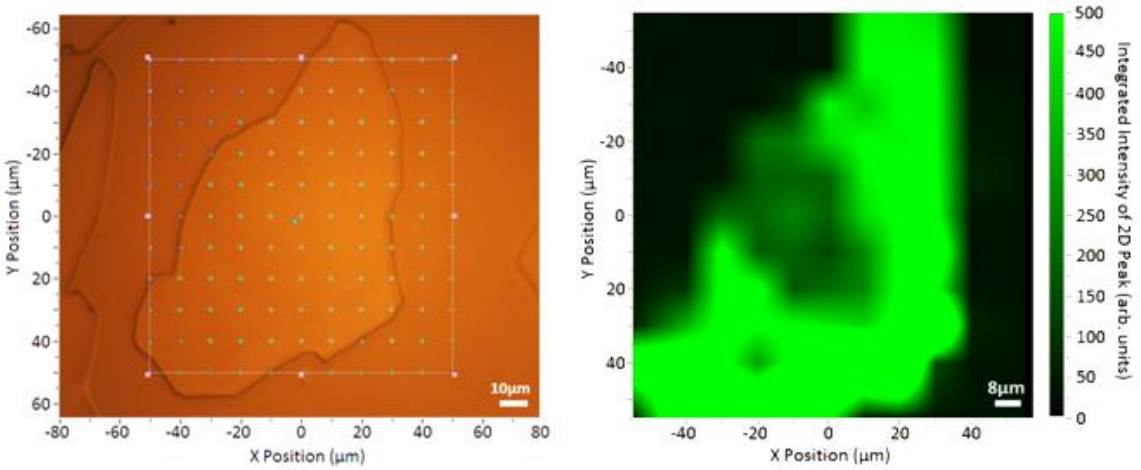

Figure 3.6: 121 point Raman mapping on a C-face mesa performed after CCS growth at 2090˚C. Left is an optical image of the mesa while the right side is a map of the integrated intensity of the 2D peak, which indicates the presence of graphene.

In order to measure the electronic properties of the atomically flat graphene formed on the mesas, Hall bars were patterned as shown in figure 3.7. Magnetoresistance measurements on these Hall bars at 4K revealed mobilities up to 1,400 $cm^2/V \cdot s$ at a charge density of $6.6x10^{12}cm^{-2}$. C-face graphene grown through CCS in vacuum have shown mobilities up to nearly $40{,}000cm^2/V \cdot s$ at low temperatures [60]. Thus, it appears that growth at elevated temperature and pressure does not necessarily improve the electronic properties of the graphene, despite providing a step free substrate. Although samples grown under these conditions did not show improved electronic properties, the suppression of graphene growth and the observed surface reconstruction of SiC may still be of use for certain applications where atomically flat surfaces are desired.

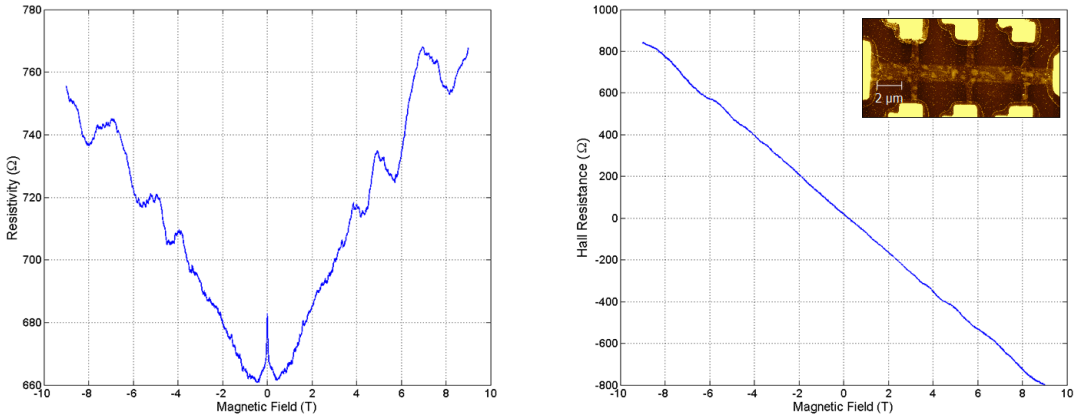

Figure 3.7: Left: Magnetoresistance data from an atomically flat Hall bar patterned on sample 21H7, Right: the corresponding hall resistance data. Inset: AFM image of the hall bar measured, the spots are believe to be PMMA residue left behind during lithography.

3.5 Silicon Carbide Pre-patterning

While high temperature growth leads to significant surface restructuring, the resulting surface structures were not well controlled. To better control SiC surface structures and steps, the SiC can be selectively etched using RIE prior to growth. Trenches and mesas etched onto the surface can strongly impact SiC step bunching. During graphene growth the SiC step edges migrate across the surface as the Si atoms sublimate, retaining the relatively uniform surface step distribution after growth. However, etching a large step parallel to the natural step direction blocks the flow of the natural steps, causing them to bunch up at the mesa edge. This process can be used to create large step free regions on the SiC surface.

An alternative use for SiC pre-patterning is to create preferred graphene nucleation sites. Steps etched into the Si-face can be used to form graphene nanoribbons along the step edges. This is possible because of the difference in growth rates on various SiC crystal facets. In order to make these sidewall graphene nanoribbons (GNR) a step is etched into the SiC (0001) face. The (0001) face is used because of its relatively

slow graphitization rate. During high temperature annealing this step edge facets to an angle of approximately 28˚. Graphitization then begins preferentially along these step edges. By carefully controlling the growth temperature and time, graphitization can be halted before the majority of the SiC (0001) face is graphitized. However, a buffer layer does form during this process. This process results in the formation of high mobility graphene nanoribbons with edges that terminate into the SiC substrate or into the insulating buffer layer. In addition, because the orientation of graphene on the Si-face is constant relative to the underlying SiC crystal directions, the chirality of the ribbons can be controlled by aligning the trenches along specified SiC crystal facets. Trenches etched parallel to $\{1\bar{1}00\}$ form armchair GNRs, while those etched parallel to $\{11\bar{2}0\}$ form zigzag GNRs. Sidewall GNRs nanoribbons have been found to have unique electronic and magnetic properties as will be presented in chapter 5. They provide a promising platform for the creation of high mobility graphene nano-electronics.

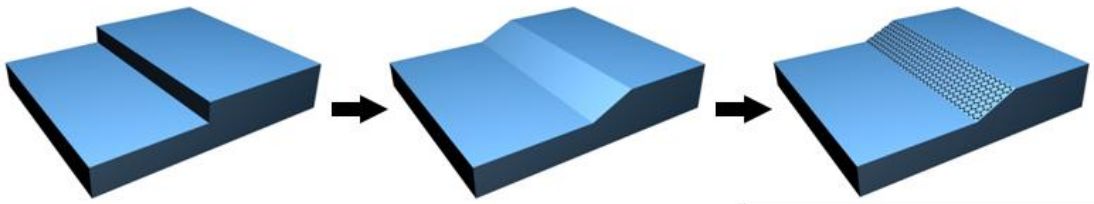

Figure 3.8: Process for creating sidewall GNRs. First a step is etched into the Si-face, then during high temperature annealing this step facets to a preferred crystal face, finally graphene grows preferentially on the sidewall facet forming a GNR. [64]

CHAPTER 4

GRAPHENE SPINTRONICS

4.1 Spintronics

In basic electronic devices, information is stored and processed through electron charge. Signals can be transmitted through voltage pulses and data can be stored in capacitors. Spintronics goes beyond this and utilizes electron spin in order to transmit, store, and manipulate data [65]. In such devices, magnetic fields are typically used to manipulate and detect the electron spin state. The principles of spintronics are already employed in devices such as hard drives and magnetic random access memory (MRAM) [65]. The discovery and characterization of materials that can manipulate and transmit spin information will lay the foundation for the next generation of spintronic devices.

While ordinary magnetoresistance was observed as early as 1856 by William Thomson [66], it was not until 1988 that giant magnetoresistance (GMR) was experimentally demonstrated through the independent experiments of Grunberg and Fert in Fe/Cr multilayers [67,68]. In a Fe/Cr multilayer system with Cr layers less than 30Å thick, the adjacent Fe layers exhibit in plane magnetization with antiferromagnetic (AF) coupling between adjacent layers [67]. The application of an external field overcomes this AF coupling and aligns the magnetizations of the Fe layers parallel to one another. As the magnetizations of the layers became aligned it was observed that the resistance through the Fe/Cr stack was reduced by a nearly factor of 2 (fig 4.1). The experimental results showed that the resistance stabilizes at high fields once the magnetization in the Fe layers becomes saturated. This initial observation of magnetization dependent

transmission was not only of interest from a pure physics standpoint, but has also triggered many practical applications in modern electronics [65].

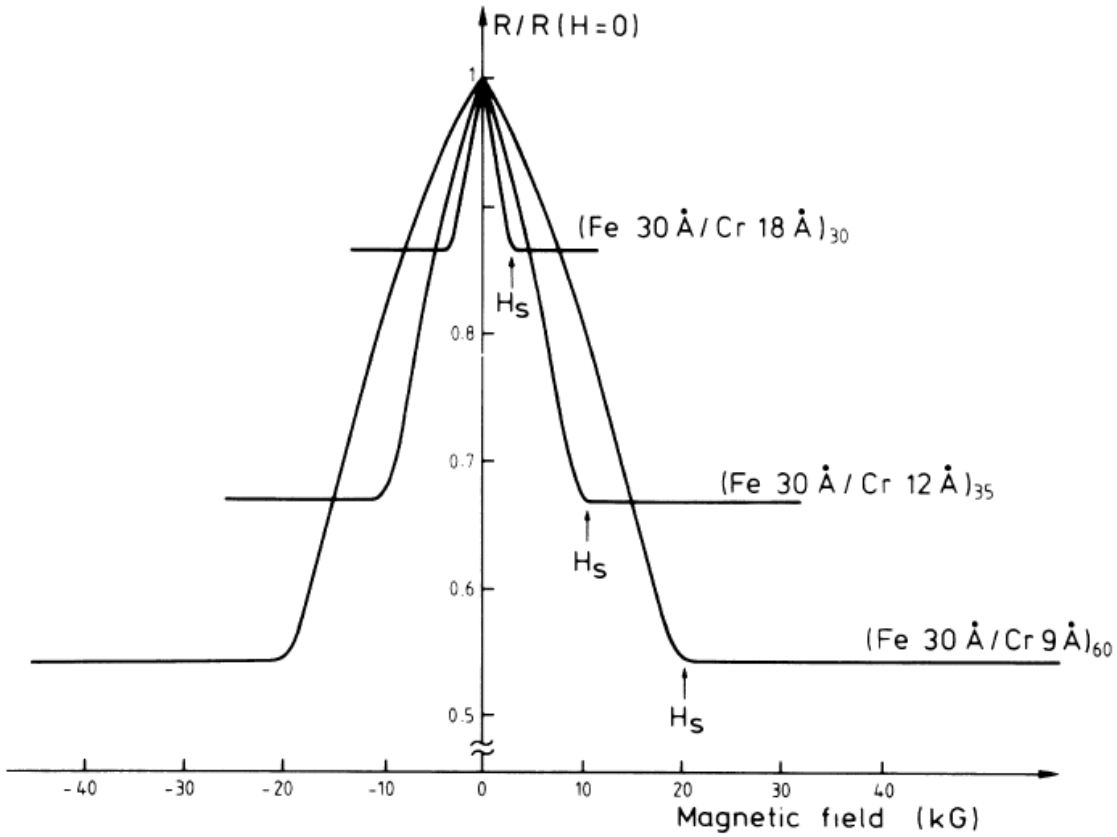

Figure 4.1: Magnetization dependent resistance of Fe/Cr multilayer films as measured by Fert in 1988 showing the fractional change in resistance measure through Fe/Cr multilayer films as a function of applied magnetic field. R(H=0) is the resistance at zero external field and H_s is the saturation field of the Fe layers [67].

The changed in resistance in the Fe/Cr multilayer system is a consequence of magnetic ordering in iron. In ferromagnets, like iron, there is an interaction between the spin states on neighboring lattice sites. This exchange interaction can be simply described by the Heisenberg model, which has the following Hamiltonian:

$$H = \frac{1}{2}\sum_{\substack{i,j \\ i \neq j}} J_{ij}\, \boldsymbol{S}_i \cdot \boldsymbol{S}_j \tag{4.1}$$

In this Hamiltonian i and j refer to lattice sites, $\boldsymbol{S}_i$ and $\boldsymbol{S}_j$ are the spin operators of the lattice sites, and J_{ij} are exchange constants. When $J < 0$ the interaction energy favors parallel alignment, the ferromagnetic case, and when $J > 0$ the interaction energy favors anti-parallel alignment, the antiferromagnetic case. This leads to local magnetic order and a spin-splitting of the energy bands in ferromagnets. The magnetic order is lost above the Curie temperature.

While the exchange interaction causes spins to align locally, this alone simply results in small domains with aligned spins [69]. Typically these domains are randomly oriented relative to each other resulting in no bulk magnetization. In order to uniformly magnetize the bulk ferromagnet in a specific direction, an external magnetic field can be applied, which aligns the domains (and hence the magnetization) along the direction of the applied field. The field strength required to create this alignment is known as the critical field (H_c in figure 4.2). Further increasing the magnetic field can further increase the magnetization to a point. Eventually a maximum magnetization is reached at the saturation field (H_s in figure 4.2). Due to hysteresis, the ferromagnet will retain its magnetization when the field is removed unless heated or otherwise given sufficient energy to randomize the domains. Applying the field in a different direction can re-align the magnetization once the critical field is reached. The value of the critical field for small ferromagnets is influenced by the geometry of the ferromagnet, due to shape anisotropy [70]. The shape anisotropy effect, where magnetization typically prefers to be along a long axis of the sample, is advantageously used in spintronics. In spin transport measurements, thin (~20nm) narrow (<1μm) contacts with a length to width ratio over 5

are typically used. This gives the contact a uniaxial magnetization axis, with bistable states parallel to the long axis as shown in fig 4.2 [71].

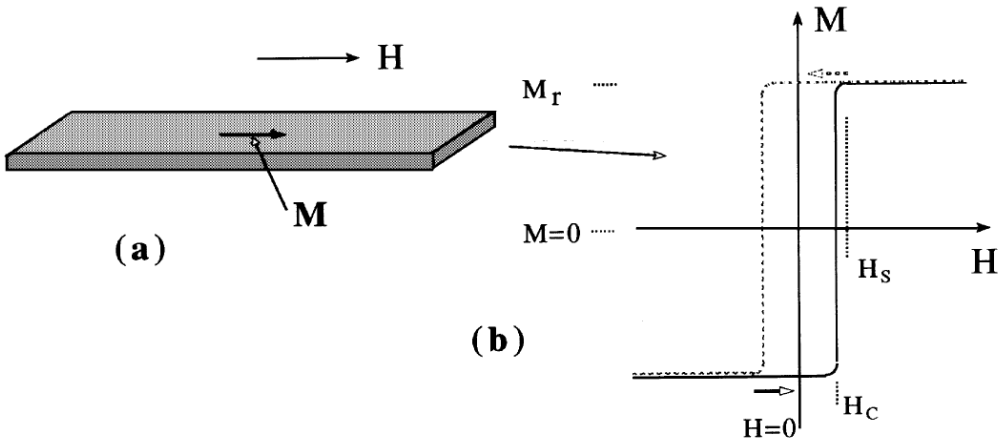

Figure 4.2: (a) Magnetization axis in a typical ferromagnetic contact showing the magnetic easy axis parallel to the long axis of the ferromagnet. (b) Relationship between magnetization and applied field showing the hysteresis loop of the magnetization as the applied field is swept. H_C and are the critical field and saturation field of the ferromagnet. From ref [71]

4.2 Giant Magnetoresistance

Giant Magnetoresistance is caused by spin-dependent scattering in the ferromagnetic layers. In 3d ferromagnets like Fe, Co, and Ni, the s and p bands form a dispersive sp band that dominates conduction, while the d band is localized with a high density of states and low carrier velocity [72]. The scattering probabilities for spin up and spin down carriers are independent and are proportional to the density of states of their respective carrier type at the Fermi level [72]. The exchange interaction causes a spin-split d band, resulting in different populations of spin-up and spin-down electrons at the Fermi level. The imbalance of spin-up and spin-down states in the d band results in different scattering probabilities for each and thus two different conductivities: $\sigma_\uparrow$ and $\sigma_\downarrow$ [73].

According to the Mott model [74], the electrical conductivity in metals can be described as the sum of two nearly independent conduction channels, corresponding to spin up and spin down electrons [72].

$$\sigma = \sigma_{\uparrow} + \sigma_{\downarrow} \tag{4.2}$$

Applying this simple concept to the situation of current perpendicular to the plane of a ferromagnet-nonmagnet-ferromagnet stack allows for clear understanding of the change in resistance caused by the change in relative magnetization. In figure 4.3, the electrons experience a low resistance when their spins are aligned anti-parallel to the magnetization of the cobalt layer ($R_{\downarrow\uparrow}$) and a high resistance when aligned parallel to the cobalt magnetization ($R_{\uparrow\uparrow}$). In the case of parallel alignment of the two ferromagnets, electrons with spins aligned in one direction experience low resistance through both ferromagnetic layers, while electrons with spins aligned in the opposite direction experience high resistance through both. If spin up and spin down carriers are treated as parallel conduction paths the total resistance is [72]

$$R_P = \left(\frac{1}{R_{\downarrow\uparrow} + R_{\downarrow\uparrow}} + \frac{1}{R_{\uparrow\uparrow} + R_{\uparrow\uparrow}}\right)^{-1} = \left(\frac{2R_{\downarrow\uparrow}R_{\uparrow\uparrow}}{R_{\downarrow\uparrow} + R_{\uparrow\uparrow}}\right) \tag{4.3}$$

In the case of anti-parallel alignment, both spin up electrons and spin down electrons experience high resistance through one layer and low resistance in the other. In this case the total resistance is

$$R_{AP} = \left(\frac{1}{R_{\downarrow\uparrow} + R_{\uparrow\uparrow}} + \frac{1}{R_{\downarrow\uparrow} + R_{\uparrow\uparrow}}\right)^{-1} = \left(\frac{R_{\downarrow\uparrow} + R_{\uparrow\uparrow}}{2}\right) \tag{4.4}$$

Combining these two equations yields the fractional change in resistance:

$$\frac{\Delta R}{R_P} = \frac{R_{AP} - R_P}{R_P} = \left(\frac{(R_{\uparrow\uparrow} - R_{\downarrow\uparrow})^2}{4R_{\downarrow\uparrow}R_{\uparrow\uparrow}}\right) \tag{4.5}$$

d

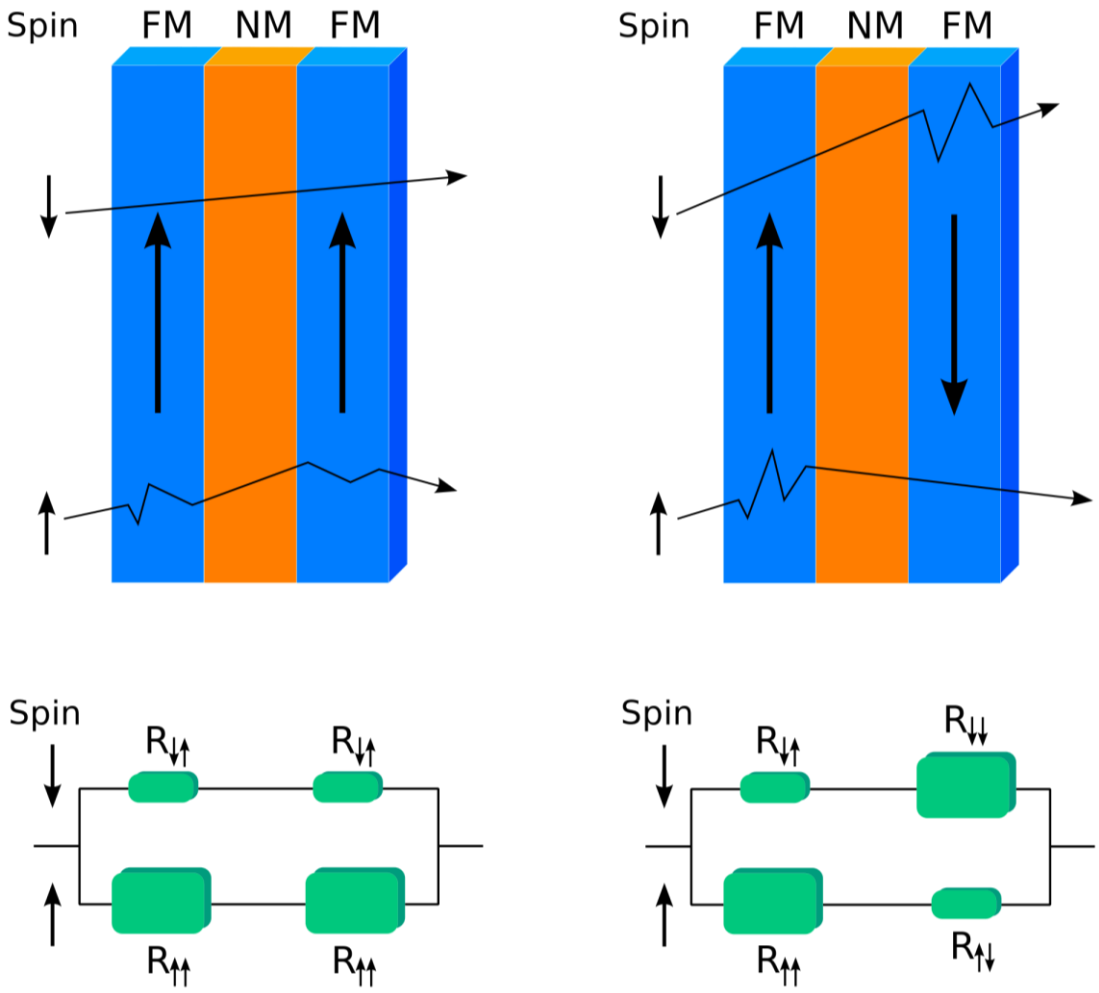

Figure 4.3: Two ferromagnetic layers separated by a thin non-magnetic metal spacer layer. In the parallel case the spin-down electrons have a high transmission probability and dominate transport, while in the anti-parallel case both spin up and spin down electrons experience increased scattering in one of the two layers, increasing the total resistance. Image from Wikimedia Commons/Guillaume Paumier

4.3 Tunnel Magnetoresistance

One alternative to the non-magnetic metal spacer is a thin (1-2nm) insulating layer to form a device known as a magnetic tunnel junction (MTJ). The tunnel barrier is typically made of Al_2O_3 or MgO [75], and gives the device a much higher resistance than is found in the ferromagnetic/non-magnetic metal stacks. As in the case of giant magnetoresistance, the resistance of a MTJ depends on the relative magnetizations of the

ferromagnetic layers. The high resistance of MTJs is preferable for many nanoelectronic applications, such as MRAM[75].

The first studies on tunnel junctions were performed by Bardeen in 1961[76]. Bardeen described tunneling by considering two independent wave functions separated by an infinite barrier. He then used time dependent perturbation theory to describe the probability of tunneling from one state to the other. Using this approach the current through the barrier from the left electrode to the right electrode can be written:

$$I(V) = \int_{-\infty}^{\infty} N_L(E) N_R(E + eV) |M(E,V)|^2 f(E)\big(1 - f(E + eV)\big) dE \qquad (4.6)$$

In equation 4.6 $N_{L,R}(E)$ is the density of states at the energy E of the left or right electrode, $f(E)$ is the Fermi-Dirac distribution, and $M(E,V)$ is the tunnel transfer matrix.

In 1975, Julliere expanded on Bardeen's description to explain spin dependent tunneling [77]. Julliere's model was based on two primary hypotheses. The first is that the tunnel conduction is performed by two independent spin channels and that spin is conserved during tunneling. The second is that the probability of transmission through the barrier is independent of spin. Based on these assumptions a simplified expression for the conductance through the junction can be formulated:

$$G \propto \sum_s N_{Ls}(E_F) N_{Rs}(E_F) \qquad (4.7)$$

Here *s* represents the different spin states and $N_{L,Rs}(E_F)$ is the density of states in the left (right) electrode with spin s. Labeling the majority spin band as ↑ and the minority spin band as ↓ allows the conductance in the parallel and anti-parallel states to be written as:

$$G_P \propto N_{L\uparrow}(E_F) N_{R\uparrow}(E_F) + N_{L\downarrow}(E_F) N_{R\downarrow}(E_F) \qquad (4.8)$$

$$G_{AP} \propto N_{L\uparrow}(E_F) N_{R\downarrow}(E_F) + N_{L\downarrow}(E_F) N_{R\uparrow}(E_F) \qquad (4.9)$$

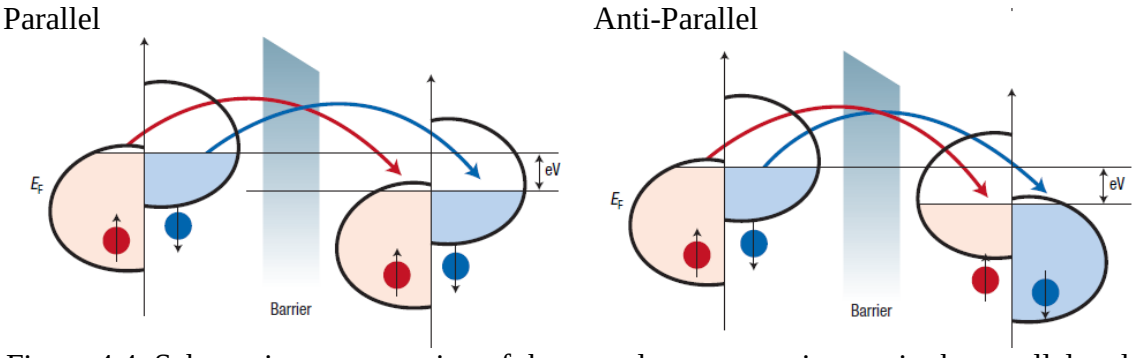

Figure 4.4: Schematic representation of the tunnel magnetoresistance in the parallel and anti-parallel configuration. The spin-split d band results in different DOS at the Fermi level for spin up and spin down electrons. Spin is conserved during tunneling and electrons can only tunnel into a matching spin state. In the parallel configuration electrons can more easily find free states to tunnel to [75].

The spin polarization of the conduction electrons is defined in terms of relative densities of states at the Fermi level of the majority and minority spin carriers, as shown in equation 4.10 [78].

$$P = \frac{N_\uparrow - N_\downarrow}{N_\uparrow + N_\downarrow} \tag{4.10}$$

Using the conductance relations for the parallel and anti-parallel configurations given in equations 4.8 and 4.9, the percent change in magnetoresistance, known as tunnel magnetoresistance (TMR), can be calculated as a function of the spin polarizations of the two ferromagnets:

$$TMR = \frac{R_{AP} - R_P}{R_p} = \frac{2P_1P_2}{1 - P_1P_2} \tag{4.11}$$

TMR is typically defined as the change in resistance relative to the parallel resistance, R_P, while a very similar quantity, called junction magnetoresistance (JMR), is defined as the change in resistance relative to the anti-parallel resistance, R_{AP}. Typically the parallel state has the lower resistance of the two, although there are systems where negative TMR has been observed [79]. Julliere made the first measurements of a MTJ in 1975 [77], but

it was not until 1995 that high magnetoresistance (up to 30% at 4.2K) MTJs were successfully demonstrated [80,81] thanks to improvements in thin film deposition.

4.4 Spin Injection Into Non-magnetic Conductors

In addition to devices made of ferromagnets with thin metallic or insulating separators, there is also great interest in injecting spin current into non-magnetic conductors and semi-conductors [82]. This would allow spintronic devices with complex device architectures, as well as further integration of spintronics with modern complementary metal–oxide–semiconductor (CMOS) electronics [83]. Much of the prior work using graphene as a spintronic material has focused its use as a non-magnetic channel for transmitting spin information. When doing spin injection, two of the most important properties to consider are the efficiency of the spin injection and the spin diffusion length inside the non-magnetic channel.

Figure 4.5 shows some of the relevant transport physics at the ferromagnet to nonmagnet interface. The spin-polarized current injected from the ferromagnet generates a non-equilibrium magnetization of the charge carriers at the interface due to spin accumulation. Spin diffusion results in an exponential decay of the spin population away from the interface with characteristic spin diffusion lengths $l_{sf,F}$ in the ferromagnet and $l_{sf,N}$ in the non-magnetic material. This decay can be seen in the magnetization potential H*, defined as the carrier magnetization over the susceptibility. The discontinuity in H* at the interface is due to the different magnetic susceptibilities of the two materials. As the figure shows, spin diffusion occurs into the ferromagnetic source as well as the non-magnetic channel. This backward spin current effectively cancels some of the incoming spin current, reducing the fractional spin polarization of the injected current as seen in

figure 4.5 (c) [71]. To combat this effect a tunnel barrier can be used to increase the interface resistance and inhibit spin diffusion back into the contact.

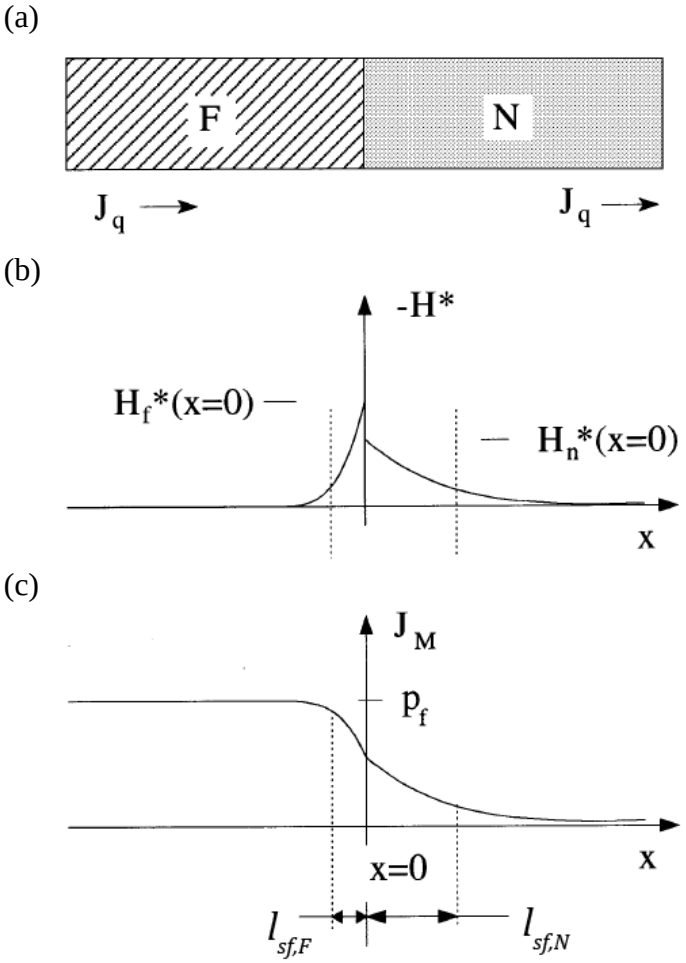

Figure 4.5: Model of charge and spin transport across a ferromagnet-nonmagnet interface (a) Schematic of the ferromagnet to non-magnetic metal interface, J_q is the charge current. (b) Magnetization potential H*, P_f is the spin polarization of the charge carriers in the ferromagnet (c) fractional spin polarization of the current J_M. From ref [71]

4.5 Graphene Spin Transport

Graphene has been investigated as a promising material for spin transport thanks to its low spin orbit coupling and high mobility [83]. The first spin transport measurement on graphene was made using a lateral spin valve consisting of two NiFe contacts ~200nm apart connected with a 200nm wide exfoliated graphene ribbon [84].

This relatively simple structure exhibited room temperature TMR up to 10%, successfully demonstrating that graphene could be used as a non-magnetic conductor for spin transport[84]. Since then, the spin transport properties of various forms of graphene have been studied, including both SLG and MLG exfoliated graphene ribbons on SiO_2 substrates [85-88], exfoliated graphene on hexagonal Boron Nitride[89], suspended graphene ribbons[90], and both C-face and Si-face epitaxial graphene on SiC [52,83,91].

In addition to the standard two terminal "local" spin valve, many experiments also employ a 4-point configuration for non-local spin current measurements. In the non-local arrangement, current is injected through one pair of contacts, while the voltage is measured using an adjacent set of contacts as shown in figure 4.6 (b). The non-local resistance is defined as the non-local voltage divided by the injected current. Spin accumulation under the current injection contact creates a magnetization potential that decays exponentially along the ribbon as discussed in chapter 4.1. This results in a pure spin current on one side of the injection contact without any accompanying charge current. Ferromagnetic detection contacts selectively measure the potential of the spin up or spin down channel depending on their own magnetic orientation (the selectivity is not 100% and depends on the polarization of the detection contacts). Figure 4.6 (c) shows the dependence of the non-local resistance on the magnetization directions of four Co contacts patterned on an exfoliated graphene ribbon [86]. While only the inner contacts (2 and 3) need to be ferromagnetic, often all four contacts are made of the same ferromagnetic material. The coercive field strength of the contacts can be tuned by adjusting their widths, allowing independent switching of the contacts' magnetization directions.

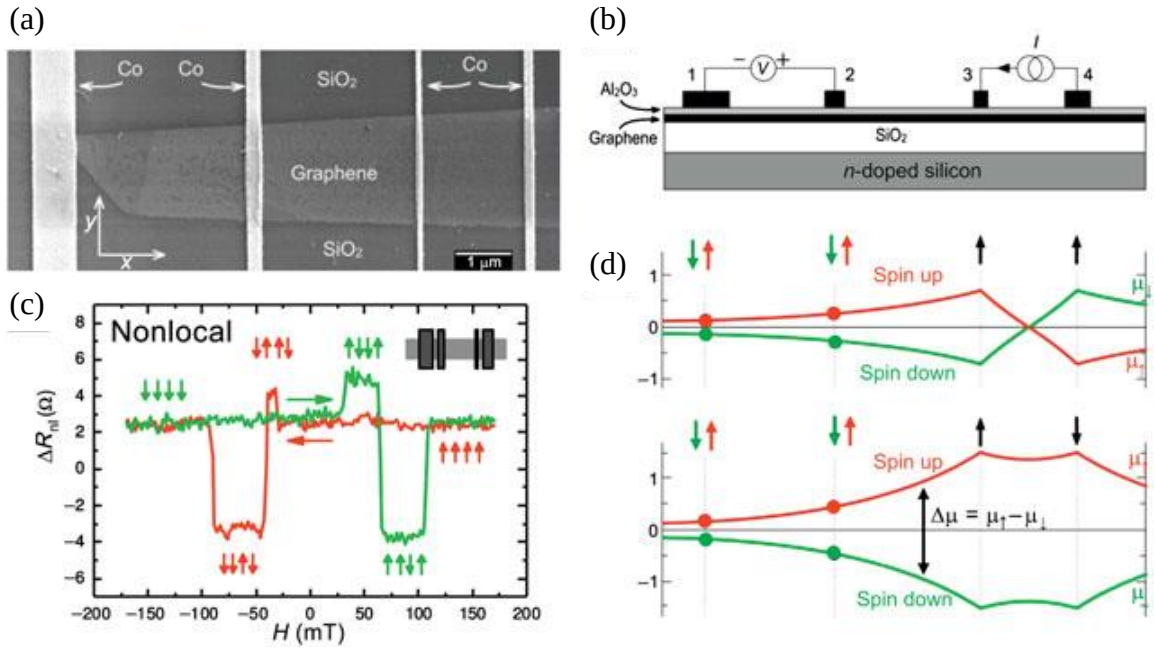

Figure 4.6:(a) SEM image of a 4-terminal spin valve on an exfoliated graphene ribbon (b) device schematic (c) non-local resistance as a function of applied field (d) schematic representation of the spin dependent chemical potential for the spin up (red) and spin down (green) channels. From ref [83,86]

In order to calculate the spin diffusion length and spin lifetime of a sample, a Hanle spin precession measurement can be carried out [83,86]. In such a measurement, the Co contacts are first polarized in a parallel or anti-parallel configuration. A magnetic field is then applied perpendicular to the plane of the graphene ribbon and Co contacts and the non-local resistance is measured as a function of this applied field. The magnetic moments of the electrons precess around the out of plane magnetic field with a Larmor frequency of $\omega_L = g\mu_B B/\hbar$, where g is the effective Lande factor (~2) and μ_B is the Bohr magneton. With the proper applied field, the magnetic moment can rotate 180˚ as it travels from the injector to the detector as illustrated in figure 4.7 (a), causing detection of now parallel magnetic moments from an anti-parallel injector or vice versa. The magnetic field also causes some dephasing of the spins in the channel, dampening the signal. The combined results of the spin precession and decay are observed as an

oscillating decay of the non-local resistance as seen in the results of Han et al. in figure 4.7 (b-c) [92]. The Hanle spin precession data can be fit with solutions of Bloch equations [83,86] to determine the diffusion constant D, the spin lifetime τ_{sf}, and the spin diffusion length l_{sf}. The results of Han et al. (figure 4.7 b-c) highlight the importance of resistive tunnel contacts. Measurements with transparent contacts gave a spin lifetime of only 84ps, while measurements using resistive tunnel barriers found a spin lifetime of 448ps [92]. This discrepancy can be attributed to spin escape into the ferromagnetic injection contact when transparent contacts are used [83].

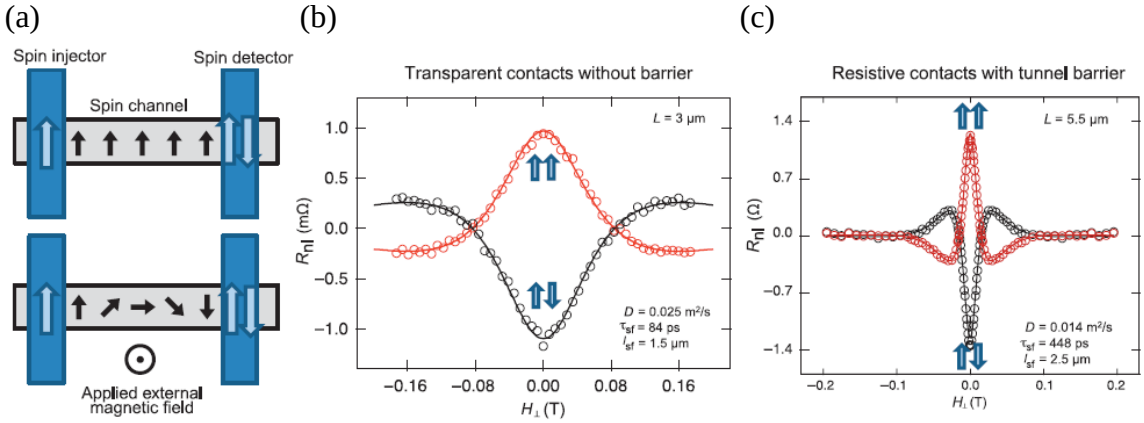

Figure 4.7: (a) With no external field the spin direction of the injected current is conserved, but when a perpendicular magnetic field is applied the magnetic moment rotates during travel. (b) Hanle measurement on exfoliated graphene with transparent contacts, and (c) Hanle measurement on exfoliated graphene done with tunnel contacts.

The Fert group further explored the importance of barrier resistance on spin transport through graphene in their experiments on C-face multilayer epitaxial graphene (MEG) [91]. In this experiment, two terminal devices consisting of Co contacts with Al_2O_3 tunnel barriers were patterned onto MEG ribbons. The tunnel resistance for these devices ranged from 1MΩ to 100MΩ, allowing efficient spin injection into the graphene, with minimal spin escape into the contacts. In one device, with a 0.8μm long channel, the measured magnetoresistance was 9.4%. A perfect channel would result in half of the

MR of a $Co/Al_2O_3/Co$ MTJ, which is 25%. Hence the 9.4% measured MR is 75% of the 12.5% MR that would be predicted for a perfect channel, demonstrating minimal degradation of spin information in the graphene channel. Spin diffusion lengths in the devices measured ranged between 95µm and 285µm, the longest spin diffusion lengths measured in any graphene system.

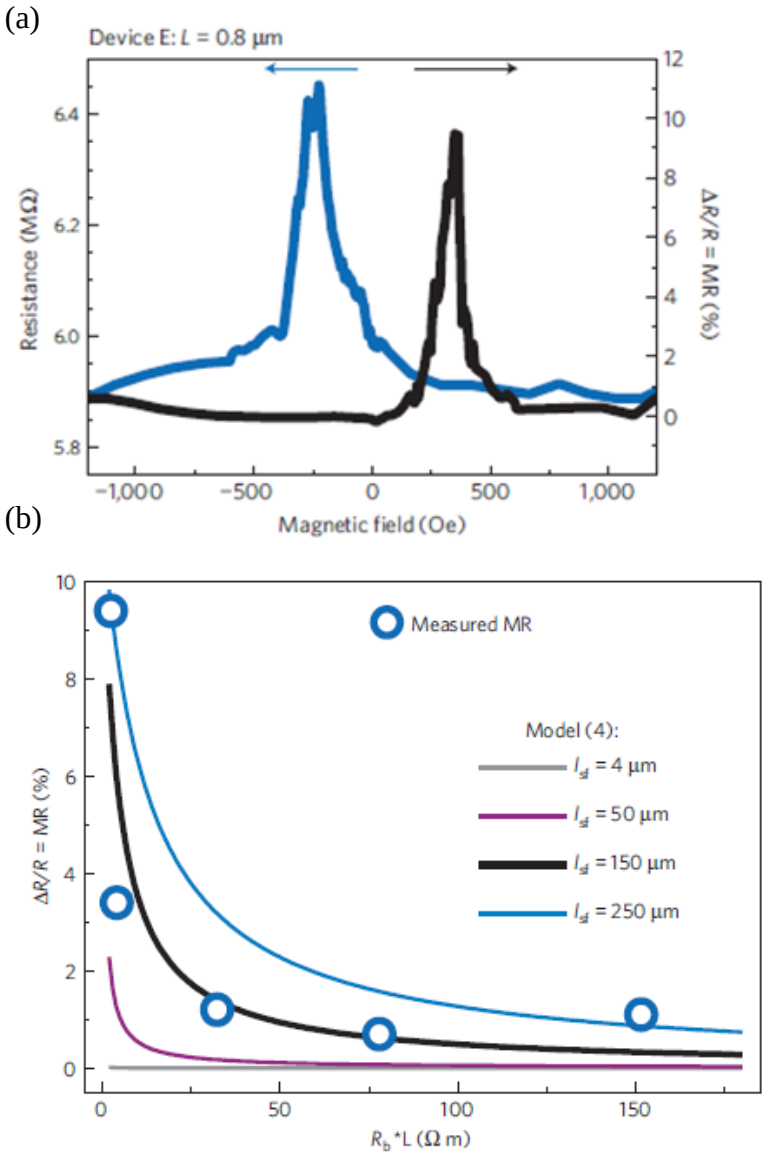

Figure 4.8: (a) 2-point magnetoresistance with Co/Al_2O_3 contacts on C-face MEG, showing 9.4% MR. (b) Results obtained with different barrier resistances and a plot of the model showing the expected behavior for different spin diffusion lengths. From ref [91]

4.6 Magnetism in Graphene

While pure graphene sheets are non-magnetic and act as good spin channels, there is great interest in creating magnetic forms of graphene for use in spintronics. There are a number of methods proposed for inducing magnetism in graphene. Many graphene nanostructures are also predicted to have shape dependent magnetic properties and have been proposed for possible applications as spin logic devices [93,94]. Graphene nanoribbons with zigzag edge terminations are predicted to have spin polarized edge states [95-97]. Magnetism can also be induced through lattice defects, vacancies, and adsorbates [98-100].

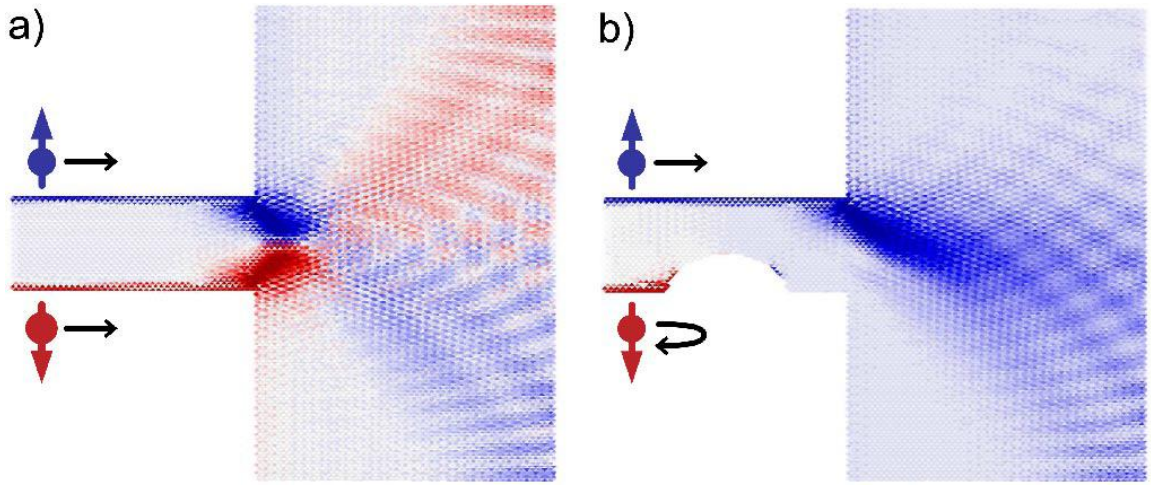

Figure 4.9: (a) An ideal zigzag GNR with opposite spin alignments on its edges. The total current injected into the non-magnetic graphene sheet is equal parts spin up and spin down. (b) A defect introduced on the lower edge scatters the edge current resulting in a net injection of spin up current into the non-magnetic graphene. From ref [101].

Graphene nanoribbons are of particular interest because of the unique properties predicted by theoretical calculations. GNRs with zigzag edges are predicted to have spin polarized edge states that exhibit anti-ferromagnetic coupling between each other [95-97,102]. This leads to locally spin polarized current on the edge but no spin polarization of the total current. However, there are situations under which a net spin current can

theoretically be injected from a GNR. For example, Wimmer et al. predicts that a GNR with one pristine edge and one defective edge could be used to inject spin polarized current as shown in figure 4.9 [101]. In addition, Son et al. predicts that transverse electric fields could be used to shift the energy bands on opposite edges, resulting in parallel alignment of the spins on both edges [95]. Superlattices of graphene and graphane with zigzag interfaces have also been proposed as a potential method to generate spin polarized current in graphene [103-106].

In addition to edge state magnetism, there have been efforts to magnetize the bulk graphene lattice through defects or chemical functionalization. Theoretical work by Yazyev et al. predicts that magnetic moments will form around lattice defects and hydrogen chemisorption sites due to ferromagnetic coupling between the electrons at the three neighboring lattice sites [98]. Defects on the same sublattice couple ferromagnetically, while defects on different sublattices couple anti-ferromagnetically[98]. Thus, the spin polarization of random defects will tend to cancel out in the bulk, but if one sublattice was selectively bonded, a net spin polarization could be obtained. Experimental work by the Haddon group has demonstrated local magnetic polarization in graphene sheets induced by nitrophenyl functionalization [99,100], supporting theoretical predictions and providing a possible path toward controlling the magnetic properties of graphene. Magnetism has also been predicted for epitaxial graphene buffer layers due to periodic bonding to the SiC substrate or adatoms [107].

At this time, there is insufficient information to deduce the mechanism behind the observed the spin dependent conductance observed in epitaxial graphene nanoribbons. However, these mechanisms show that magnetism in graphene is not entirely unexpected.

Hopefully, the careful documentation of the effects observed here, along with future measurements on epitaxial graphene nanoribbons, will provide better understanding of the underlying physics at work.

CHAPTER 5

EPITAXIAL GRAPHENE NANORIBBON TRANSPORT

While growing large graphene sheets on the SiC (0001) and (000-1) faces is useful for many applications, lithographic patterning leads to very rough edges that cause scattering and limit edge conduction[108]. This is unfortunate because interesting physical properties have long been predicted for GNRs with perfect zigzag-edges, including ferromagnetism [95] and ballistic transport [109]. In order to create ribbons with clean edge terminations (although not perfectly zigzag), the selective growth technique discussed in chapter 3.5 is used to form sidewall GNRs along SiC $(10\bar{1}n)$ and $(11\bar{2}n)$ crystal facets. They are labeled armchair and zigzag ribbons respectively, based on the orientation of Si-face graphene. However, their true edge orientations may not be so straightforward. The results presented in this work were all measured on ribbons grown along the armchair direction. Transport measurements of these ribbons [110] have shown them to have unique electronic and magnetic properties that could prove useful in the creation of future electronic and spintronic devices as explained in detail below. In particular the work of Baringhaus et al. shows single channel ballistic transport indicating that both the spin and valley degeneracies are lifted in these ribbons [110].

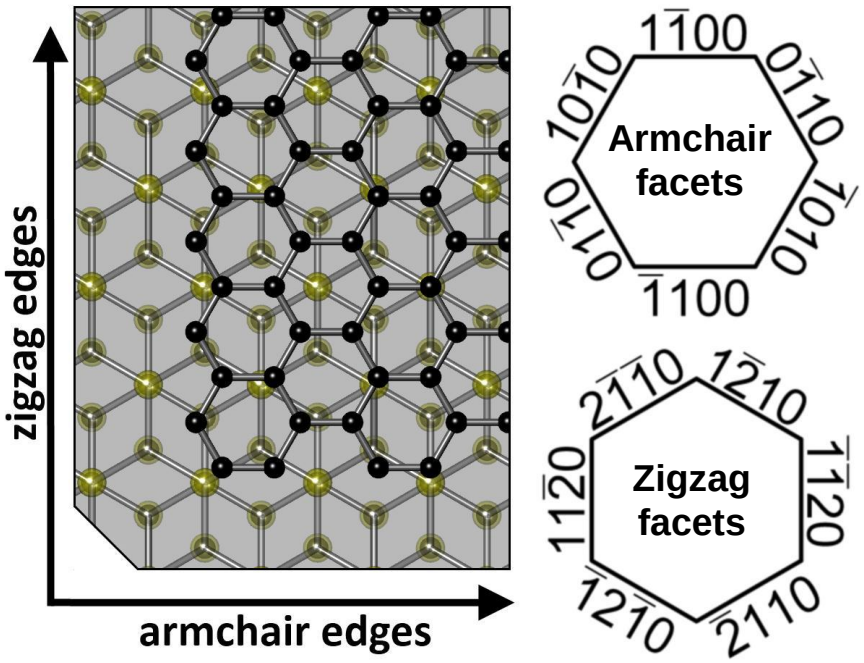

Figure 5.1: Armchair and zigzag ribbons are labeled based on the SiC crystal facet

5.1 Magnetic Tunnel Junction Measurements

In order to probe the electronic and magnetic properties of these sidewall GNRs, metallic contacts were patterned on the ribbons. Initially, devices with multiple cobalt tunneling contacts were created in order to measure the spin diffusion length in the GNRs, as discussed in Chapter 4.5. However, the results were anomalous. Specifically, in several measurements there was a difference in resistance when all of the Co contacts were magnetized up compared to when they were all magnetized down. From a simple symmetry argument, one would expect these two configurations to result in identical resistances. The difference indicated that the graphene ribbons were intrinsically magnetically polarized. In order to test this hypothesis, devices with a single Co tunneling contact in between non-magnetic Pd/Au contacts were created.

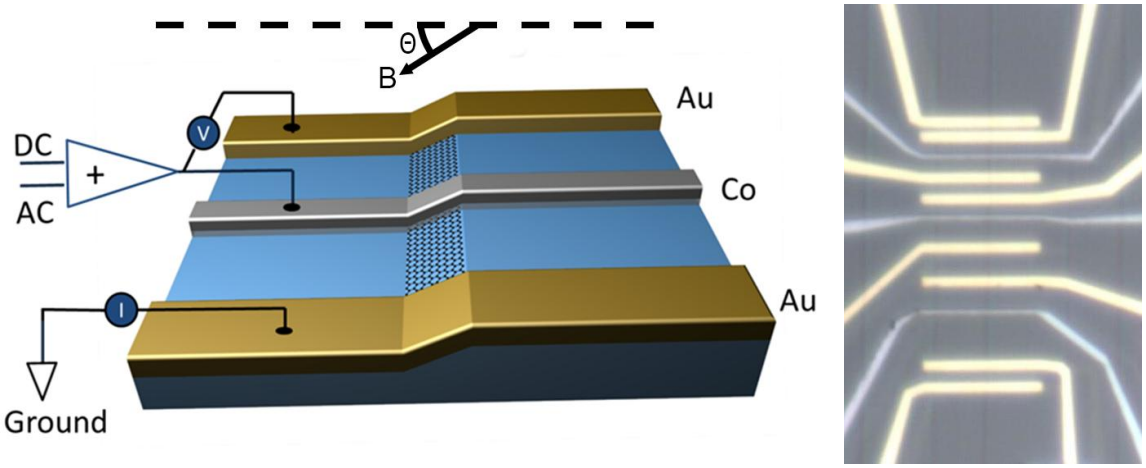

Figure 5.2: Left: Schematic of 3-terminal tunnel magnetoresistance measurement. Sample can be rotated relative to external magnetic field. Field angle is measured relative to Si (0001) face. At 0˚ the positive field direction is from the high side of the trench wall toward the low side as indicated. Right: optical image of a sidewall MTJ.

A magnetic tunnel junction consists of two ferromagnets separated by a thin insulating layer. In this experiment, Co serves as one magnetic contact, while the GNR itself serves as the other. A thin aluminum oxide tunnel barrier, approximately 1nm thick, separates the graphene and Co. To allow for control over the cobalt's spin polarization direction, it is locally patterned into a long thin rod: 10μm long, 300nm wide, and 40nm thick. This shape anisotropy gives the cobalt a magnetic easy axis, as discussed in chapter 4, along which the spin polarization can be controlled using an external field. The coercive field strengths for the Co contacts were between 20mT and 100mT depending on the device. During spin switch measurements, the magnetic field was typically aligned along the Co long axis in the (0001) plane (θ=0). Nearby Pd/Au contacts allow for 2 and 3-point measurements of the tunnel resistance, as well as other electronic transport measurements on the ribbon.

Resistance measurements were made using a lock-in amplifier providing either constant current or voltage depending on the measurement. For low resistance measurements, a large series resistor (1MΩ to 1GΩ) is placed on the voltage output of the

lock-in amplifier, providing a relatively constant current as long as the device resistance is much smaller than the series resistor. However, this method is not well suited for measuring resistances over 1MΩ because they approach the input impedance of the SR830, which is 10MΩ. For these measurements, an AC voltage is applied to the sample and a current amplifier is used to measure the AC current through the device. The voltage can be measured in parallel or measured at another contact in a 3-point configuration as shown in figure 5.2. Because the focus of these measurements is the tunnel resistance, the 3-point configuration was used whenever possible since it does not include additional resistance from the ribbon and drain contact. However, very little difference was observed between 2-point and 3-point resistance measurements as the tunnel resistance is typically much larger than the ribbon resistance. For voltages less than 10mV a voltage divider is placed on the output to provide a clean low voltage signal.

To calculate TMR in this work the difference in resistance at B=0T is used. Rather than using a single point at B=0T the values of R for $|B| < 10mT$ are averaged to minimize the effects of noise. The standard TMR equation (4.11) will yield positive values whenever $R_{AP} > R_P$. However, in this work a slightly different definition of TMR is used (equation 5.1) so that the sign reflects the magnetic field direction of the high resistance state. The resistance values near B=0T during the up sweep, $R(B_0^-)$, are subtracted from those near B=0T during the down sweep, $R(B_0^+)$, and this difference is divided by the smaller of the two values, since the smaller value is R_P in most systems. Negative TMR values in this work indicate that the field direction for the high and low resistance states has flipped. As the true spin polarization direction in the graphene is unknown, it cannot be determined if this is true negative TMR or if the spin polarization

of the graphene has changed direction. The magnitude will be the same as would be found using the standard TMR equation, if R_P is in fact the low resistance state.

$$TMR = \frac{R(B_0^+) - R(B_0^-)}{R_{min}} \tag{5.1}$$

5.2 Sample 31JH6

One of the first samples to show a TMR signal was with a sidewall ribbon sample 31JH6. From the orientation with respect to the SiC lattice this ribbon was determined to be a armchair ribbon (see Fig 5.1). The ribbon was grown using a fixed power recipe (see below) in a graphite crucible with a 0.4mm diameter leak hole. It was grown following a C-face multi-layer sample grown at ~1565˚C for 45 min, which likely left the inner crucible walls Si-rich due to the significant sublimation of Si during the growth. A 3-stage growth recipe was used with a 15 minute anneal at ~60W (approximately 450˚C) followed by another 15 minutes at ~200W, during which the chamber temperature reached approximately 830˚C. The graphitization stage was 65s at a constant power of ~1730W, reaching a maximum temperature of 1565˚C based on a previous temperature calibration using the Northrop Gruman optical pyrometer.

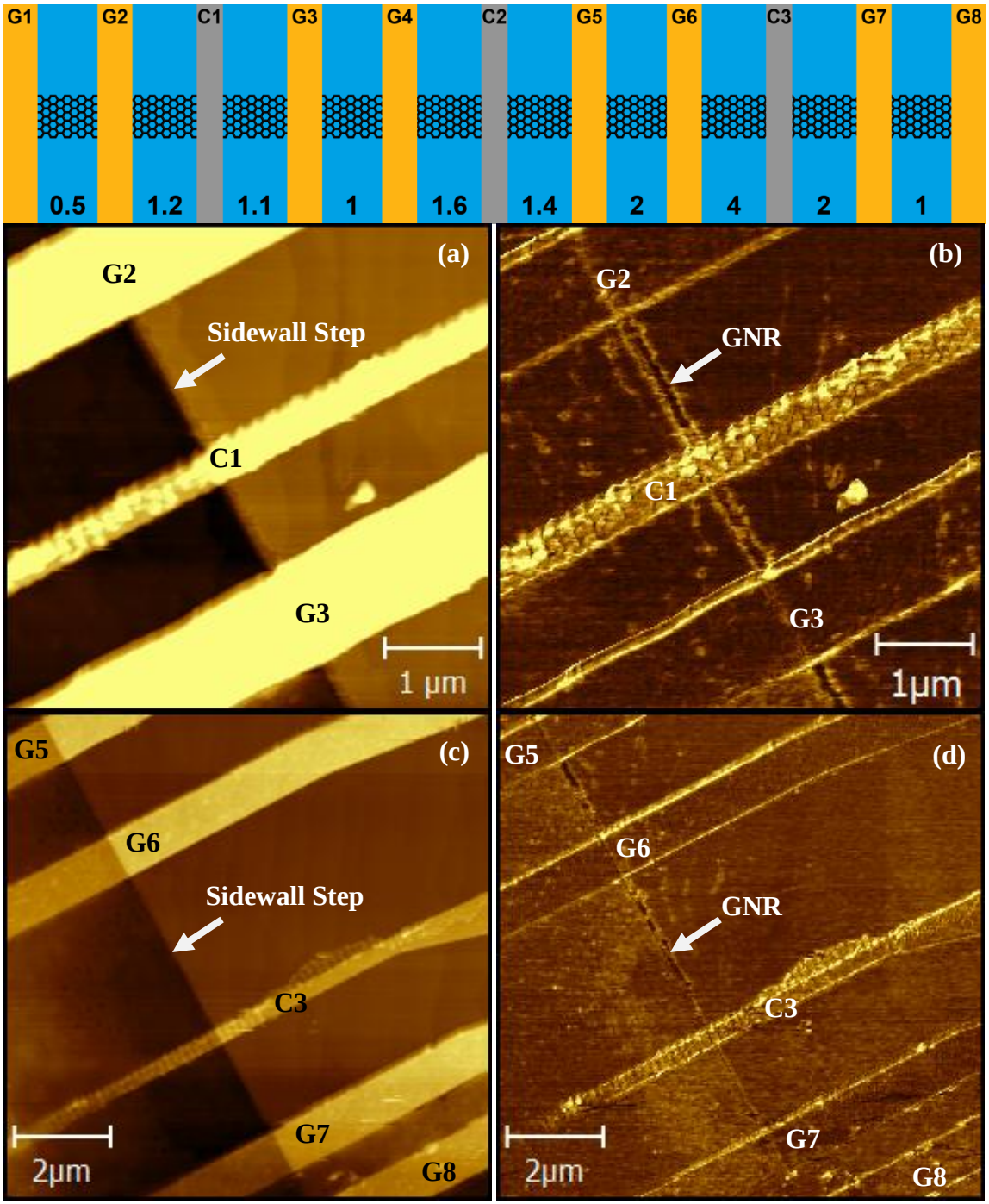

Figure 5.3: Top: 31JH6 TL Device contact diagram, edge to edge distances between contacts are given in microns. (a) AFM Topography and (b) corresponding LFM image taken from G2 to G3. (c) AFM Topography and (d) corresponding LFM image taken from G5 to G8.

Lateral force microscopy performed on this sample showed single ribbons grown on the etched sidewalls with very little additional graphene formation as shown in figure

5.3. 30nm deep trenches were etched with trench walls parallel to the $(10\bar{1}0)$ facet in order to form armchair graphene nanoribbons. Transport measurements were done on two different ribbons, TR and ML. LFM showed the width of ribbon TR to be approximately 100nm, although it appears to be much more narrow near contact C3 as seen in figure 5.3 (d). Based on the contact mode topography scan the sidewall facet appears to be about 22˚, but flattens out near the top edge to an angle of about 4˚. The graphene ribbon covers this gently sloped region but does not extend onto the flat surface.

Tunnel magnetoresistance measurements on 31JH6 TR were performed in Dr. Jiang's cryostat with the assistance of Huan Chao and Wenlong Yu. The sample orientation was fixed with a 28-degree rotation between the magnetic field and the plane of the (0001) face. This orientation aligned the field in the plane of the $(10\bar{1}7)$ facet (the facet typically observed for armchair sidewall ribbons), in order to minimized the perpendicular field component. For this particular ribbon, there was still some magnetic flux through the ribbon due to the growth onto flatter regions. The tunnel resistance was measured using a 3-point configuration with a 1mV AC voltage applied with a lock-in amplifier.

At 6K, the 3-point tunnel resistance of contact C3 displayed very clear reproducible switching during magnetic field sweeps. AC and DC voltage was applied between C3 and G7, current was measured by use of a current amplifier between G7 and ground, and the AC voltage used in the 3-point resistance calculation was measured from C3 to G6. Adjusting the DC bias across the junction changed the magnitude of the switch and could even be used to change the direction of the switch as shown in figure

5.4. The DC bias dependence was measured in two ways. One method was to sweep the magnetic field while at a constant DC bias as shown in figure 5.4 (a). TMR was calculated as the difference in resistance at B=0 between the down sweep and up sweep divided by the lower resistance value. The second method was to sweep the DC bias at 0T after going to +1T and after going to -1T as shown in figure 5.4 (b). The difference in these two curves was used to calculate the TMR as a function of DC bias and agrees remarkably well with the individual data points as seen in figure 5.4 (c). The switch amplitude peaked at 9mV DC, giving a TMR of just under 8%.

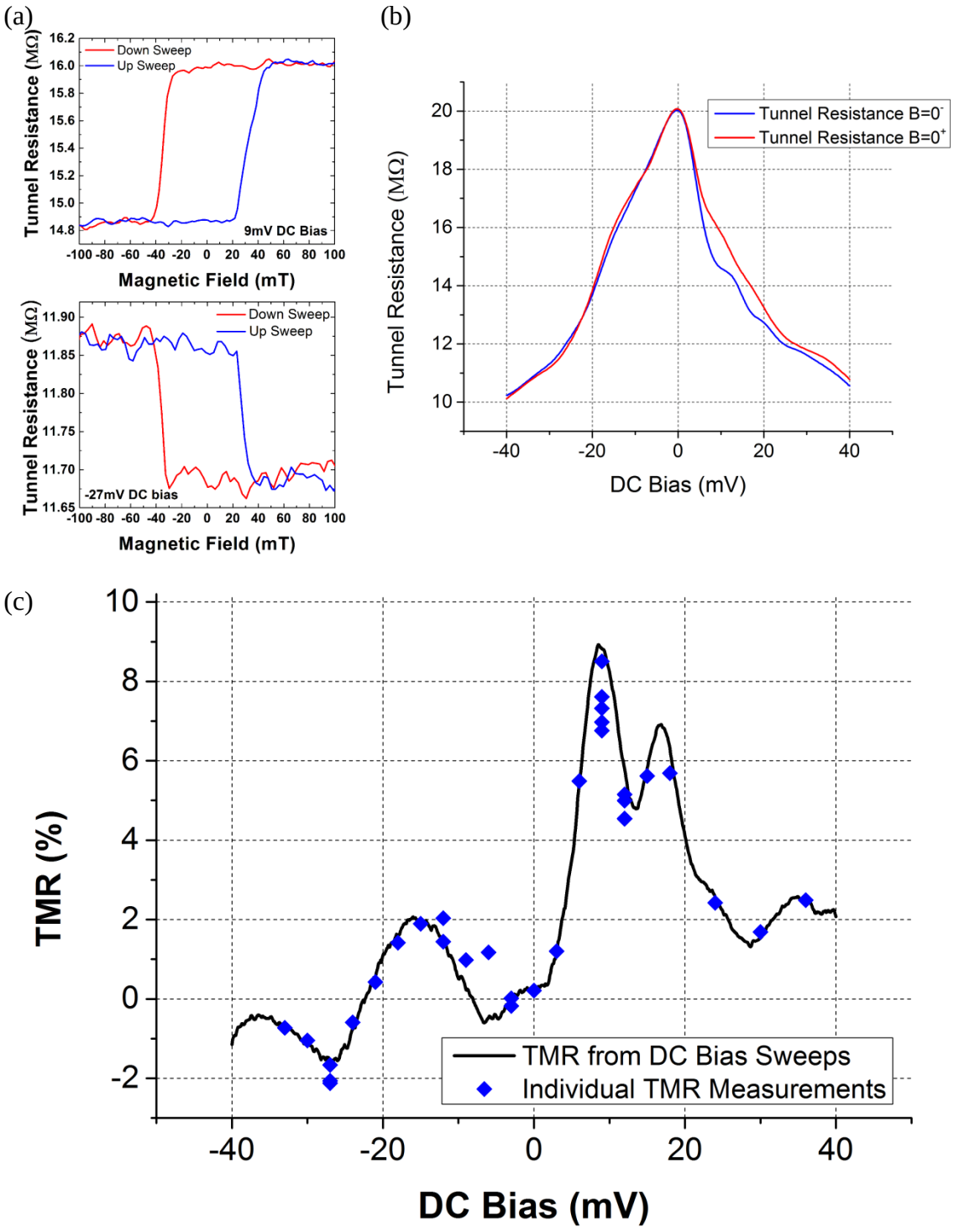

Figure 5.4: DC bias dependence was tested in two ways: (a) the magnetic field was swept with a constant bias across the junction (9mV and -27mV shown), (b) the bias across the junction was swept at 0T after magnetic field was swept to 3T and after going to -3T and back. The difference in these curves was used to calculate the TMR and compared to the values from (a) in (c).

High field sweeps up to 14T were used to investigate how sensitive the magnetization of the GNR is to external magnetic fields. In typical magnetic tunnel junctions between two ferromagnets, the tunnel resistance will return to the low resistance value at high fields as the magnetization of both layers align with the external field. Remarkably, in the Co-GNR system the change in tunnel resistance persisted at high fields. Even at 14T, it had not returned completely to its low resistance state. The tunnel resistance retraced its path as the field was swept back down and the switch was observed as expected when the coercive field strength of the Co contact was reached in the negative direction. Four complete sweeps were done and the tunnel resistance followed an almost identical path every time as show in figure 5.5.

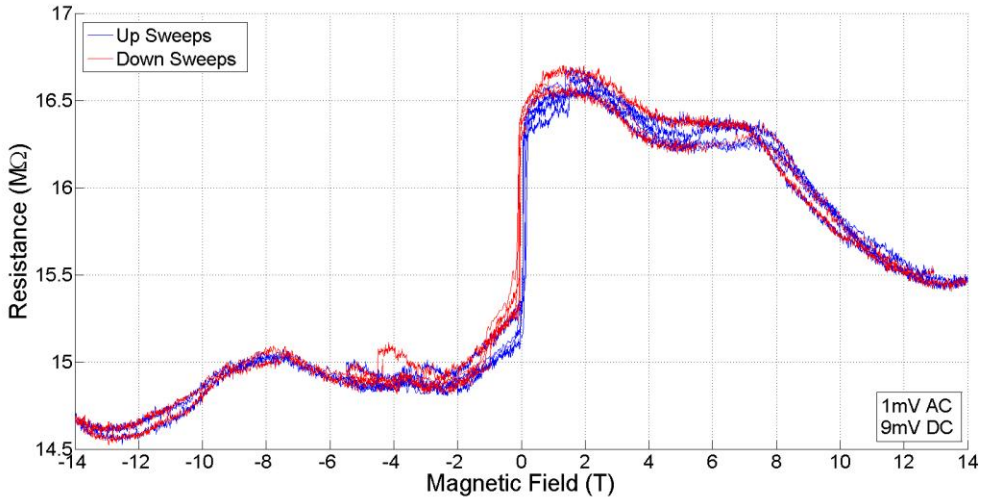

Figure 5.5: Four magnetic field sweeps between +/- 14T, measuring the 3-point tunnel resistance through contact C3.

A two-point resistance measurement was made between adjacent gold contacts G7 and G8 as magnetic field was swept, to act as a control experiment and to measure the magnetoresistance response of the ribbon. The rotation angle was the same 28˚ angle used in the magnetic switch measurements. The two-point resistance was approximately 33kΩ at 0T and the ribbon displayed a slight negative magnetoresistance of 2.5% from

0T to 1T. No switching was observed, which was the expected result since the Pd/Au contacts are non-magnetic and inject a current which is not spin polarized.

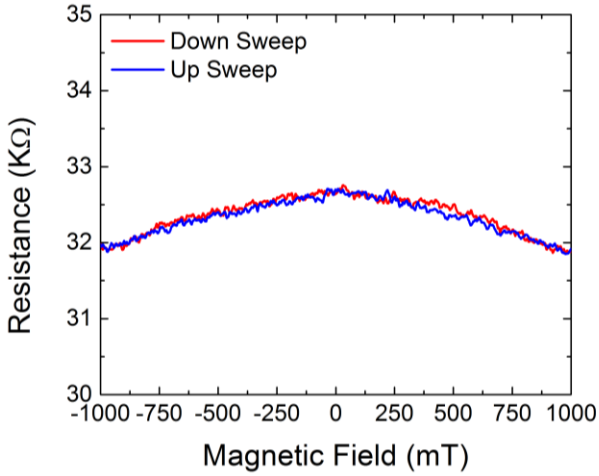

Figure 5.6: Two-point magnetoresistance measurement between contact G6 and G7.

Several months after the completion of the spin switch measurements in Dr. Jiang's lab, sample 42OJ6 was transferred to another sample stage and wire bonded for measurement in the de Heer lab. The tunnel barriers below the Co contacts did not survive the storage, transfer, and re-bonding, preventing further TMR measurements. However, the Pd/Au contacts could still be used for other electronic transport measurements.

The conductance of the ribbon was measured as a function of temperature as the sample was cooled. The conductances between G2 and G8 and between G3 and G4 were measured during a 16-hour cool down from 300K to 4K. The conductance was also measured between G7 and G8 during a separate cool down from 180K to 4K. A 100nA AC current was used for both measurements. The conductance decreases significantly in all of the segments measured as the temperature is reduced. In addition, the ribbon resistance seems to have increased greatly during the time between the initial measurements in Jiang's lab and these measurements. The segment from G7 to G8 was

~32kΩ at 6K in Jiang's cryostat, while the 2-point resistance was approximately 106kΩ at 6K during this measurement. Surface contamination is likely to blame for this huge change in resistance.

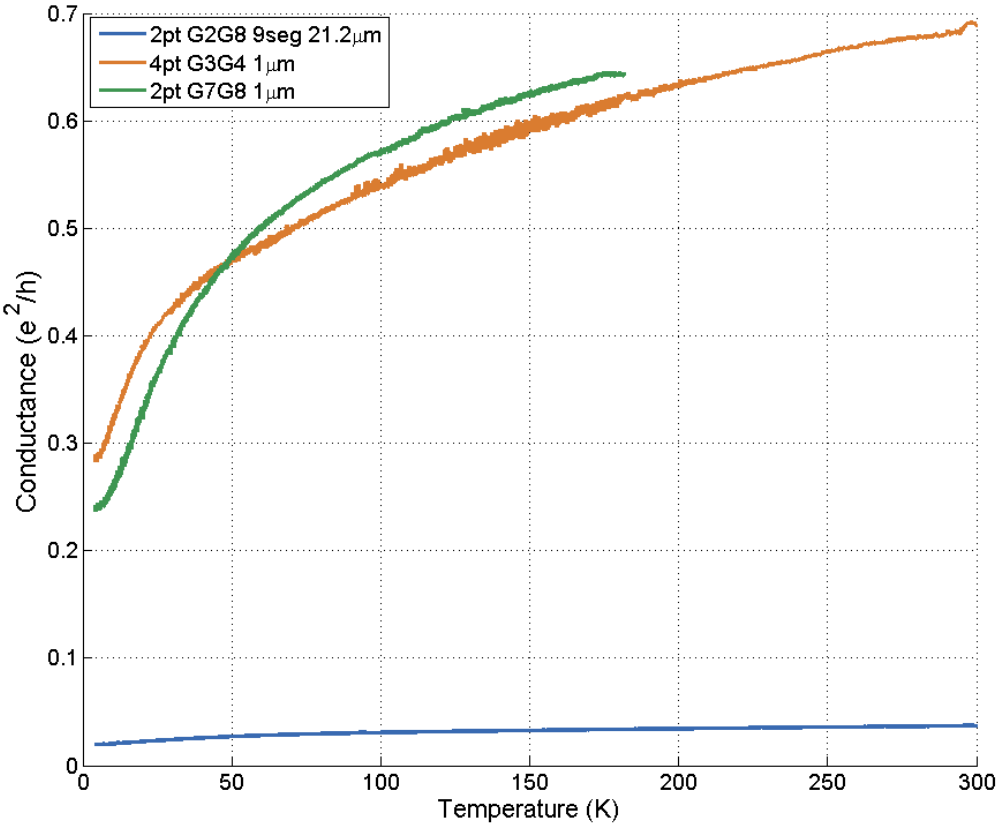

Figure 5.7: Conductance vs Temperature for 31JH6 ribbon TR. The lengths are given as edge to edge distances, for the center to center distances add 1μm

Another experiment that was performed was to measure the magnetoresistance response at various rotational angles in order to try to determine whether the transport was dominated by graphene lying on the sidewall facet or by graphene in the plane of the Si-face. In a flat graphene sheet, transport is generally not affected by the in-plane component of magnetic field because electronic motion can only couple to the component of magnetic field perpendicular to the sheet [111]. Thus, the angle at which the

maximum magnetoresistance is observed should be perpendicular to the graphene nanoribbon being measured.

To determine the "magnetic normal" of the ribbon, the magnetic field was swept between 0T and 9T while the resistance was measured using a lock-in amplifier supplying a 100nA AC current. The sample was rotated in ~15˚ increments between 90˚and -13˚ and a full 9T sweep was performed at each angle. The unit vector normal to the ribbon was calculated as a function of facet angle and rotation angle. The dot product of this normal vector and magnetic field was used to determine the magnitude of the magnetic field perpendicular to the ribbon at each angle. If the magnetoresistance is only sensitive to a single component of magnetic field perpendicular to the ribbon, then the proper choice of facet angle (and resulting normal vector) should align all of the magnetic field sweeps when plotted as a function of the perpendicular magnetic field strength.

For 31JH6 TR it was observed that the magnetoresistance was dependent on only a single component of the magnetic field with an apparent facet angle of 10-15˚ depending on the ribbon segment measured. A 4-point measurement between G3 and G4 gave a 11˚ facet (see figure 5.7), a 2-point measurement between G7 and G8 gave a 10˚ facet, and a 2-point measurement across the length of the ribbon from G2 to G8 gave a facet of 15˚. There was one segment measured on ribbon TR that could not be properly fit using a single component of the magnetic field. However, the measurement used a Co contact as one of the voltage probes, which may be responsible for the strange response. See appendix A for this data.

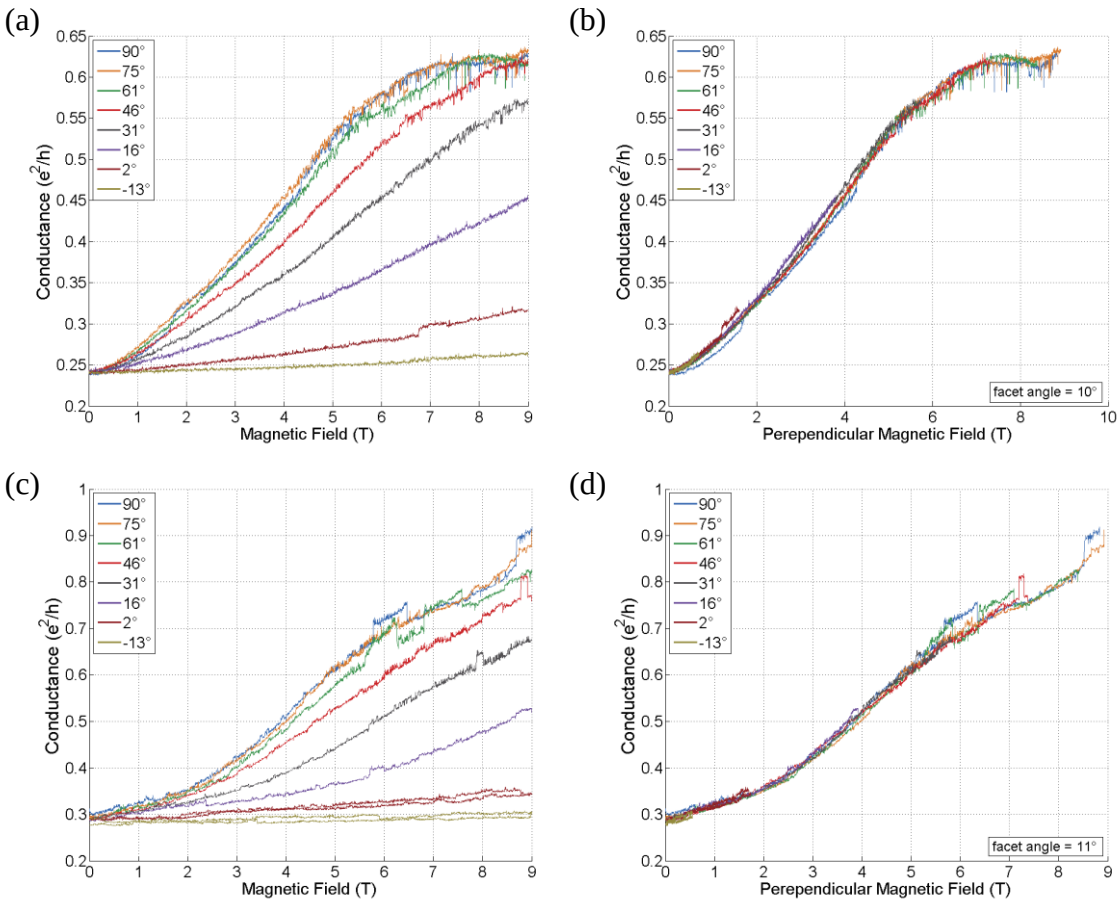

Figure 5.8: Top: 2-point conductance measured between G7 and G8 as a function of the (a) total magnetic field and (b) component of magnetic field perpendicular to a 10˚ facet. Bottom: 4-point conductance measured between G3 and G4 as a function of the (c) total magnetic field and (d) component of magnetic field perpendicular to an 11˚ facet.

5.3 Sample 42OJ6

Sample 42OJ6 was graphitized in a graphite crucible with a 1mm diameter leak hole. The growth recipe was 10 min at 800˚C for degassing, 1150˚C for 20 min to remove surface oxide, and graphitization at 1490˚C for 90s. Transport measurements were done on armchair ribbon TL grown on a 22nm deep trench wall oriented parallel to the $(10\bar{1}0)$ facet. The sample was significantly overgrown as shown in figure 5.9. Additional graphene appears to form in small recesses 2-4nm deep. The graphene can be identified in LFM thanks to its low frictional force and the I-AFM measurement confirms that these regions are conducting. The additional graphene appears to form in small

recessed regions 2-4nm deep. Although it was significantly overgrown, the sample showed remarkable electronic and magnetic properties including very high sensitivity to spin polarized current.

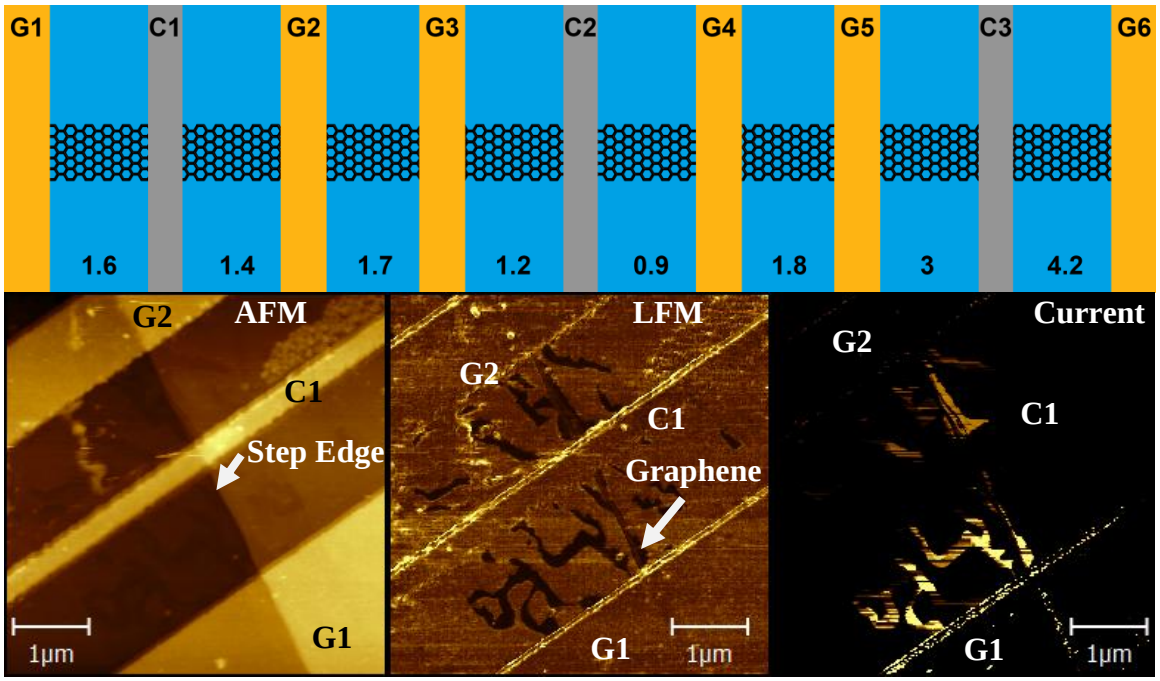

Figure 5.9: Top: Device schematic for 42OJ6 TL. Bottom: Topography, lateral force, and current measured on 42OJ6 ribbon TL between contacts G1 and G2. Contact G1 was used as ground for the C-AFM measurement. The C-AFM confirms that the smooth regions are in fact conducting. The images were taken about a year after the transport measurements in cryostat. Oxidation of the Co and settling of material on the gold surface is believed to be the reason that the contacts do not show much current flow.

Sample 42OJ6 was inserted into the de Heer cryostat for low temperature transport measurements. The conductance of ribbon TL was measured during a 16-hour cool down from 300K to 4K. A 100nA AC current was applied from contact G1 to G6, while voltage was measured between various pairs of Pd/Au contacts using a lock-in amplifier. The conductance did not have a strong dependence on temperature, changing no more than 25% on any of the segments during the cool down. The conductance peaked between 70K and 100K for all segments and appeared to level off around 7K. The behavior is different than that of 31JH6, which showed a constant decrease in

conduction. The difference in the conductance vs temperature relation may be due to the influence of the graphene overgrowth on this sample.

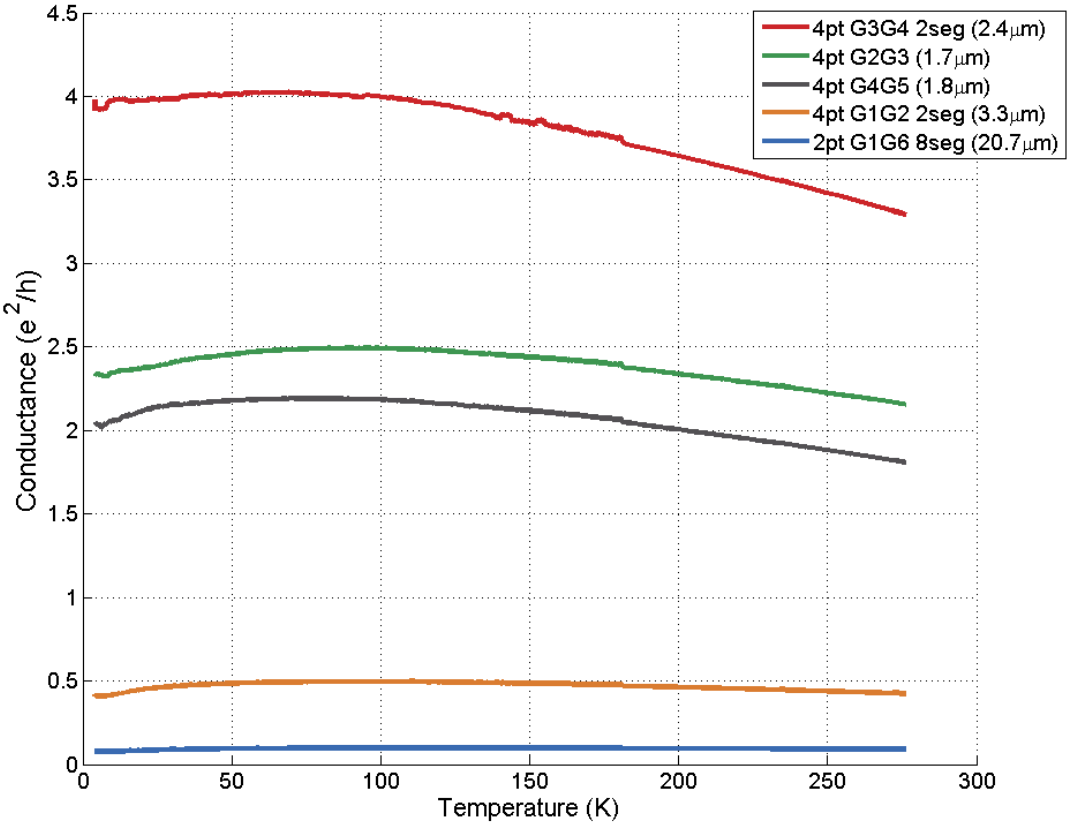

Figure 5.10: Conductance vs Temperature measured on 42OJ6 ribbon TL measured during a 6hr cool down using a 100nA AC current. Lengths are measured from contact edge to contact edge, for center to center distances add 1μm.

Initial 3-point tunnel magnetoresistance measurements on contact C1 showed very clean reproducible switching despite a relatively low tunnel resistance of only 500kΩ. Using a 1nA AC current the TMR was approximately 9%. Increasing the AC current to 100nA caused the TMR to go up to 15% but the tunnel resistance was reduced to approximately 250kΩ. Unfortunately, during subsequent DC bias dependence measurements the tunnel contact resistance became unstable. The sample was removed from the cryostat and stored in liquid nitrogen. It was later re-inserted into the cryostat,

after which the contact resistance of C1 was approximately 1300kΩ. Oxidation during the sample's brief exposure to air is likely the cause of the increased tunnel resistance.

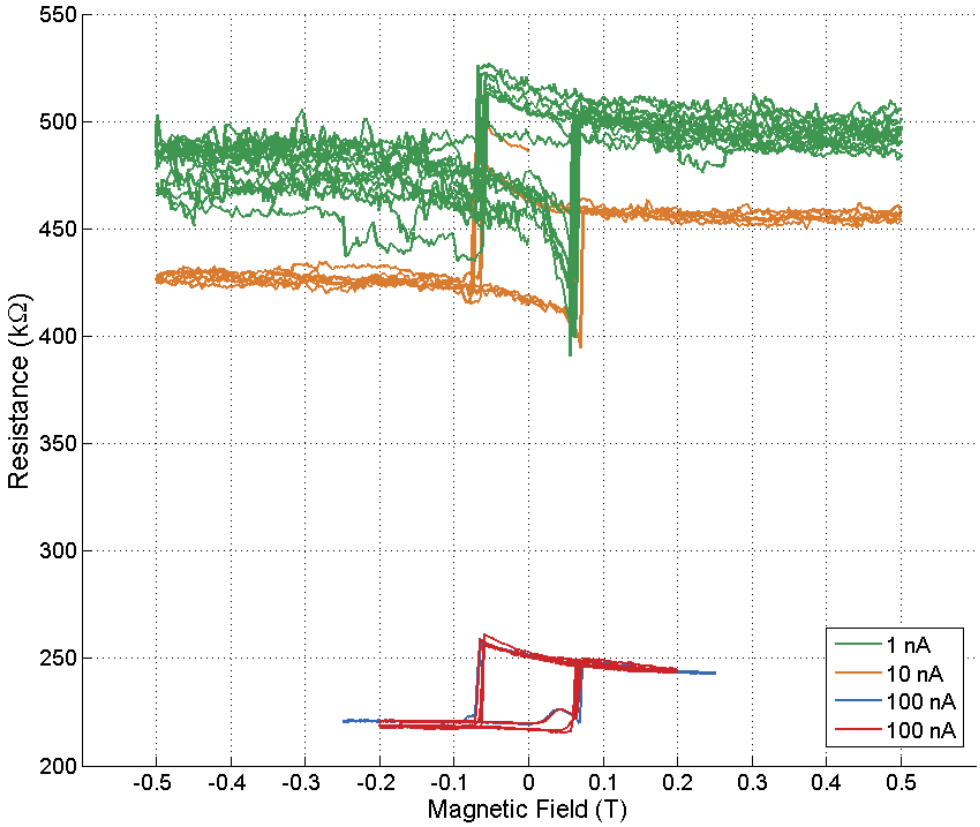

Figure 5.11: 3-point tunnel resistance measurements on contact C1 using constant current mode.

Further spin switch measurements on 42OJ6 TL contact C1 after re-insertion showed very large TMR responses, as high as 38%. This would indicate a spin polarization of 45.6% in the graphene nanoribbons based on equation 4.11, assuming P_{Co}=35% [112]. The spin polarization could be even larger if the GNR's polarization direction is not parallel to the magnetization axis of the Co contact. In addition, the spin polarization of the graphene charge carriers appeared to be strongly resistant to external magnetic fields, as the change in resistance persists under external fields up to 6T.

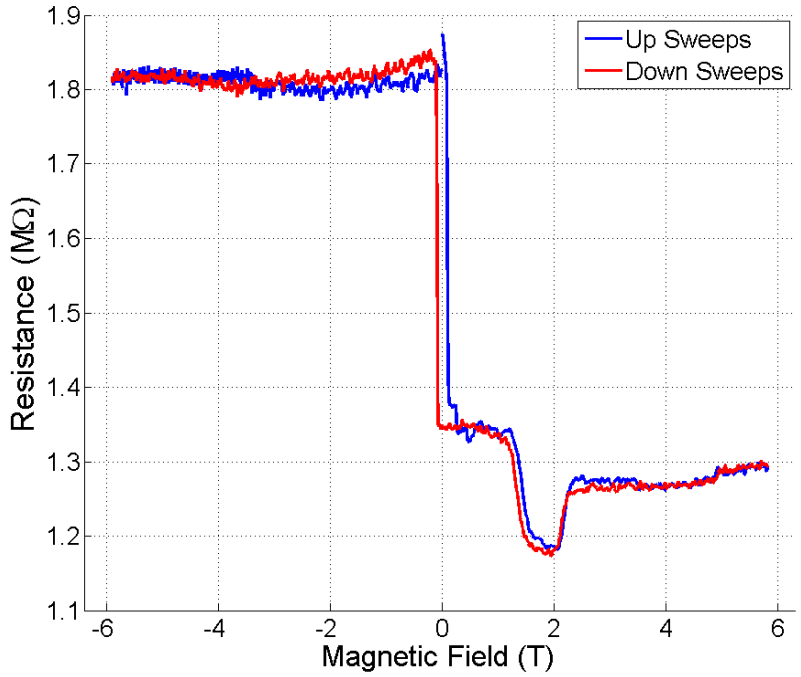

Figure 5.12: 3-point tunnel resistance measured up to +/- 6T external field. 2mV AC and 2mV DC applied from C1 to G1, Voltage measured C1 to G2.

Although the ribbon showed some very impressive spin switching, it also displayed some very odd behavior. During many of the spin switch measurements two high resistance states were often observed, and subsequent sweeps would sometimes alternate between a very large switch of 30% or more and a smaller switch of 15% or less. In addition, despite resisting external magnetic fields up to 6T, complete reversal of the graphene spin direction occurred at seemingly random intervals. As the temperature was increased, the spin polarization direction in the graphene appeared to become increasingly unstable and three distinct resistances were observed at 30K. At 70K to 90K, instead of the normal resistance loop, there was a slight increase in resistance as the field crosses 0T until the cobalt magnetization flipped and the resistance returned to its low value. This would seem to indicate that at these temperatures the magnetization direction of the graphene is no longer fixed and instead follows the direction of the

applied field, as in a paramagnet. Finally, at 100K the spin switching effects were completely lost and constant resistance was observed. The Curie temperature of Co is 1388K [70], so these changes in behavior are not due to a transition in the Co. After cooling back to 4K, the switch behavior was different than it had been initially. In future experiments, it would be interesting to apply a magnetic field during the cool down to see if the graphene magnetization can be controlled.

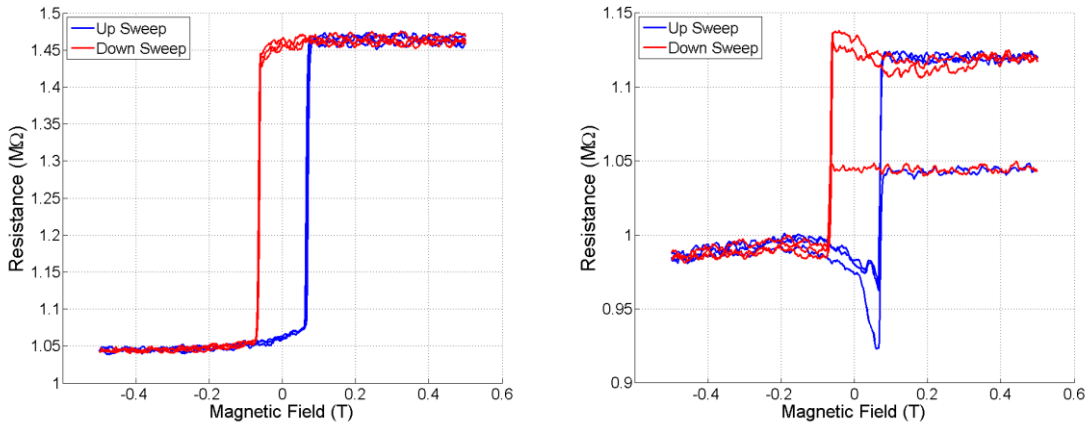

Figure 5.13: (a) 3-point tunnel resistance measurement showing 38% TMR over three consecutive magnetic field sweeps. 2mV AC and -10mV DC applied from C1 to G2, Voltage measured C1 to G1. (b) 3-point tunnel resistance displaying two high resistance states during three consecutive sweeps. 2mV AC and -8mV DC applied from C1 to G2, Voltage measured C1 to G1.

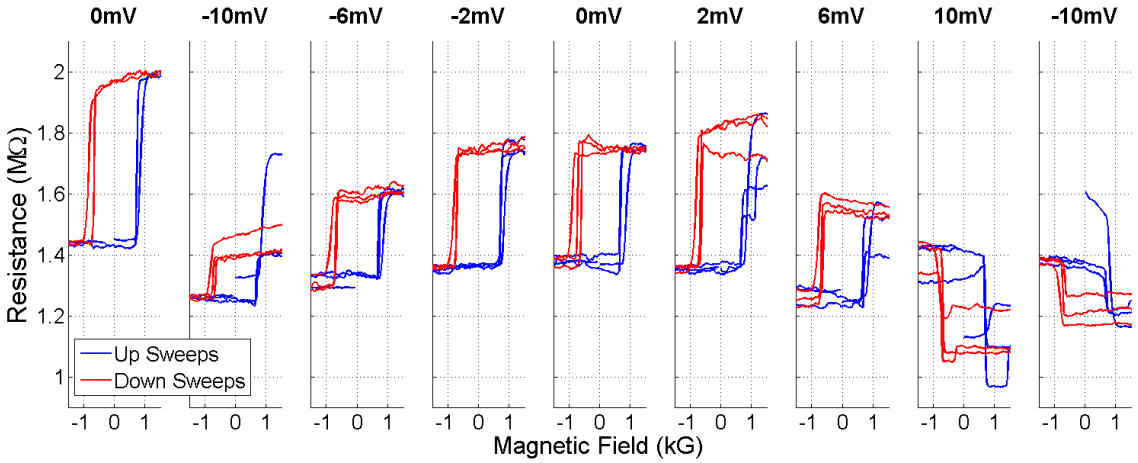

Figure 5.14: 42OJ6 TL 3-point tunnel resistance at 4K, various DC biases. 2mV AC applied from C1 to G1, Voltage measured C1 to G2. Data plotted in the order it was taken to present the sudden change in behavior over time, such as the direction reversal between 6mV and 10mV. Field in kG for clarity of plot axes.

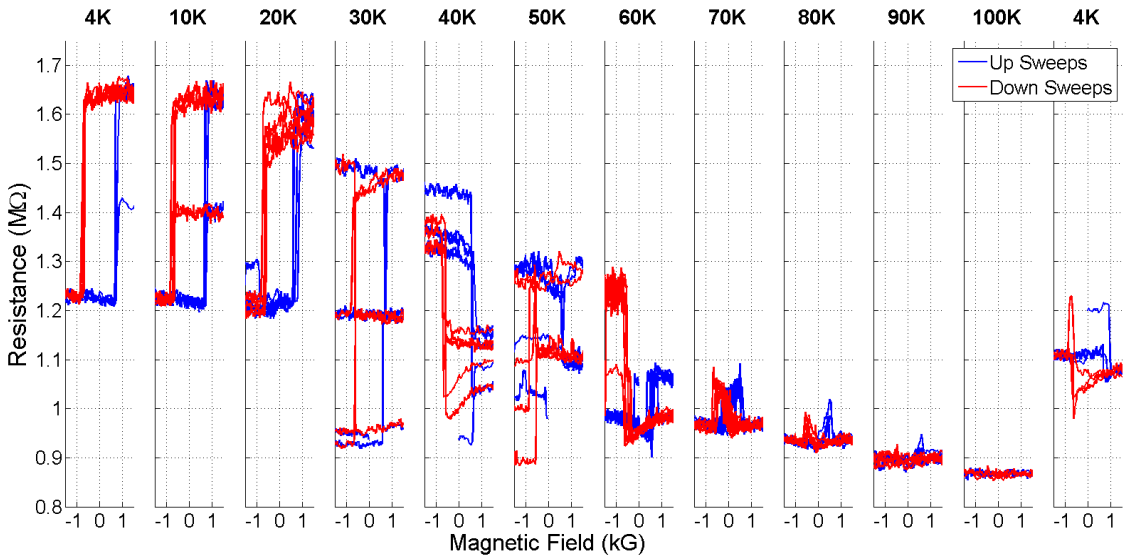

Figure 5.15: 42OJ6 TL C1 3-point tunnel resistance, temperature dependence of switch. Constant voltage mode: 1mV AC and -2mV DC applied from C1 to G2 (current amplifier on G2), Voltage measured C1 to G1. Data plotted in the order it was taken, note that the 4K behavior changed after the temperature cycle. Field in kG for clarity of plot axes.

To test if the electron spin polarization in the graphene was momentum dependent a DC bias was applied across the ribbon while the tunnel resistance was measured using a lock-in amplifier. A DC voltage was applied between contacts G1 and G2 using the Keithley 4200, while a 3-point AC resistance measurement was made on contact C1 with G2 serving as ground and voltage measured between C1 and G1. Before this measurement was carried out, the tunnel resistance dropped significantly, to approximately 100kΩ. Despite the drop in tunnel resistance, the sensitivity to spin polarized current persisted and an increase in the TMR was observed, showing magnetic switching as high as 75%. This indicates a graphene spin polarization of 78% based on equation 4.11 and a cobalt polarization of 35% [112]. The switch behavior showed very little dependence on the current direction, but died off when a large enough DC bias was applied.

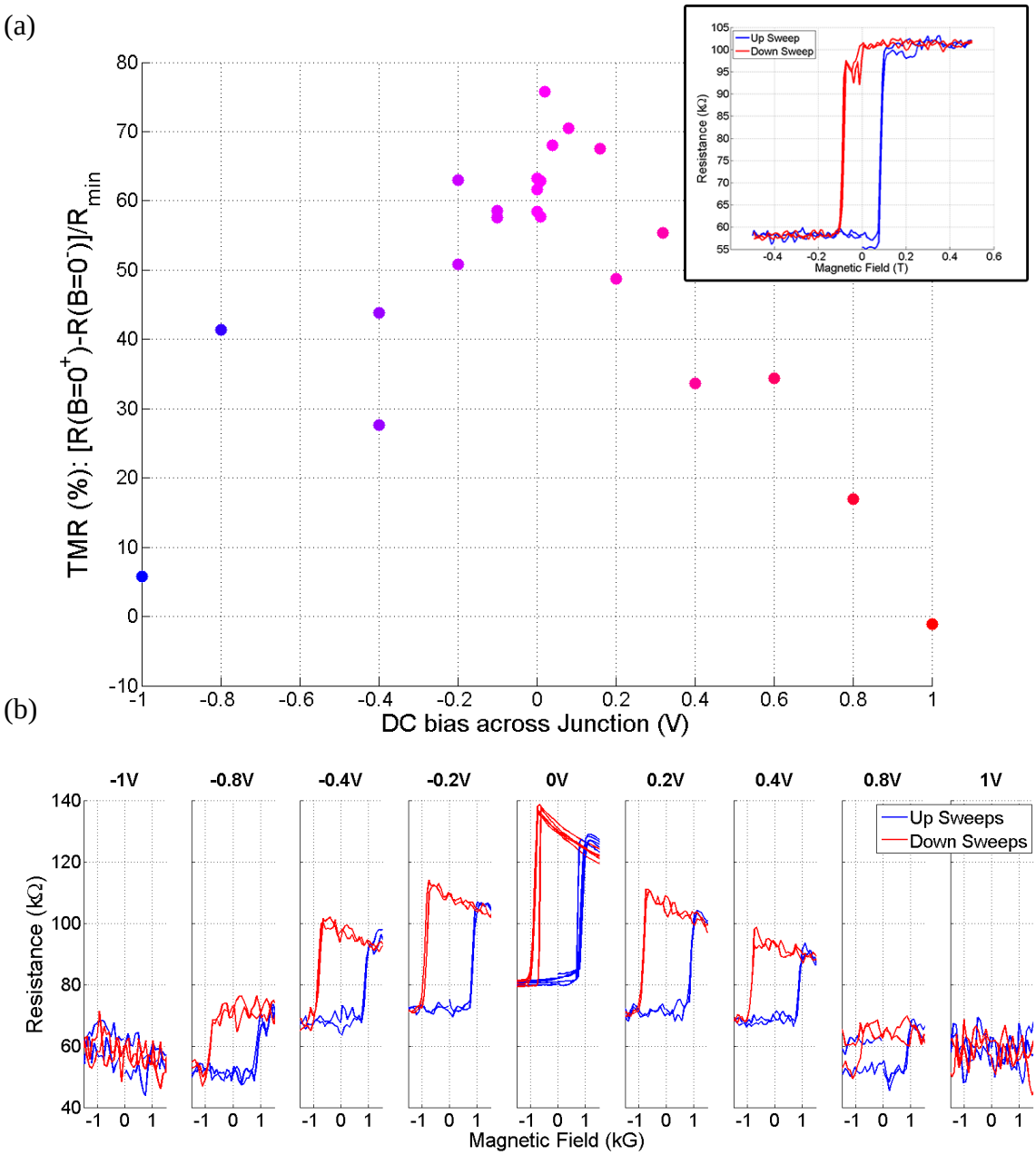

Figure 5.16: (a): TMR measured with various DC biases applied across the ribbon. DC bias G1 to G2, 3- point tunnel resistance measured in constant current mode 2nA from C1 to G2, voltage measured C1 to G1. Inset: largest TMR measured at 20mV DC bias. (b) A sampling of the spin switch measurements performed, field in kG for clarity of plot axes.

Standard magnetoresistance measurements using all gold contacts were also performed on ribbon TL. The ribbon displayed a slight negative magnetoresistance, increasing its conductance by 10% at 9T. Magnetoresistance was measured at various angles to test if it was sensitive to the total magnitude of the field or only sensitive to a

specific directional component of the field as described in 5.2. For ribbon TL we see that a facet angle of -7˚ aligns the sweeps done at different angles. This is very different from the results obtained on the single sidewall ribbon 31JH6 TR, and indicates that the additional graphene overgrowth is likely responsible for a significant portion of transport.

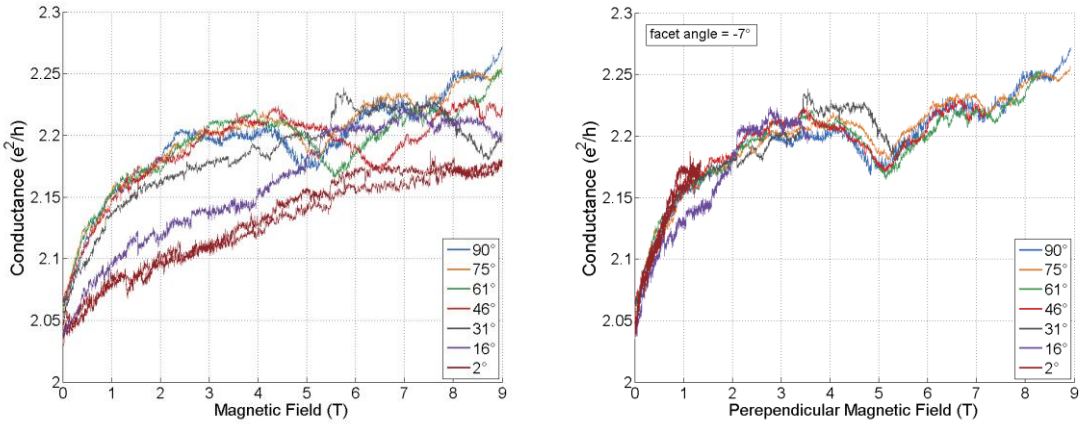

Figure 5.17: 4-point conductance measured between G2 and G3 as a function of the (a) total magnetic field and (b) component of magnetic field perpendicular to a -7˚ facet.

5.4 Sample 42OJ7

Sample 42OJ7 was graphitized in a graphite crucible with a 1mm diameter leak hole. The growth recipe was 10 min at 800˚C for degassing, 1150˚C for 20 min to remove surface oxide, and graphitization at 1485˚C for 85s. Several additional ribbons approximately 100nm wide grew next to the sidewall ribbon. They were rotated between 25 to 30 degrees relative to the etched sidewall, putting them very close to the orientation of zigzag ribbons. Although the ovegrowth was still significant it seemed much more ordered than the extra graphene that formed on 42OJ6. The sidewall ribbon itself was slightly overgrown varying in width between 100nm to 300nm. Contacts were patterned on ribbon TR and it was inserted into the de Heer cryostat for low temperature transport measurements.

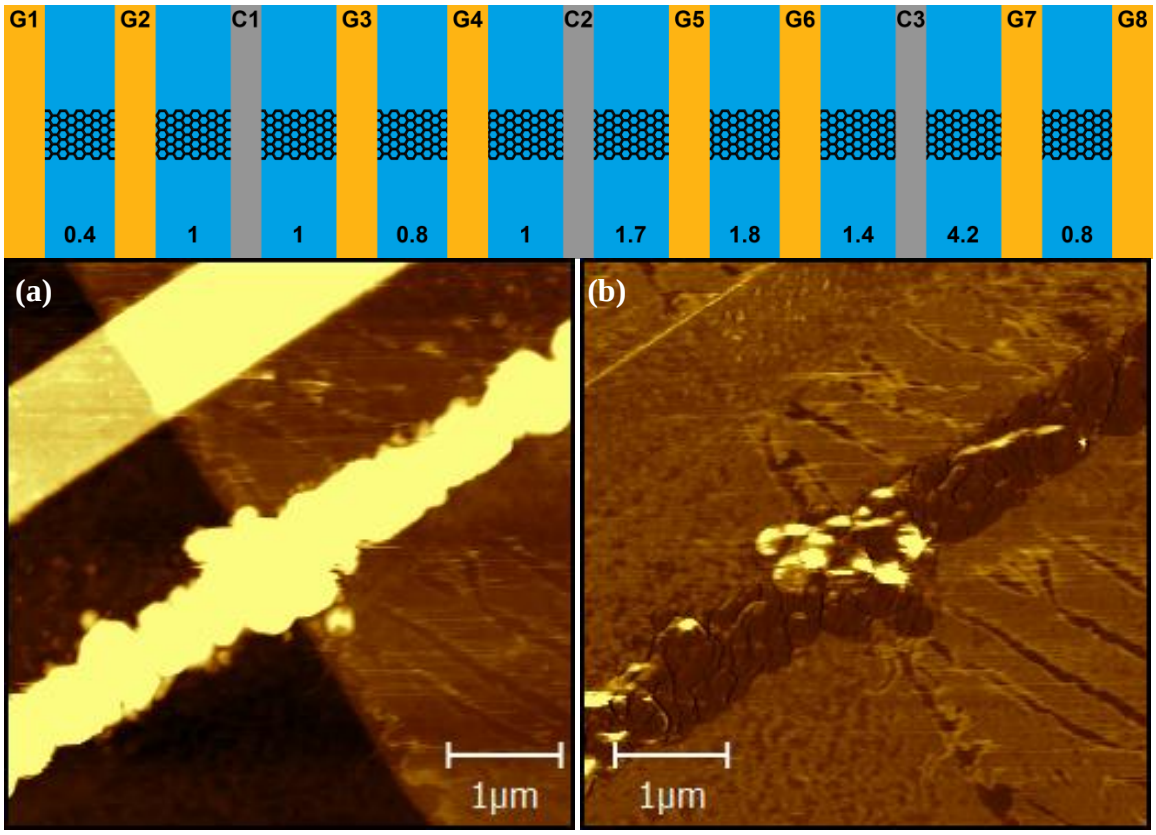

Figure 5.18: Top: Device schematic for 42OJ7 TR with edge-to-edge distance between contacts listed in microns. Gold contacts are ~1μm wide and Co contacts are ~300nm wide. (a) AFM topography and (b) LFM images taken around contacts G6 and C3. Images were taken over one year after the initial transport measurements and it appears that Co contact reacted with something during storage.

The conductance of ribbon TR was measured during an 18-hour cool down from 260K to 4K. A 10nA AC current was supplied and measured using a lock-in amplifier. The relationship between conductance and temperature was very similar to that observed in ribbon 42OJ6 TL with a slight increase until ~100K and then a decrease in conductance that begins to level off around 7K. Both 42OJ6 and 42OJ7 had significant overgrowth, unlike 31JH6, which may explain why the increase in conductance during cool down at temperatures above 100K is only observed in these samples. Below 100K, all three ribbons display a similar behavior.

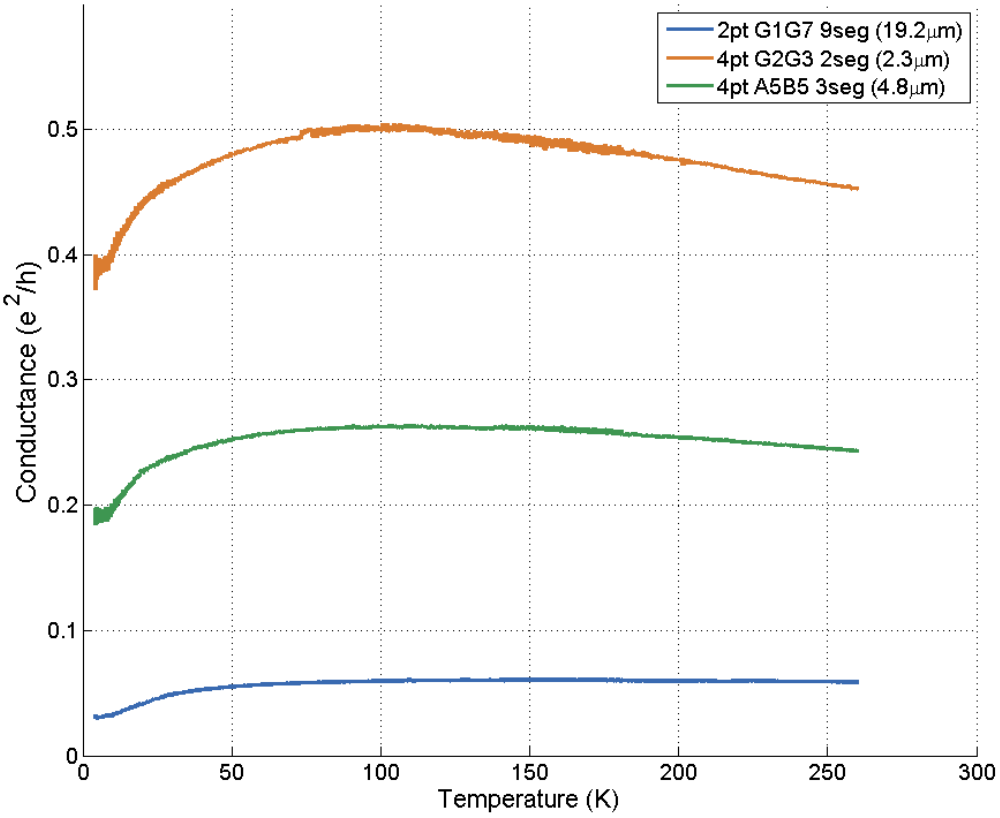

Figure 5.19: Conductance vs Temperature for 42OJ7 ribbon TR, measured during an 18hr cool down with a 10nA AC current. Lengths are given from contact edge to contact edge, for center-to-center distances add 1μm.

Initial spin switch measurements performed on contact C1 yielded a relatively stable resistance loop with an average TMR of 3.7% using a 3-point configuration with a 2mV AC bias. The DC bias was changed in 2mV increments from -8mV to +8mV and three sweeps were performed at each bias value. The TMR did display DC bias dependence increasing to 5.4% at 8mV and decreasing to 3% at -8mV as shown in figure 5.20. The switch direction did not change within the measured voltage range. 8mV was the maximum DC bias applied, as there was concern that higher biases would damage the tunnel barrier, which already had a fairly low tunnel resistance. Angle dependence measurements were then performed using 8mV DC and 2mV AC, the conditions that gave the largest TMR.

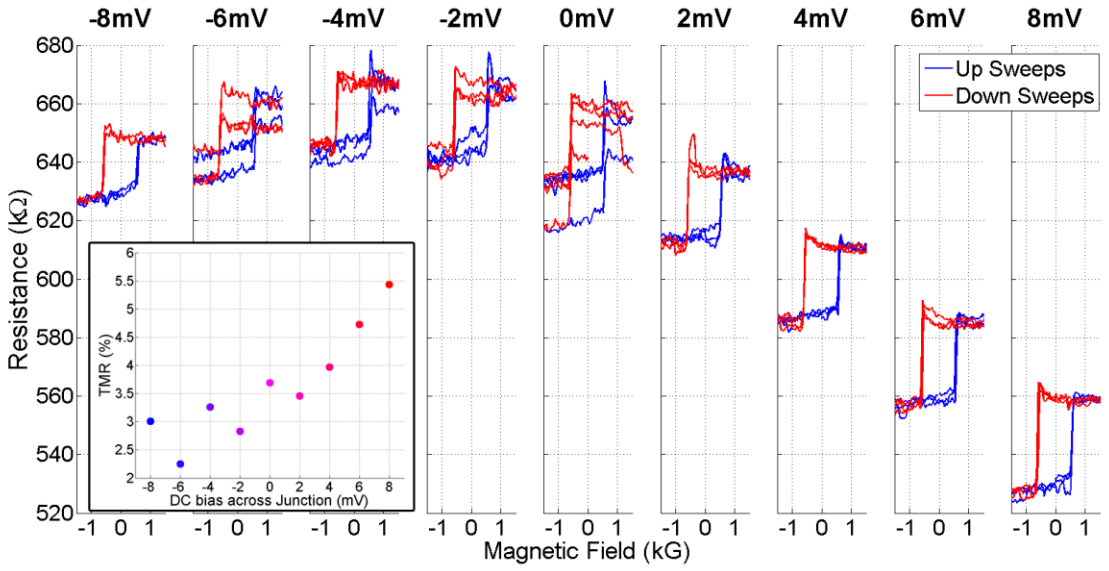

Figure 5.20: 3-point tunnel magnetoresistance measurements on contact C1. 2mV AC plus various DC biases applied from C1 to G3, current was measured through G3, and AC voltage was measured C1 to G2. Field in kG for clarity of plot axis. Inset: TMR as a function of applied DC bias.

The tunnel resistance was relatively stable during the angular dependence measurements between -20˚ and 79˚, although a few sudden changes did occur. Initially, the high resistance value was 560kΩ and the low resistance value was approximately 525kΩ, giving a TMR value of 6%, very close to the value observed previously. During the last down sweep at -20˚ the resistance went from 560kΩ to 510 kΩ, a TMR of 9.5%. This larger switch was observed for all of the -10˚ and 0˚ sweeps, then it returned to its initial behavior for several sweeps before jumping back to the 9.5% TMR during the sweep at 59˚. Both loops were very stable and reproducible and it is unclear why the change occured. A significant jump in tunnel resistance from 520kΩ to 690kΩ was observed at the very beginning of the first 69˚ sweep and the TMR was reduced below 3%. After the 79˚ sweep the tunnel resistance became very noisy and unstable, never returning to its initial clean behavior. The full magnetic field sweeps for each angle are shown in figure 5.21 (a).

The average TMR at each angle is plotted in figure 5.21 (b). Other than the unexplained jumps, the TMR was very consistent, seemingly unaffected by the angle of the external field. Sweeps at -20˚, 10˚, 20˚, 29˚, 39˚, and 49˚ had nearly identical TMR of approximately 6%, while sweeps at -10˚, 0˚, and 59˚ (as well as the last down sweep at -20˚) had consistent 9-10% TMR loops. In addition, the shape of the resistance loop was quite consistent. The tunnel resistance curves up slightly before both the down switch and up switch (for all measurements before the jump to 690kΩ), and remains relatively flat up to +/-0.5T.

The only property of the loop that did have a clear dependence on angle was the coercive field strength. The change in coercive field strength is expected for a narrow Co contact with a magnetic easy axis, as used in this experiment. In such a contact, it is the component of the field parallel to the magnetic easy axis that is relevant rather than the total field strength. Thus, the total field strength required to flip the magnetization should have a 1/cos(θ) dependence. To check this relationship the coercive field strength was plotted as a function of angle and fit using equation 5.2 as shown in figure 5.21 (c). B_0 is the coercive field strength at θ=0˚, and θ_0 accounts for any shift between the expected angle and the true angle of the contact relative to the magnetic field. The resulting fit of B_0=57.6mT and θ_0=4.6˚ agreed very well with the experimental data.

$$B = \frac{B_0}{\cos(\theta - \theta_0)} \tag{5.2}$$

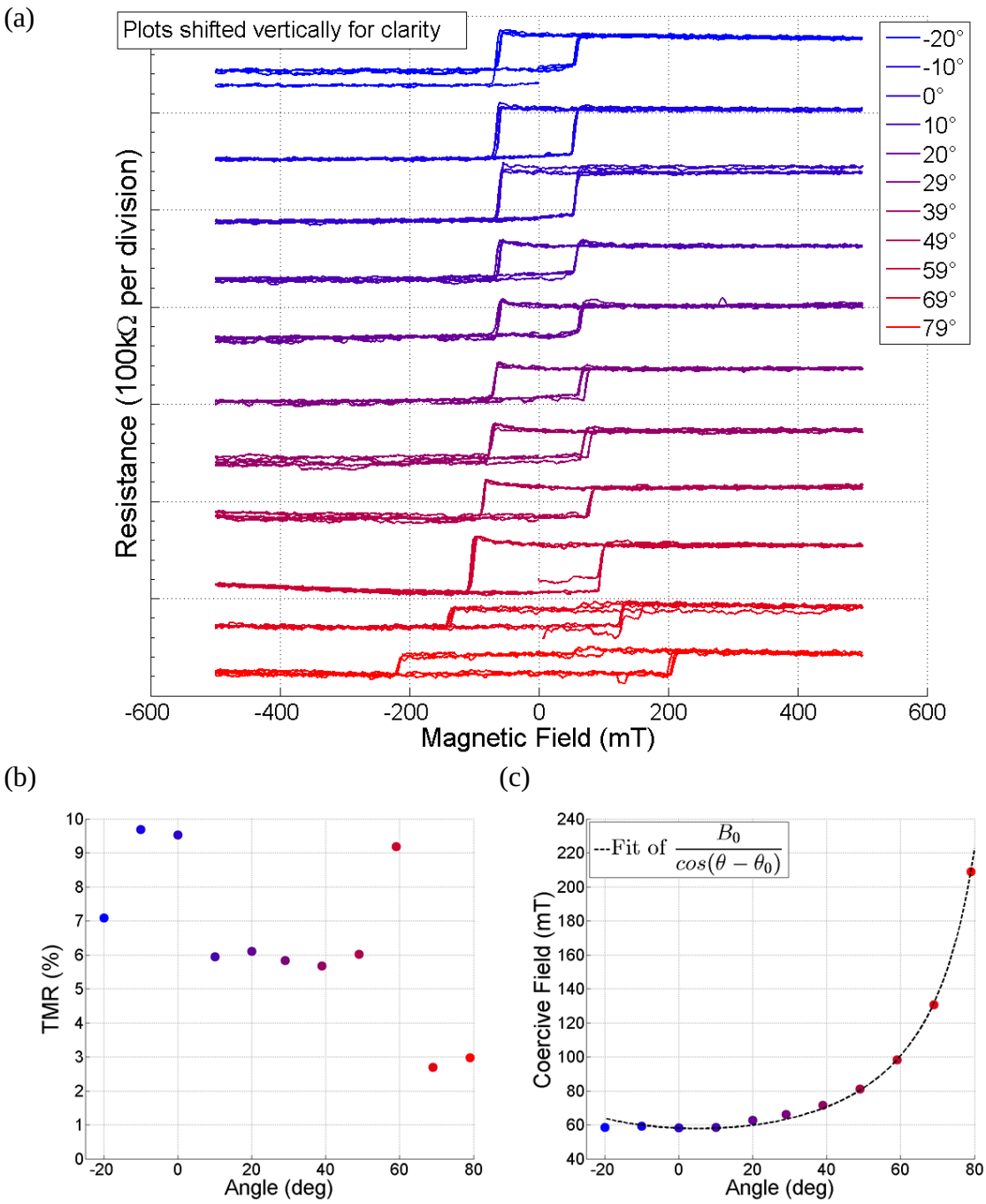

Figure 5.21: (a) 3-point tunnel resistance on contact C1 measured as a function of magnetic field at various angles. (b) Average TMR based on three full sweeps at each angle. (c) Coercive field strength vs angle fit using equation 5.2.

Although the tunnel resistance became very noisy, a few more measurements were taken before the contact was lost completely. It was observed that at angles beyond 90˚ the switch direction was reversed and upon returning to 0˚ the switch orientation

returned to its original direction as shown in figure 5.22. This change in switch direction was expected because at angles beyond 90˚ the cobalt contact is magnetized in the opposite direction relative to the field as shown in figure 5.22.

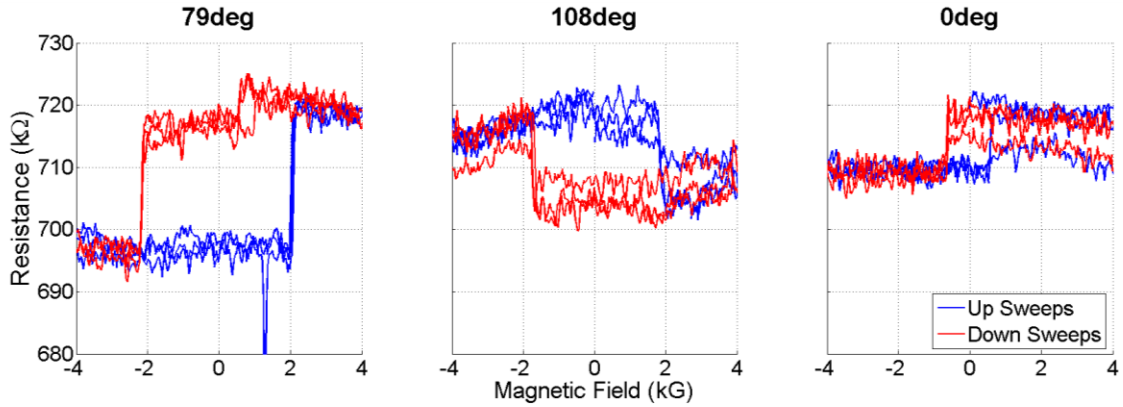

Figure 5.22: A series of TMR measurements on 42OJ7 TR contact C1 at different angles showing the switch direction flipping relative to the applied field when the angle goes from 79˚ to 108˚ and returning to its original orientation when the angle is rotate back to 0˚. Field in kG for clarity of plot axis.

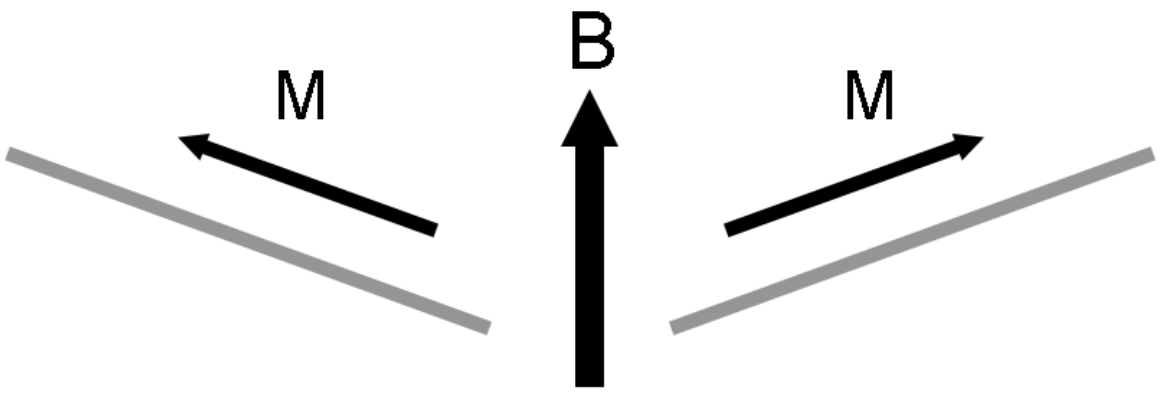

Figure 5.23: Illustration of effect of angle on magnetization direction of the cobalt contact. The left contact is oriented 70˚ relative to the applied field and magnetizes right to left, while the contact pictured on the right is oriented 110˚ relative to the applied field and magnetizes from left to right. This leads to an inversion of the switch behavior relative to the applied field because a "positive" field will align the magnetization in the "negative" direction when the angle is above 90˚.

Angle dependence measurements were also made on contact C3 using constant current mode. A 10nA AC current was applied from C3 to G3, while the voltage was measured between C3 and G7. A relatively normal spin switch loop with ~2% TMR was

observed at 0˚, but the behavior changed drastically as the magnetic field direction approached 90˚ relative to the sample surface. At very low angles, tunnel resistance increased when the cobalt spin direction flipped during both the up sweeps and down sweeps. The tunnel resistance slopes downward before the switch in order to create a continuous loop as seen in figure 5.24 (a). Interestingly, if one focuses on the change in resistance at B=0T and calculates TMR as described in equation 5.1, it is relatively constant despite the very odd shape of the magnetoresistance loop at angles near 90˚. Figure 5.24 (b) shows these results with the percent change in resistance during the up sweep plotted in blue, the percent change in the down sweep plotted in red, and the TMR measured at B=0T plotted in green. Each point represents the average of 3 sweeps.

(a)

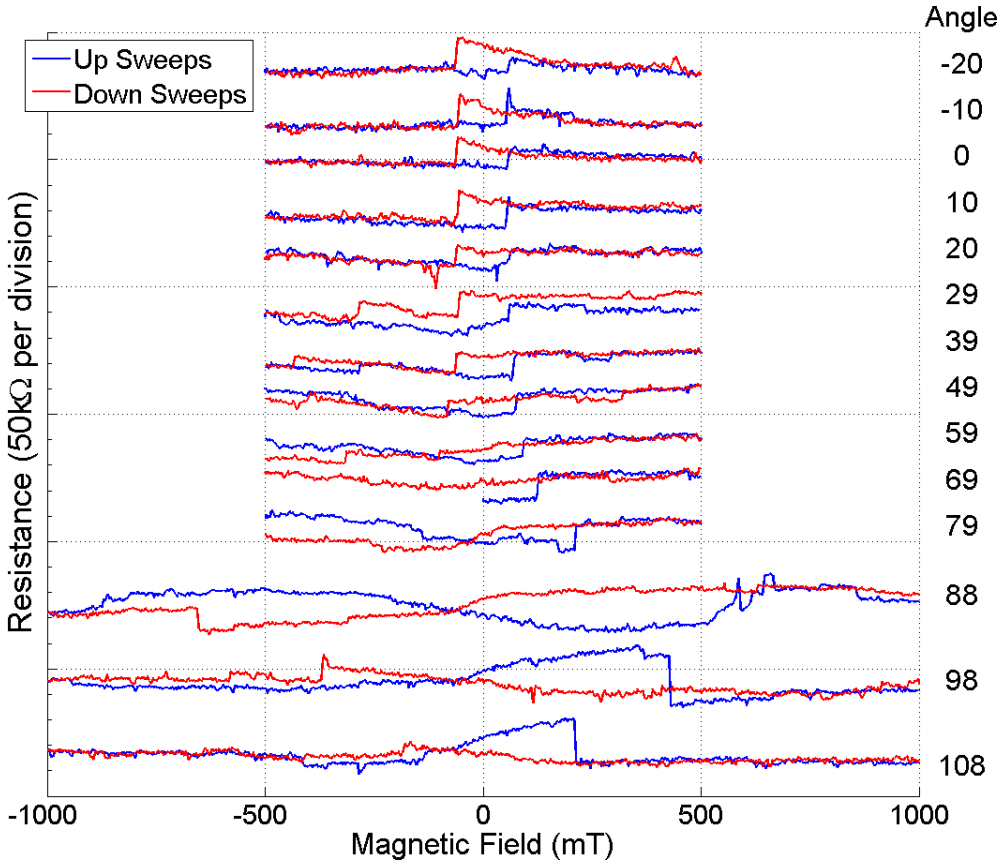

(b)

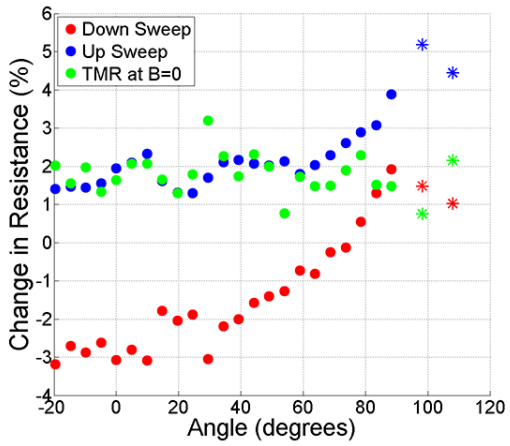

(c)

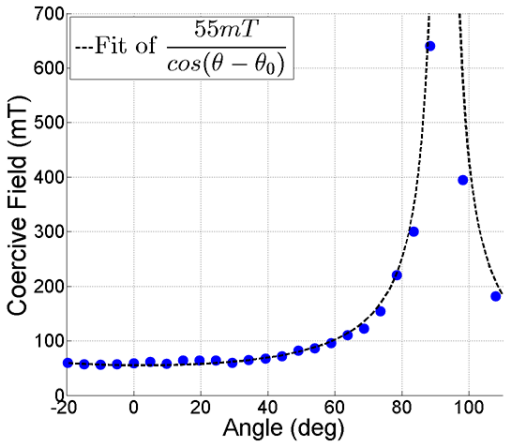

Figure 5.24: Results of 3-point tunnel resistance measurements on 42OJ7 TL contact C3 at various angles. (a) Selected plots are shown to illustrate the evolution of the switch behavior. R_0~360kΩ for all, large ticks are 50kΩ and small ticks are 10kΩ (b) The average switch up, switch down, and TMR at B=0 are plotted for each angle. Beyond 90˚ the magnetic field aligns the cobalt magnetization in the opposite direction so these data points have been inverted and marked with a * (c) Coercive field strength vs angle and 1/cos(θ) fit.

5.5 Sample 52JHY

Sample 52JHY was graphitized in a graphite crucible with a 1mm diameter leak hole. Sidewall ribbons were grown on 18nm deep trench walls. The growth recipe was 10 min at 800˚C for degassing, 1150˚C for 20 min to remove surface oxide, and graphitization at 1485˚C for 65s. Non-contact AFM measurements with an EFM tip showed a facet angle of ~19˚. A lower facet angle of around 11˚ was measured using a SHOCONA tip in contact mode. However, non-contact measurements are generally more accurate for determining facet angle as the tip effect is more pronounced in contact mode measurements.

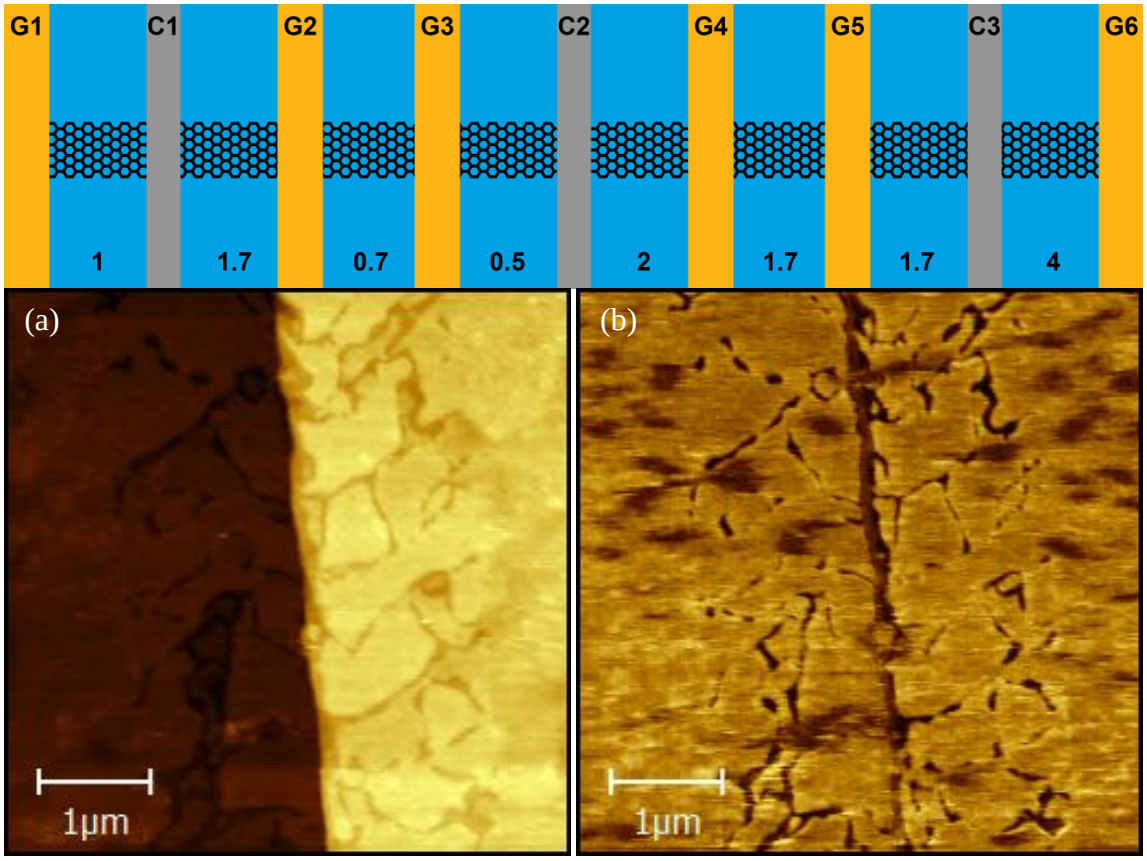

Figure 5.25 Top: Device schematic of 52JHY with edge-to-edge contact distances given in microns. Gold contacts are ~1μm wide and Co contacts are approximately 300nm wide. Bottom: (a) AFM Topography and (b) Lateral Force measurements taken on a 4μm long segment of 52JHY ribbon TL

Ribbon TL, shown in figure 5.25, is an armchair oriented ribbon. It is approximately 100nm wide based on LFM measurements. There was patchy overgrowth nearby as shown in the LFM image in figure 5.25 (b). The additional graphene appears to form in recessed regions of the SiC surface, 2-4nm deep. The graphene abruptly stops ~1.5µm from the ribbon on either side due to the REI etching step done using an O_2 plasma.

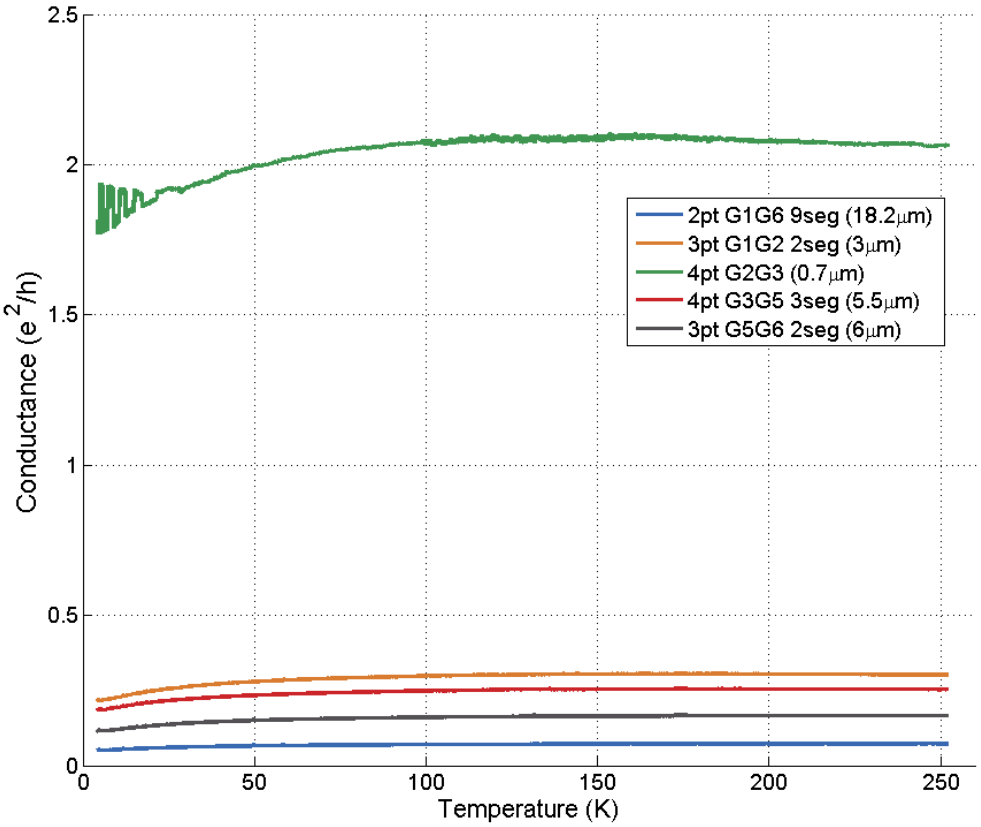

Figure 5.26: Conductance vs Temperature for 52JHY ribbon TL, measured during a 27hr cool down with a 100nA AC current from G1 to G6. Lengths are given from contact edge to contact edge, for center-to-center distances add 1µm.

Ribbon 52JHY TL was inserted into the de Heer cryostat for low temperature transport measurements. The ribbon conductance was measured during a 27 hour cooldown from 250K to 4K. A 100nA AC current was applied from contact G1 to G6 while the voltage was measured across various ribbon segments using gold contacts. The

conductance increased very slightly as the temperature was decreased from 250K, peaking between 150K and 200K depending on the segment. Cooling to 4K reduced the conductance from its peak value by ~15% for G2G3 and 25-30% in the other segments. The conductance began to level off around 6-7K as observed in the other ribbons measured. The strange jumps in the conductance of segment G2G3 had a period of 1 hour and continued when the temperature was held at 4K. Thus, it appears these jumps are due to some outside electronic signal being picked up rather than a temperature dependent effect. Such periodic noise was not observed in any other measurements.

Initial room temperature measurements of the tunnel barriers on this contact were around 5MΩ. However, after cooling the tunnel resistance was much lower, around 100kΩ. Despite this relatively low tunnel resistance, spin dependent conductance through the barrier was observed, with a TMR of approximately 3%. Measurements were made in constant voltage mode with a 1mV AC bias applied from contact C2 to contact G3. Current was measured using a lock-in amplifier connected between G3 and ground, and the 3-point voltage was measured between C2 and G5. The DC bias dependence was measured in 1mV increments between -5mV and 5mV. Three complete up and down sweeps were performed at each bias before changing to the next bias value and the entire set of measurements was repeated a second time to examine the reproducibility of the switch behavior. The results of these DC bias dependence measurements are shown in figure 5.27.

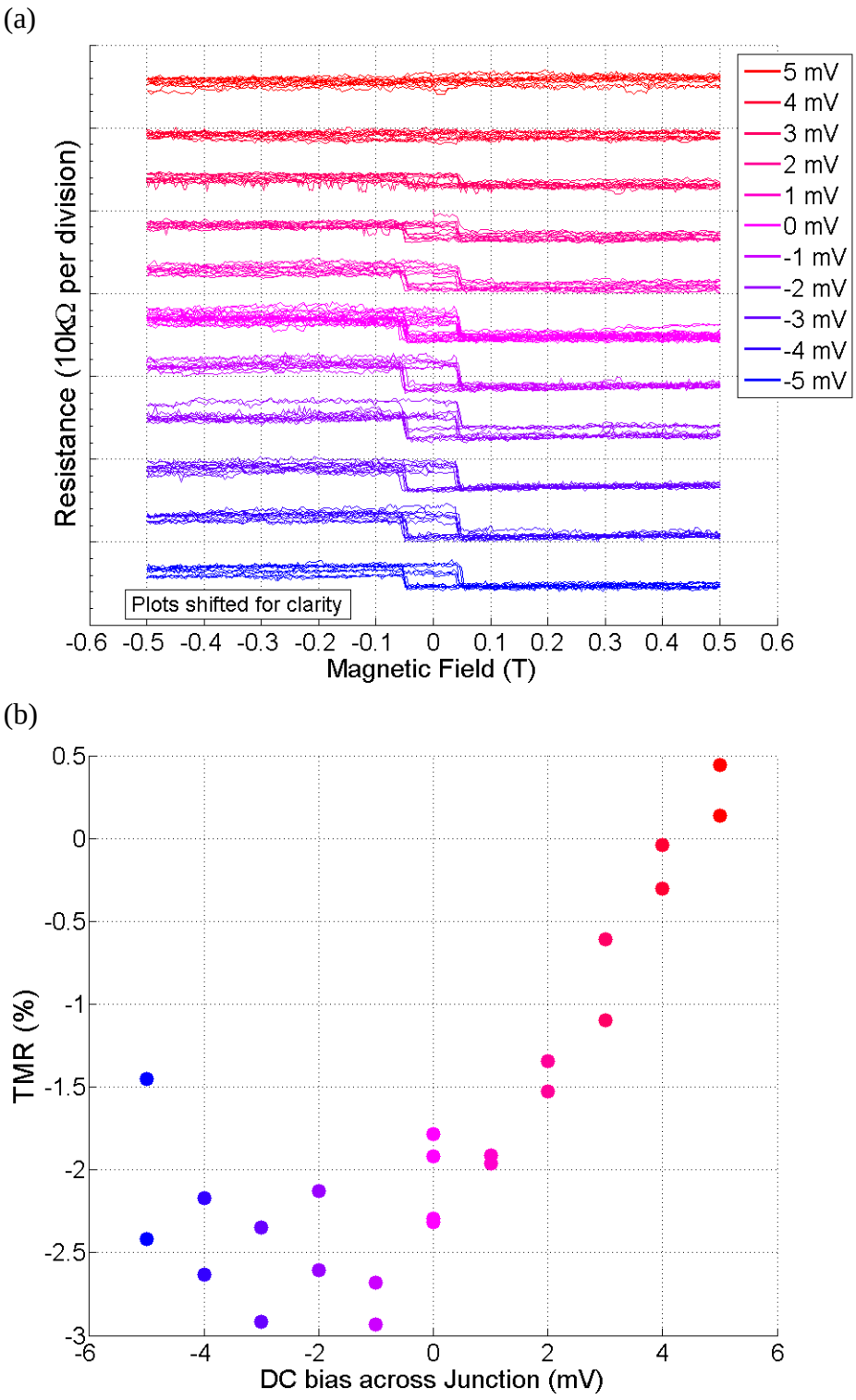

Figure 5.27: (a) 3-point tunnel resistance measurements on 52JHY TL. R_0~110kΩ for all plots. Six full sweeps were done at each DC bias value (12 at 0mV). (b) TMR vs DC bias. Each point represents the average TMR from a set of three full sweeps.

5.6 Cobalt Magnetoresistance Measurement

To ensure that the effects observed were not purely due to the cobalt itself, 2-point magnetoresistance measurements were made on some of the Co contacts. To allow for these measurements, cobalt contacts with pads on both sides of the ribbon were patterned. The resistance through the cobalt was measured while the magnetic field was swept in order to obtain an independent measurement of the cobalt's magnetoresistance. Figure 5.28 shows a 2-point resistance measurement across contact C2 of sample 42OJ6. A 1μA AC current was used. The sample orientation was -8˚. The total change in resistance was less than 1% and unlike the tunnel resistance measurements it did not exhibit the clear spin switch loop with a high and low resistance state.

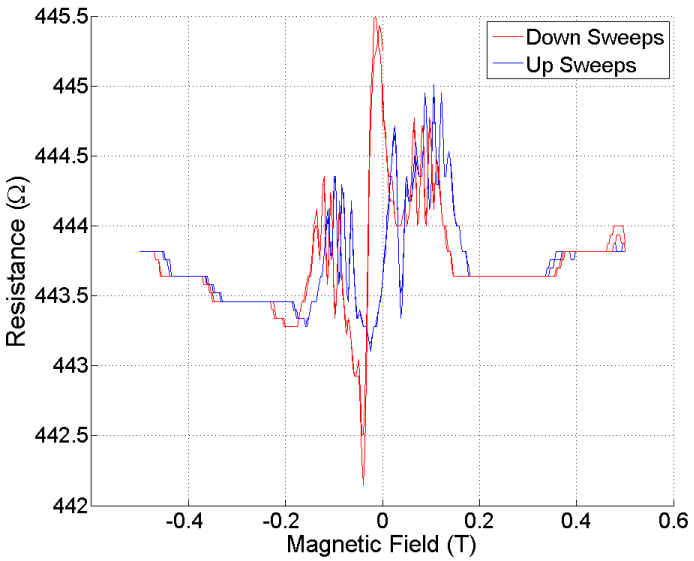

Figure 5.28: 2-point resistance measured across contact C2 on sample 42OJ6

Figure 5.29 shows a series of 2-point resistance measurements done on sample 52JH3 TL across contact C1 using a 10nA AC + 10nA DC current through the contact. The magnetoresistance of the contact was measured at 0˚, 30˚, 60˚, and 90˚. The total change in resistance for each sweep was less than 2% and again no clear switching loop was observed. In the 0˚ measurement there is a 1-2% spike in resistance just after

crossing 0T in both directions (figure 5.30 (a)), likely due to the re-arranging of the magnetic domains in the Co. At higher field strengths, the resistance returns to its original value as the domains become aligned. This behavior is completely different than that of the tunnel resistance measurements, where there is a clear loop with a high resistance state in one field direction and a low resistance state in the other field direction as shown in figure 5.30 (b).

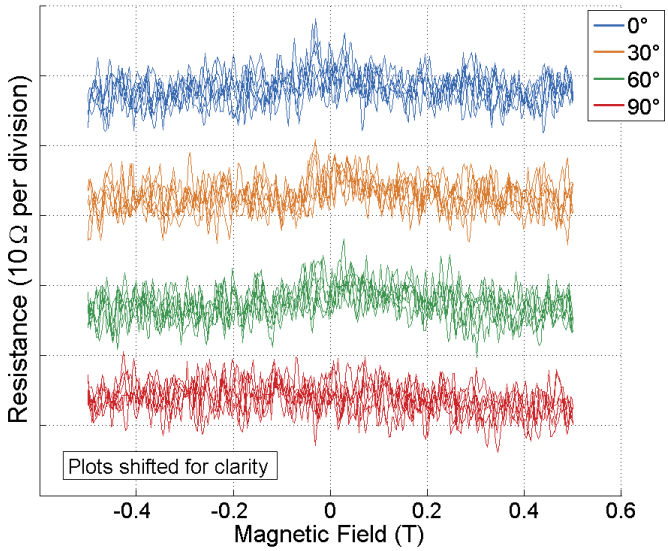

Figure 5.29: 2-point resistance measured across contact C1 on sample 52JH3 TL as a function of magnetic field, measured at four different rotations. R_0~464kΩ for all sweeps

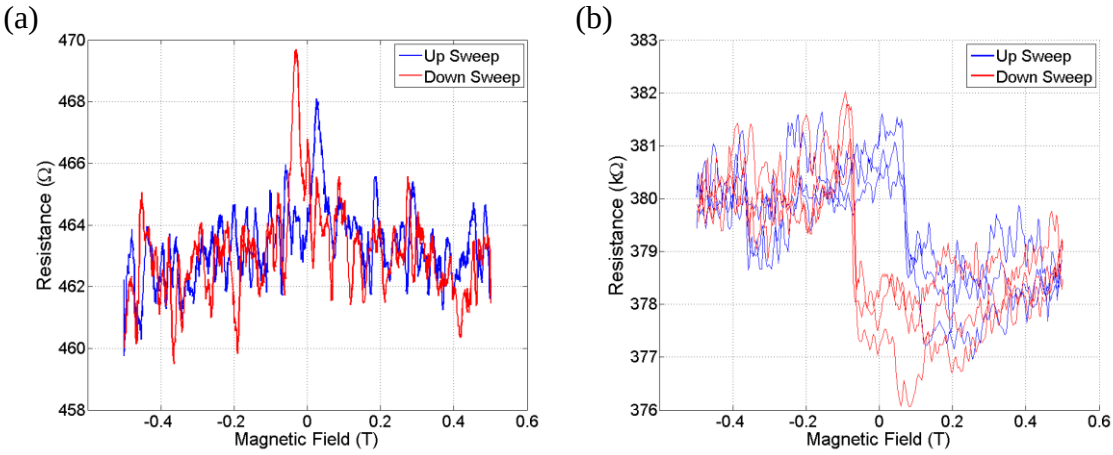

Figure 5.30: (a) 2-point resistance measurements across contact C1 on sample 52JH3 TL at 0˚, the average resistance from three up sweeps and three down sweeps is plotted. (b) 3-point tunnel resistance measurement at 0˚ using contact C1 on sample 52JH3 TL for comparison.

CHAPTER 6

CONCLUSIONS

Epitaxial graphene on silicon carbide is an exciting material for the exploration of fundamental physics and for its potential applications in future electronic devices. The CCS furnace design is very versatile and provides a simple, scalable method for producing high quality graphene. Altering the background gases, growth time, and growth temperature can significantly alter the resulting graphene. In addition, SiC pre-patterning allows for the growth of graphene nanostructures that do not suffer from the rough edges caused by traditional lithography techniques.

Nanostructured epitaxial graphene produced using SiC pre-patterning is shaping up to be one of the most interesting forms of graphene yet observed. The unique properties of these GNRs are just beginning to be revealed. The work in this thesis shows that Si-face epitaxial graphene nanoribbons with clean edge terminations have a strong sensitivity to spin polarized current. Magnetic switching was observed in multiple ribbon samples with TMR as high as 75% observed in the cobalt/GNR MTJs. Such magnetic switching has not been demonstrated in any lithographically patterned ribbons, showing that these GNRs are truly unique. The observation of magnetization dependent tunnel resistance demonstrates that the charge carriers in these ribbons are in fact spin polarized, as implied by the single channel ballistic transport measurements performed by Baringhaus et al. [110].

In addition, the GNRs exhibited very high magnetic coercivity at low temperatures. In sample 31JH6 the change in tunnel resistance persisted up to 14T and in 42OJ6 the change persisted up to 6T, which was the largest magnetic field applied. To

the best knowledge of the author, the strong magnetic anisotropy energy of these GNRs has not been successfully explained by any of the models yet, as ferromagnetic coupling alone does not result in a fixed magnetization direction.

Since the cobalt magnetization axis is aligned transverse to the ribbon, it is clear that the magnetization direction of the graphene is at least partially aligned along this direction, i.e. in the plane of the (0001) face and perpendicular to the transport direction. However, the exact alignment direction is not known, as these experiments were all performed with a consistent orientation of the cobalt contacts relative to the GNRs. Thus, the spin polarization measured in this work is simply a minimum value. It is possible that the spin polarization of the graphene is even higher than calculated with a magnetization direction that is not parallel to the cobalt magnetization axis. In future experiments, contacts with different magnetization directions could be used in order to probe the true magnetization direction of the graphene.

The measurements on sample 42OJ6 demonstrated the strong sensitivity of the GNR magnetization to temperature. At temperatures of 70K the magnetization direction of the GNRs was no longer fixed and at temperatures above 100K no magnetic switching was observed. In addition, the switch behavior changed as a result of the thermal cycling. Rather than returning to its initial 4K switch behavior after cooling, the magnitude and direction were changed. This change implies that the magnetization direction in the GNR is not an intrinsic property and may simply get "locked in" as the sample is cooled down. This observation may provide a means to control the magnetization direction in the GNRs. In future experimental work, it would be interesting to cool the samples in the

presence of an external magnetic field in order to test if the low temperature magnetization direction can be controlled.

All of the ribbons displayed TMR that was dependent on the DC bias across the tunnel junction. Furthermore, under the right conditions, the direction of the switch could be inverted by changing the junction bias. These results indicate that the spin polarization of the graphene might be gate controllable, which would be of great interest for the development of new spintronic devices. In future experiments, a separate gate could be added to decouple the effects of gating and tunnel current.

Another key measurement performed was the ribbon bias measurement on sample 42OJ6. This experiment showed that the spin switch was not affected by the direction of the current through the ribbon. This measurement rules out explanations that are based spin-orbit coupling, such as the Rashba effect, because if the spin polarization was momentum dependent, then reversing the current direction would reverse the spin switch. However, no such reversal was observed.

One key difference between the samples was the stability of the switch behavior. Measurements on sample 31JH6 were very consistent, while abrupt, unexplained reversals of the switch direction were observed in sample 42OJ6. This may be due to the difference in growth of the samples. 31JH6 was a single ribbon grown along the sidewall, while sample 42OJ7 was significantly overgrown with multiple ribbons between the contacts. Another possible cause is the difference in the tunnel barrier thickness from sample to sample. For instance, sample 31JH6 had a tunnel resistance of approximately 16MΩ while samples 42OJ6 and 42OJ7 had much lower tunnel resistance values of approximately 1.4MΩ and 500kΩ respectively.

There are many additional experiments that could also be performed to gain further insight into the nature of the spin polarization. To probe whether the spin polarization is a bulk property or the product of edge states, devices with contacts that only touch the ribbon edges could be fabricated. Devices can also be produced with multiple Co contacts next to each other with different coercive fields. This would allow for measurement of the spin potential, as done in the non-local measurements performed on planar graphene ribbons. Spin polarized scanning tunneling microscopy could also be employed to reveal magnetic information on the atomic scale.

Due to the complex nature of the observed phenomenon, the exact nature of the spin polarization is still unclear. The unique magnetic properties of these GNRs are likely related to the clean edge terminations or due to bonding between the GNR and substrate. The work of Palacio et al. [113] shows that the structure of the sidewall ribbons can be quite complicated, with "pinning" regions where the graphene appears to bond to the SiC substrate. This additional substrate bonding could break the A/B sublattice symmetry in places and lead to the ferromagnetic ordering observed here.

While much is still to be understood about these ribbons, this work gives an early glimpse of magnetic epitaxial graphene on SiC. These results have piqued the interest of experts in the field, and collaborative work with the Fert group in the coming year will seek further clarify the mechanism behind the observed graphene spin polarization. The integration of these magnetic GNRs with standard epitaxial graphene could prove to be a powerful platform for the development of future spintronic devices.

APPENDIX A

ANGLE DEPENDENT MAGNETORESISTANCE ANOMALY

As discussed in chapter 5.2, taking magnetoresistance measurements at different angles can be used to find the direction that maximizes the magnetoresistance response, which should correspond to the direction perpendicular to the plane of the nanoribbon. While nearly all of the angle dependent magnetoresistance data could be fit to a single component of the magnetic field, there were some segments that showed anomalous responses that could not be fit with this method. In order to maintain transparency, these anomalous results are presented here for your consideration.

After the transfer from Jiang's cryostat, the tunnel barriers below many of the Co contacts were destroyed, giving far lower contact resistances. Since the contact resistance was now low, some of these contacts were used in the magnetoresistance measurements. In particular, during the angular dependence measurements, a 4-point resistance measurement was made with current injected from G2 to G8 while the voltage was measured between C1 and G3. The results of this measurement could not be fit as a function of a single component of the magnetic field as was done with the other segments. When fit using the 11˚ facet angle that worked for other segments the peaks did not align, but using a facet angle of 37˚ did align the peak locations, but the peak heights were different. It should be noted that other 4-point measurements were made using a Co contact that did not show this strange behavior. This anomalous behavior was only observed on one other sample. A Co contact was used in a 4-point resistance measurement for that data as well. There were no measurements using all gold contacts that could not be fit using a single component of the magnetic field.

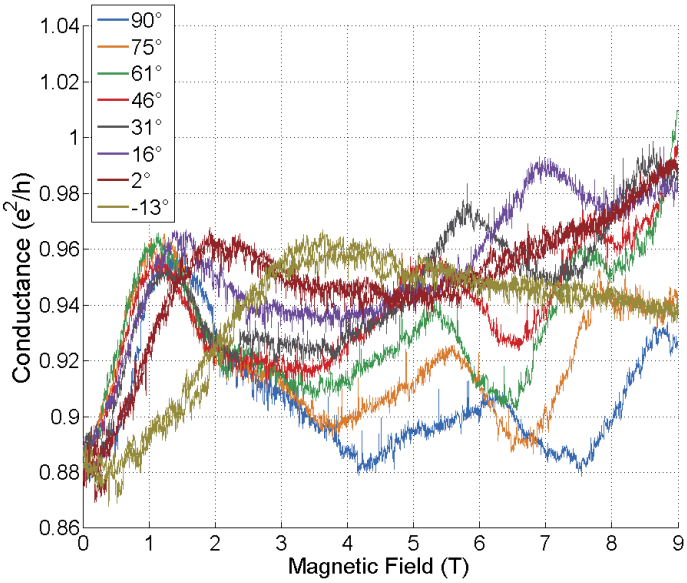

Figure A.1: The original 4pt conductance vs field data on 31JH6 ribbon TR contacts C1 to G3 measured at various angles.

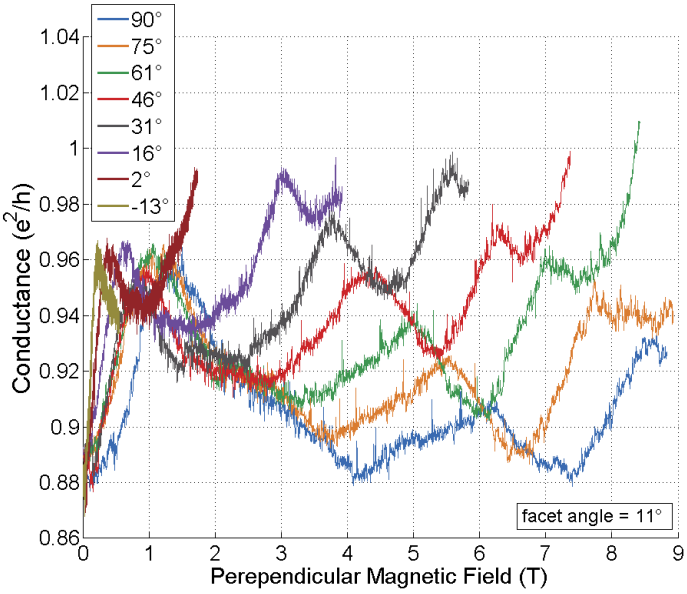

Figure A.2: Conductance vs perpendicular component of magnetic field fit using the 11˚ facet angle that fit for the other segments on this ribbon

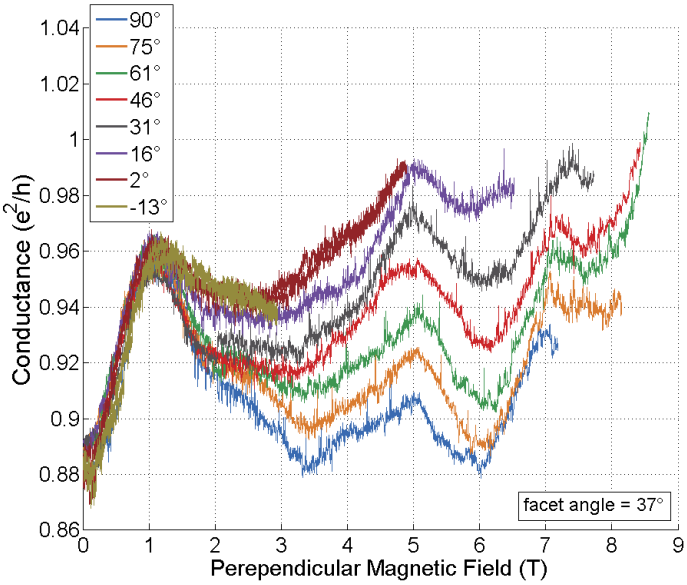

Figure A.3: Conductance vs perpendicular component of magnetic field fit using a 37˚, which aligns the peak locations.

REFERENCES

[1] D. Fathi, Journal of Nanotechnology **2011** (2011).

[2] P. R. Wallace, Physical Review **71**, 622 (1947).

[3] A. Castro Neto, F. Guinea, N. Peres, K. S. Novoselov, and A. K. Geim, Reviews of modern physics **81**, 109 (2009).

[4] K. S. Novoselov, A. K. Geim, S. V. Morozov, D. Jiang, M. I. Katsnelson, I. V. Grigorieva, S. V. Dubonos, and A. A. Firsov, Nature **438**, 197 (2005).

[5] M. Sprinkle, Georgia Institute of Technology, 2010.

[6] M. I. Katsnelson, K. S. Novoselov, and A. K. Geim, Nat Phys **2**, 620 (2006).

[7] P. L. McEuen, M. Bockrath, D. H. Cobden, Y.-G. Yoon, and S. G. Louie, Physical Review Letters **83**, 5098 (1999).

[8] J.-H. Chen, W. Cullen, C. Jang, M. Fuhrer, and E. Williams, Physical review letters **102**, 236805 (2009).

[9] D. K. Efetov and P. Kim, Physical Review Letters **105**, 256805 (2010).

[10] J. González, F. Guinea, and M. Vozmediano, Physical Review B **63**, 134421 (2001).

[11] V. N. Kotov, B. Uchoa, V. M. Pereira, F. Guinea, and A. H. Castro Neto, Reviews of Modern Physics **84**, 1067 (2012).

[12] X. Wu, Y. Hu, M. Ruan, N. K. Madiomanana, J. Hankinson, M. Sprinkle, C. Berger, and W. A. De Heer, Applied Physics Letters **95**, 223108 (2009).

[13] K. I. Bolotin, K. J. Sikes, Z. Jiang, M. Klima, G. Fudenberg, J. Hone, P. Kim, and H. L. Stormer, Solid State Communications **146**, 351 (2008).

[14] C. Berger *et al.*, The Journal of Physical Chemistry B **108**, 19912 (2004).

[15] Y. Zhang, Y.-W. Tan, H. L. Stormer, and P. Kim, Nature **438**, 201 (2005).

[16] K. S. Novoselov, A. K. Geim, S. V. Morozov, D. Jiang, Y. Zhang, S. V. Dubonos, I. V. Grigorieva, and A. A. Firsov, Science **306**, 666 (2004).

[17] Y. Zhang, J. P. Small, M. E. S. Amori, and P. Kim, Physical Review Letters **94**, 176803 (2005).

[18] A. J. Van Bommel, J. E. Crombeen, and A. Van Tooren, Surface Science **48**, 463 (1975).

[19] I. Forbeaux, J. M. Themlin, A. Charrier, F. Thibaudau, and J. M. Debever, Applied Surface Science **162–163**, 406 (2000).

[20] A. Y. Tontegode, Progress in Surface Science **38**, 201 (1991).

[21] G. Eda, G. Fanchini, and M. Chhowalla, Nature nanotechnology **3**, 270 (2008).

[22] H. Boehm, A. Clauss, G. Fischer, and U. Hofmann, Z Naturforsch **17**, 150 (1962).

[23] K. Novoselov, D. Jiang, F. Schedin, T. Booth, V. Khotkevich, S. Morozov, and A. Geim, Proceedings of the National Academy of Sciences of the United States of America **102**, 10451 (2005).

[24] Y. Ohashi, T. Koizumi, T. Yoshikawa, T. Hironaka, and K. Shiiki, 炭素 **1997**, 235 (1997).

[25] P. Blake, E. W. Hill, A. H. Castro Neto, K. S. Novoselov, D. Jiang, R. Yang, T. J. Booth, and A. K. Geim, Applied Physics Letters **91**, 063124 (2007).

[26] W. A. De Heer, C. Berger, M. Ruan, M. Sprinkle, X. Li, Y. Hu, B. Zhang, J. Hankinson, and E. Conrad, Proceedings of the National Academy of Sciences **108**, 16900 (2011).

[27] A. F. Young *et al.*, Nat Phys **8**, 550 (2012).

[28] R. Zan, Q. M. Ramasse, R. Jalil, and U. Bangert, *Atomic Structure of Graphene and h-BN Layers and Their Interactions with Metals* 2013), Advances in Graphene Science.

[29] X. Li *et al.*, Science **324**, 1312 (2009).

[30] K. S. Kim *et al.*, Nature **457**, 706 (2009).

[31] P. W. Sutter, J.-I. Flege, and E. A. Sutter, Nature materials **7**, 406 (2008).

[32] J. Coraux, T. N. Plasa, C. Busse, and T. Michely, New Journal of Physics **10**, 043033 (2008).

[33] S. Bae *et al.*, Nature nanotechnology **5**, 574 (2010).

[34] P. Y. Huang *et al.*, Nature **469**, 389 (2011).

[35] X. Li, C. W. Magnuson, A. Venugopal, R. M. Tromp, J. B. Hannon, E. M. Vogel, L. Colombo, and R. S. Ruoff, Journal of the American Chemical Society **133**, 2816 (2011).

[36] X. Li *et al.*, Nano Letters **10**, 4328 (2010).

[37] A. Ganguly, S. Sharma, P. Papakonstantinou, and J. Hamilton, The Journal of Physical Chemistry C **115**, 17009 (2011).

[38] G. Binnig, C. F. Quate, and C. Gerber, Physical review letters **56**, 930 (1986).

[39] *Park Systems XE-70 User's Manual*.

[40] *Veeco CP-II User's Manual*.

[41] R. Wiesendanger, *Scanning probe microscopy: Analytical methods* (Springer Science & Business Media, 1998).

[42] Ellipsometry Academy, www.horiba.com/scientific/products/ellipsometers/ellipsometry-academy/ (Accessed February 20th 2014).

[43] G. E. Jellison Jr, J. D. Hunn, and H. N. Lee, Physical Review B **76**, 085125 (2007).

[44] Ellipsometry - Surface and Interface Physics, http://physics.tcd.ie/Surfaces/ellipsometry2. (Accessed February 20th 2014).

[45] A. C. Ferrari and D. M. Basko, Nature nanotechnology **8**, 235 (2013).

[46] A. C. Ferrari *et al.*, Physical Review Letters **97**, 187401 (2006).

[47] I. Childres, L. A. Jauregui, W. Park, H. Cao, and Y. P. Chen, Developments in photon and materials research (2013).

[48] A. Ferrari and J. Robertson, Physical review B **61**, 14095 (2000).

[49] A. Das *et al.*, Nature nanotechnology **3**, 210 (2008).

[50] J. Kunc, Y. Hu, J. Palmer, C. Berger, and W. A. De Heer, Applied Physics Letters **103**, 201911 (2013).

[51] M. Altissimo, Biomicrofluidics **4**, 026503 (2010).

[52] T. Maassen, J. J. van den Berg, N. Ijbema, F. Fromm, T. Seyller, R. Yakimova, and B. J. van Wees, Nano Letters **12**, 1498 (2012).

[53] Y. S. Park, *SiC materials and devices* (Academic Press, London, 1998).

[54] G. L. Harris, *Properties of silicon carbide* (Iet, 1995), 13.

[55] P. N. First, W. A. de Heer, T. Seyller, C. Berger, J. A. Stroscio, and J.-S. Moon, MRS bulletin **35**, 296 (2010).

[56] V. Ramachandran, M. Brady, A. Smith, R. Feenstra, and D. Greve, Journal of Electronic Materials **27**, 308 (1998).

[57] J. Hass, W. De Heer, and E. Conrad, Journal of Physics: Condensed Matter **20**, 323202 (2008).

[58] V. Borovikov and A. Zangwill, Physical Review B **80**, 121406 (2009).

[59] F. Ming and A. Zangwill, Physical Review B **84**, 115459 (2011).

[60] Y. Hu, M. Ruan, Z. Guo, R. Dong, J. Palmer, J. Hankinson, C. Berger, and W. A. De Heer, Journal of Physics D: Applied Physics **45**, 154010 (2012).

[61] G. M. Rutter, N. P. Guisinger, J. N. Crain, E. A. A. Jarvis, M. D. Stiles, T. Li, P. N. First, and J. A. Stroscio, Physical Review B **76**, 235416 (2007).

[62] C. Riedl, C. Coletti, T. Iwasaki, A. A. Zakharov, and U. Starke, Physical Review Letters **103**, 246804 (2009).

[63] K. V. Emtsev *et al.*, Nature materials **8**, 203 (2009).

[64] M. Sprinkle, M. Ruan, Y. Hu, J. Hankinson, M. Rubio-Roy, B. Zhang, X. Wu, C. Berger, and W. A. De Heer, Nature Nanotechnology **5**, 727 (2010).

[65] M. Johnson, The Journal of Physical Chemistry B **109**, 14278 (2005).

[66] W. Thomson, Proceedings of the Royal Society of London **8**, 546 (1856).

[67] M. N. Baibich, J. M. Broto, A. Fert, F. N. Van Dau, F. Petroff, P. Etienne, G. Creuzet, A. Friederich, and J. Chazelas, Physical Review Letters **61**, 2472 (1988).

[68] G. Binasch, P. Grünberg, F. Saurenbach, and W. Zinn, Physical Review B **39**, 4828 (1989).

[69] C. Kittel, Reviews of modern Physics **21**, 541 (1949).

[70] C. Kittel, *Introduction to solid state physics.* (John Wiley and Sons, Inc, 2005), ISBN 047141526X.

[71] M. Johnson, Proceedings of the IEEE **91**, 652 (2003).

[72] E. Y. Tsymbal and D. Pettifor, Solid state physics **56**, 113 (2001).

[73] S. M. Thompson, Journal of Physics D: Applied Physics **41**, 093001 (2008).

[74] N. Mott and H. Wills, in *Proc. R. Soc. Lond. A*1936), pp. 368.

[75] C. Chappert, A. Fert, and F. N. Van Dau, Nat Mater **6**, 813 (2007).

[76] J. Bardeen, Physical Review Letters **6**, 57 (1961).

[77] M. Julliere, Physics Letters A **54**, 225 (1975).

[78] J. M. De Teresa, A. Barthelemy, A. Fert, J. P. Contour, F. Montaigne, and P. Seneor, Science **286**, 507 (1999).

[79] M. Sharma, S. X. Wang, and J. H. Nickel, Physical Review Letters **82**, 616 (1999).

[80] J. S. Moodera, L. R. Kinder, T. M. Wong, and R. Meservey, Physical Review Letters **74**, 3273 (1995).

[81] T. Miyazaki and N. Tezuka, Journal of Magnetism and Magnetic Materials **139**, L231 (1995).

[82] M. Johnson, Semiconductor science and technology **17**, 298 (2002).

[83] P. Seneor, B. Dlubak, M. Martin, A. Anane, H. Jaffres, and A. Fert, MRS Bull **37**, 1245 (2012).

[84] E. W. Hill, A. K. Geim, K. Novoselov, F. Schedin, and P. Blake, Magnetics, IEEE Transactions on **42**, 2694 (2006).

[85] W. Han, K. Pi, K. M. McCreary, Y. Li, J. J. I. Wong, A. G. Swartz, and R. K. Kawakami, Physical Review Letters **105**, 167202 (2010).

[86] N. Tombros, C. Jozsa, M. Popinciuc, H. T. Jonkman, and B. J. van Wees, Nature **448**, 571 (2007).

[87] H. Goto, A. Kanda, T. Sato, S. Tanaka, Y. Ootuka, S. Odaka, H. Miyazaki, K. Tsukagoshi, and Y. Aoyagi, Applied Physics Letters **92**, 212110 (2008).

[88] O. Megumi, S. Masashi, N. Ryo, N. Takayuki, S. Teruya, and S. Yoshishige, Japanese Journal of Applied Physics **46**, L605 (2007).

[89] P. J. Zomer, M. H. D. Guimarães, N. Tombros, and B. J. van Wees, Physical Review B **86**, 161416 (2012).

[90] M. H. D. Guimarães, A. Veligura, P. J. Zomer, T. Maassen, I. J. Vera-Marun, N. Tombros, and B. J. van Wees, Nano Letters **12**, 3512 (2012).

[91] B. Dlubak *et al.*, Nat Phys **8**, 557 (2012).

[92] W. Han, K. M. McCreary, K. Pi, W. H. Wang, Y. Li, H. Wen, J. R. Chen, and R. K. Kawakami, Journal of Magnetism and Magnetic Materials **324**, 369 (2012).

[93] W. L. Wang, O. V. Yazyev, S. Meng, and E. Kaxiras, Physical Review Letters **102**, 157201 (2009).

[94] W. L. Wang, S. Meng, and E. Kaxiras, Nano Letters **8**, 241 (2008).

[95] Y.-W. Son, M. L. Cohen, and S. G. Louie, Nature **444**, 347 (2006).

[96] L. Pisani, J. A. Chan, B. Montanari, and N. M. Harrison, Physical Review B **75**, 064418 (2007).

[97] L. Yang, M. L. Cohen, and S. G. Louie, Physical Review Letters **101**, 186401 (2008).

[98] O. V. Yazyev and L. Helm, Physical Review B **75**, 125408 (2007).

[99] J. Hong *et al.*, Small **7**, 1175 (2011).

[100] S. Niyogi, E. Bekyarova, J. Hong, S. Khizroev, C. Berger, W. de Heer, and R. C. Haddon, The Journal of Physical Chemistry Letters **2**, 2487 (2011).

[101] M. Wimmer, İ. Adagideli, S. Berber, D. Tománek, and K. Richter, Physical Review Letters **100**, 177207 (2008).

[102] O. V. Yazyev, Reports on Progress in Physics **73**, 056501 (2010).

[103] A. D. Hernández-Nieves, B. Partoens, and F. M. Peeters, Physical Review B **82**, 165412 (2010).

[104] L. F. Huang, X. H. Zheng, G. R. Zhang, L. L. Li, and Z. Zeng, The Journal of Physical Chemistry C **115**, 21088 (2011).

[105] J.-H. Lee and J. C. Grossman, Applied Physics Letters **97**, 133102 (2010).

[106] M. J. Schmidt and D. Loss, Physical Review B **82**, 085422 (2010).

[107] A. Ramasubramaniam, N. V. Medhekar, and V. B. Shenoy, Nanotechnology **20**, 275705 (2009).

[108] M. Y. Han, J. C. Brant, and P. Kim, Physical Review Letters **104**, 056801 (2010).

[109] D. Gunlycke, H. M. Lawler, and C. T. White, Physical Review B **75**, 085418 (2007).

[110] J. Baringhaus *et al.*, Nature **506**, 349 (2014).

[111] M. B. Lundeberg and J. A. Folk, Physical Review Letters **105**, 146804 (2010).

[112] R. Meservey and P. M. Tedrow, Physics Reports **238**, 173 (1994).

[113] I. Palacio *et al.*, Nano Letters **15**, 182 (2015).

VITA

JOHN H. HANKINSON

Hankinson was born in Tallahassee, Fl in 1985. He attended public schools in Palatka, Fl and Decatur, Ga. He received a B.S. in Physics from Harvey Mudd College in 2007 before coming to Georgia Tech to pursue a doctorate in condensed matter physics. When he is not working on his research, Mr. Hankinson enjoys spending time with his beagle, Buddy.